
Towards Ultracold Polar NaK Molecules and the Investigation of Dipolar Quantum Gases

VON DER FAKULTÄT FÜR MATHEMATIK UND PHYSIK DER
GOTTFRIED WILHELM LEIBNIZ UNIVERSITÄT HANNOVER

zur Erlangung des Grades

DOKTOR DER NATURWISSENSCHAFTEN

– DR. RER. NAT. –

genehmigte Dissertation

von

Matthias Walter GEMPEL

Geboren am 08.06.1985,
in Treuchtlingen

2016

Referent:

Prof. Dr. S. OSPELKAUS
Institut für Quantenoptik,
Leibniz Universität Hannover

Koreferent:

Priv.-Doz. Dr. C. KLEMP
Institut für Quantenoptik,
Leibniz Universität Hannover

Tag der Promotion:

05. Februar 2016

¡ Vaya Máquina !

Abstract

Ultracold atomic gases have proven to be excellent test grounds for implementing a large variety of quantum-many-body systems. Equipping them with the long-range and anisotropic interactions of polar molecules will pave the way for studying fascinating physics.

This work presents the design and setup of an experiment devised for the creation of ultracold $^{23}\text{Na}^{40}\text{K}$ ground state molecules, tailored to investigate dipolar interactions. The molecule creation will start from the preparation of a two-component quantum degenerate mixture of ^{23}Na and ^{40}K . Both atomic species will be associated to loosely bound Feshbach molecules and subsequently transferred to the rovibrational ground state via a two-photon transition. Within this thesis, two cold atomic beams of ^{23}Na and ^{40}K , a two-species magneto-optical trap and magnetic trapping of both species have been implemented.

The dipolar interaction of ground state polar molecules can be induced when polarizing the molecules by means of electric DC fields. Within this thesis, I present an electrode geometry which allows for electric field magnitudes up to 10 kV/cm with relative deviations below 10^{-6} , in the volume of the dipole trap. The direction of the field is fully rotatable in a two-dimensional, vertical plane. Accordingly, it will be possible to polarize NaK ground state molecules up to 68% of their internal dipole moment (2.76 D), along any direction in this plane. The electrode geometry also enables electric field gradients of 3 kV/cm². This allows to address the rotational states of molecules confined in a vertical optical lattice layerwise. Such versatile electric fields are indispensable, when investigating the proposed phase diagrams of dipolar quantum gases.

Some of the phases appearing in optical lattices can be recognized by their in-situ density distributions. To enable single-site sensitive imaging of molecules in an optical lattice, a microscope objective was devised. The objective is a two lens design, aiming for a resolution corresponding to an Airy radius of 0.69 μm , at the sodium D2 line, i.e., 589 nm. The performance of the objective was tested by measuring the point spread function, by means of imaging gold nanoparticles. The images of those nanoparticles suggest an Airy radius of $0.71^{+0.02}_{-0.03}$ μm and diffraction limited performance.

The combination of all components shown in this work will open the way to investigate strong dipolar interactions in the quantum regime.

Ultracold molecules, electric fields, imaging.

Zusammenfassung

Ultrakalte Gase haben sich als ideal für die Implementierung von Quantenvielteilchensystemen erwiesen. Erweitert man sie um die langreichweitige, anisotrope Wechselwirkung polarer Moleküle, öffnen sich Wege zur direkten Beobachtung faszinierender Physik, wie Modellen die mit Hochtemperatursupraleitung assoziiert werden. Diese Arbeit beschreibt ein Experiment, gebaut um ultrakalte $^{23}\text{Na}^{40}\text{K}$ Grundzustandsmoleküle in optischen Gittern zu erzeugen und deren Wechselwirkung zu untersuchen.

Das Experiment beinhaltet alle Komponenten um eine Mischung von ultrakalten ^{23}Na und ^{40}K Gasen zu erzeugen. Aus dieser werden dann durch eine Feshbach Resonanz heteronukleare $^{23}\text{Na}^{40}\text{K}$ Moleküle assoziiert, welche über einen Zweiphotonenprozess in ihren absoluten Grundzustand transferiert werden. Während dieser Arbeit wurden kalte ^{23}Na und ^{40}K Atomstrahlen, die jeweiligen magneto-optischen Fallen und das Laden beider Spezies in eine Magnetfalle implementiert.

Die Grundzustandsmoleküle können mithilfe von elektrischen Feldern polarisiert werden. Eine im Rahmen dieser Arbeit entwickelte Elektrodengeometrie erlaubt es am Ort der Moleküle elektrische Felder von bis zu 10 kV/cm, mit relativen Abweichungen unter 10^{-6} zu erzeugen. Die Richtung der Felder kann in einer vertikalen Ebene, aufgespannt von zwei Achsen des optischen Gitters, frei rotiert werden. Dies erlaubt eine freie Einstellbarkeit der Dipolwechselwirkung zwischen den Molekülen – von schwacher zu starker und von repulsiver zu attraktiver Wechselwirkung. Um die Rotationszustände von Molekülen in einzelnen Lagen eines eindimensionalen optischen Gitters zu adressieren, können vertikale, elektrische Feldgradienten bis 3 kV/cm^2 angelegt werden. Diese hohe Flexibilität der elektrischen Felder ist unabdingbar um die Phasendiagramme von dipolaren Quantengasen zu untersuchen.

Einige dieser Phasen können aufgrund ihrer mikroskopischen Dichteverteilung in optischen Gittern charakterisiert werden. Hierzu wurde ein einfaches, hochauflösendes Objektiv aus zwei Linsen entwickelt. Das Objektiv hat einen Arbeitsabstand von 22 mm und kann an verschiedene Experimentvoraussetzungen angepasst werden. Die Vermessung der Punktspreizfunktion des Objektivs mit Goldnanopartikeln, bei einer Wellenlänge von 589 nm, ergab beugungsbegrenzte Auflösung bei einem Airy Radius von $0.71^{+0.02}_{-0.03}\text{ }\mu\text{m}$. Dieser Wert erlaubt es einzelne Natrium Atome auf den Plätzen eines optischen Gitters mit 532 nm Gitterkonstante aufzulösen zu können.

Das im Rahmen dieser Arbeit entwickelte Experiment umfasst alle Komponenten, die nötig sind, um polar ultrakalte Moleküle in optischen Gittern zu erzeugen. Die entwickelte Elektrodenkonfiguration erlaubt die Manipulation und Kontrolle des elektrischen Dipolmomentes der Moleküle, sowie deren selektive Adressierung in einzelnen Lagen eines eindimensionalen optischen Gitters. Zusammen mit den entwickelten hochauflösenden Abbildungsmethoden wird dieses Experiment die Möglichkeit eröffnen, starke Dipolwechselwirkungen in Quantenvielteilchensystemen zu untersuchen.

Ultrakalte Moleküle, elektrische Felder, Abbildung.

Contents

| | | |
|----------|-------------------------------------------------------------------|-----------|
| 1 | Polar Molecules | 1 |
| 2 | Experiment Setup | 9 |
| 2.1 | Overview | 10 |
| 2.1.1 | Towards Ultracold NaK Molecules | 10 |
| 2.1.2 | Internal States - Energetic Structure of Ground State | 11 |
| 2.2 | Laboratory Requirements | 13 |
| 2.3 | Main Chamber | 14 |
| 2.4 | D2 Line Laser Systems | 17 |
| 2.4.1 | Potassium Laser System | 17 |
| 2.4.2 | Sodium Laser System | 20 |
| 2.5 | Magnetic Fields | 22 |
| 2.5.1 | Coil Design | 22 |
| 2.5.2 | Compensation Cage | 25 |
| 2.6 | Laser Cooling | 26 |
| 2.6.1 | Cases of ^{23}Na and ^{40}K | 26 |
| 2.6.2 | Zeeman Slower | 27 |
| 2.6.3 | 2D-MOT | 29 |
| 2.6.4 | 3D-MOT | 31 |
| 2.7 | Magnetic Trap | 32 |
| 2.7.1 | Magnetic Trapping of ^{40}K | 33 |
| 2.7.2 | Magnetic Trapping of ^{23}Na | 35 |
| 2.8 | Evaporation and Microwaves | 35 |
| 2.8.1 | Evaporation in Current Situation | 37 |
| 2.8.2 | Microwave Setup | 38 |
| 2.9 | Dipole Trap | 40 |
| 2.9.1 | Implementation | 41 |
| 2.9.2 | Optical Lattice | 42 |
| 2.10 | Imaging | 42 |
| 2.10.1 | Different Techniques | 43 |
| 2.10.2 | PolarCam | 44 |
| 2.11 | Towards the Creation of Molecules | 47 |
| 2.11.1 | Feshbach Molecules | 48 |
| 2.11.2 | Ground State Transfer | 49 |
| 3 | Electric Fields | 53 |
| 3.1 | Molecules in Electric Fields | 55 |
| 3.2 | The Effect of Electric Fields on Trapped Molecules | 57 |
| 3.2.1 | Different Contributions of the Electric Field | 58 |
| 3.2.2 | Addressing Single Layers Using Electric Field Gradients | 61 |
| 3.3 | Electrode Configuration | 63 |
| 3.3.1 | Plate Capacitors | 64 |
| 3.3.2 | Four Rods | 64 |
| 3.3.3 | Configuration of Eight Rods | 66 |
| 3.3.4 | Main Windows | 69 |
| 3.4 | Conclusion | 71 |

| | |
|-------------------------------------------------------|------------|
| 4 High Resolution Imaging | 73 |
| 4.1 Imaging of Molecules | 74 |
| 4.2 Imaging | 75 |
| 4.2.1 General Terms | 76 |
| 4.2.2 Quality Criteria | 77 |
| 4.2.3 Aberrations | 78 |
| 4.3 Ideal System | 80 |
| 4.3.1 Optimization Definitions | 80 |
| 4.3.2 Optimization Results | 82 |
| 4.4 System Tolerances | 84 |
| 4.4.1 Tolerances of the Objective | 84 |
| 4.4.2 Effect of Compensators | 86 |
| 4.4.3 Air versus Vacuum | 87 |
| 4.4.4 Other Wavelength | 88 |
| 4.4.5 Window Properties | 89 |
| 4.5 Mounting | 91 |
| 4.6 Characterization | 92 |
| 4.6.1 1951 USAF Resolution Test Chart | 92 |
| 4.6.2 Point Spread Function - Pinhole | 93 |
| 4.6.3 Point Spread Function - Nanoparticles | 94 |
| 4.7 Conclusion | 98 |
| 5 Outlook | 99 |
| 5.1 Setup | 100 |
| 5.2 Electric Fields | 100 |
| 5.3 Objective | 102 |
| A Appendix | 103 |
| A.1 Constants | 104 |
| A.2 Laboratory Conditions | 105 |
| A.3 Offset Lock | 106 |
| A.4 Coil Control | 108 |
| A.5 Electrodes | 109 |
| A.6 Objective | 111 |
| A.6.1 Non Ideal Imaging | 111 |
| A.6.2 Zemax | 112 |

CHAPTER 1

Polar Molecules

Cold atom experiments have redefined the frontier in the experimental exploration of quantum mechanics. Since the first direct demonstrations of Bose-Einstein condensation [1, 2] and the creation of a degenerate Fermi gas [3] strong efforts arose to explore physics originally solely affiliated with condensed matter. These efforts did manifest in achievements like probing the BCS-BEC crossover [4] or the superfluid to Mott insulator transition [5], the latter becoming possible by the implementation of periodic potentials, using so called optical lattices [6, 7].

Therefore – might ultracold atomic quantum gases appear too artificial in their own right – they are certainly capable of modeling a huge variety of quantum systems [8]. Due to their cleanness, the excellent adjustability of nearly any parameter and the possibility to observe effects directly, ultracold atomic gases are the ideal testing ground for quantum-many-body phenomena [9, 10].

All the fascinating physics named above was studied in systems of alkali atoms. These have the advantage of a relatively simple level structure, and hence can well be cooled to ultra low temperatures. The interactions between alkali atoms, however, are to a good approximation isotropic and short-ranged which limits the modeling capabilities to systems with contact interactions. Systems with long-range interactions, exhibiting effects like ergodicity breaking [11] or negative specific heat [12], go beyond this. As in experiments with alkali atoms interactions between neighboring sites of optical lattices can only be mediated by second order processes [13], huge efforts were dedicated to overcome this limitation. Dipolar particles, namely atomic species with large magnetic moments and polar molecules are the prime candidates in this race. Their pairwise interaction

$$V_{dd} \sim \frac{d^2}{r^3} \cdot [1 - 3 \cos^2 \theta] \quad (1.1)$$

arising from the dipole moments d is not only long-range in the separation of the particles r but also anisotropic, indicated by the dependence on the angle θ , enclosed by the mutual orientation of the dipole moments and the interparticle axis.

Two quantities characterizing the dipolar interaction are its magnitude

$$V_{dd,0} = K \frac{d^2}{r^3}, \quad (1.2)$$

and the corresponding dipole length [14]

$$a_{dd} = K \frac{m d^2}{\hbar^2}. \quad (1.3)$$

The prefactor K has to be replaced by $\frac{\mu_0}{4\pi}$ in the case of magnetic dipoles and by $\frac{1}{4\pi\epsilon_0}$ for electric ones. As usual, ϵ_0 and μ_0 denote the vacuum permittivity and the vacuum permeability, m is the reduced mass. Using the two quantities, $V_{dd,0}$ and a_{dd} , the strength of different magnetic and electric dipoles can be compared in the same plot, like the one in Fig. 1.1.

Despite being on the very left side of this plot, effects of dipolar interactions can already be observed in experiments with ^{87}Rb [15], which has a dipole moment of only one

Bohr magneton μ_B . Atoms like chromium [16], erbium [17] and dysprosium [18] with dipole moments of $6\mu_B$, $7\mu_B$ and $10\mu_B$, respectively, show significantly stronger dipolar interactions than rubidium due to the quadratic dependence of the interaction on d .

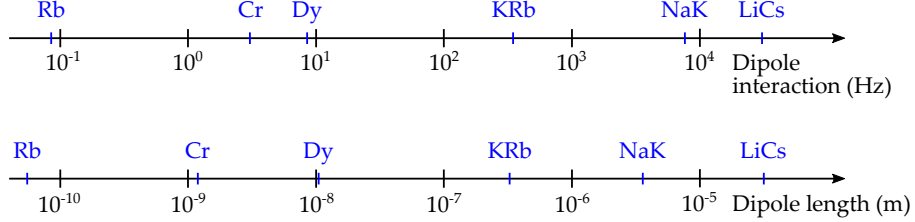


Figure 1.1: Comparison of dipolar interactions for different magnetic atoms and polar molecules. The upper graph shows $V_{dd,0}$ for selected atoms and ground state alkali dimers at a separation of $r = 532$ nm. This separation corresponds to the a lattice constant typically present in ultracold atom experiments. The lower graph shows the dipole length a_{dd} of the same particles. Rydberg atoms can have dipole moments which are several order of magnitude larger than those of atoms or ground state molecules and are off the chart, here. The molecular values are taken from [19].

Therefore, first evidence of strong dipolar interactions at ultracold temperatures was found in such systems. The anisotropic expansion [20] and the d -wave collapse [21] of a chromium Bose-Einstein condensate could be observed after reducing the contact interaction by means of a Feshbach resonance. Via the same tuning knob, the stability of the condensate in a one-dimensional optical lattice [22] was investigated. In a condensate of dysprosium, which has a significantly higher dipole moment than chromium, the anisotropic expansion of a BEC could already be observed ‘without careful minimization’ [18] of the contact interaction. With a degenerate gas of fermionic erbium the effects of dipolar interactions on the momentum distribution [23] and the relaxation dynamics of anisotropically excited systems [24] were probed.

Still, the magnetic dipolar interaction between atoms cannot come close to the values that are possible considering the electric dipole moments of ground state polar molecules. Figure 1.1 emphasizes that the difference in the interaction potential is about two to three orders of magnitude. At a distance of $r = 532$ nm, which is a typical lattice constant in ultracold atomic gas experiments, the interaction potential between two NaK molecules can correspond to about 400 nK, an actually feasible temperature for current experiments. This energy scale strongly indicates that polar molecule are excellent candidates to observe dipolar effects in ultracold quantum gases. First experiments with ultracold gases of KRb molecules [25] have used the strong dipolar interaction in combination with carefully designed external confinement to suppress inelastic two body collisions [26]. Nearest neighbor interactions could be probed when those molecules were confined at the sites of a three-dimensional optical lattice, by observing oscillations in the contrast of Ramsey fringes [27].

Nonetheless, a large amount of dipolar quantum phenomena could not yet be implemented and the theoretically proposed effects outnumber the already observed by far. Among those [28, 29, 30, 31] are the detailed study of the ground state of dipolar bosons in a two-dimensional optical lattices [32], the roton spectrum [33], super-

fluid pairing [34], dipolar chains forming quantum liquids [35], interlayer superfluidity [36], non-local state swapping [37], supersolid phases [38, 39, 40], quantum magnetism [41, 42], spin-orbit coupling [43], topological phases [44], and the dynamics of long-range interactions [45, 46].

The exploration of supersolid phases, for example, experienced a truly diverse past. Supersolids were predicted in 1969 [47, 48] and suggested to be identified by anomalous rotation [49]. A first indication for their existence, namely by detecting anomalous rotation of ^4He at 200 mK, was only reported in 2004 [50]. Since then, the underlying mechanisms of the observed system and of the supersolid phenomenon in general have been up for discussion [51, 52, 53]. The effects of impurities and lattice defects, for instance, still remain not clearly identified [51]. Only recently, the existence of a supersolid phase in ensembles of strongly interacting, bosonic [38, 39] or fermionic [40] polar molecules was proposed. In the model, the molecules are confined in a quasi two-dimensional geometry with an optical lattice structure, imprinted along the transverse directions. As optical lattices are well defined and do not suffer from defects, such systems could potentially rule out dislocations as a necessary ingredient for reaching supersolidity. The molecules are supposed to be polarized perpendicularly to the confining two-dimensional layer, hence their long-range interaction is isotropic and repulsive. It was found that strong interactions stabilize and increase the supersolid regime [38, 40], which makes polar molecules the ideal candidates. The supersolid phase is then obtained by doping respective Mott solids with particles or vacancies [38, 40]. For fermionic molecules, the supersolid originates from a checkerboard phase at filling factor one, leading to singlet pairing of molecules with different spin [40]. Doping the system with particles, however, appears to be challenging, especially for the KRb molecules considered in the proposal [40]. As KRb systems suffer from inelastic two-body collisions [26], chemically stable molecules, like those indicated in Fig. 1.2, will provide a better choice. Nevertheless, doping the system with vacancies, also leads to the formation of a supersolid, which can, in the case of strong interactions, already emerge at filling factors substantially below one. Finally, the supersolid phase can be identified by its in situ density distribution, in combination with the singlet pairing order parameter, which requires high resolution imaging [40].

In addition to quantum-many-body physics, cold polar molecules are an excellent test ground to search for an electric dipole moment of the electron [54], implementing quantum computation schemes [55], or investigating ultracold chemistry [26].

Based on this high demand in various fields, many and vastly different strategies are pursued to obtain cold and ultracold gases of molecules. All those strategies can be accounted to two fundamentally different ideas. Some approaches try to cool samples of molecules directly, whereas the other concept is to cool two species of atoms and combine them to diatomic molecules.

The direct cooling methods include techniques like: supersonic expansion, buffer gas cooling [56, 57], Stark deceleration [58], centrifuge deceleration [59], Sisyphus cooling [60], laser cooling [61], and evaporative cooling [62]. Despite the large number of techniques those direct cooling methods are far from reaching quantum degeneracy and at the current stage not ideal to prepare samples for studying quantum-many-body physics.

The other concept, referred to as indirect cooling, includes two major techniques which are currently pursued. One of them, photo association [63, 64, 65], has not shown the possibility to reach quantum degeneracy, yet. In contrast, the association of ultracold atoms to diatomic ground state molecules via Feshbach resonances and stimulated Raman adiabatic passage (STIRAP) has demonstrated the possibility to prepare molecules at a phase space density of 0.1 [25]. This is only one order of magnitude from quantum degeneracy. The major advantage of this approach over direct cooling techniques is that many atoms can already be cooled to quantum degeneracy. In contrast to photo association, the coherent transfer to the molecular ground state is more efficient, transfers molecules to a single, selected quantum state and introduces only a negligible amount of heat to the sample.

Among the huge number of possible polar molecules dialkalis represent a small and maybe untypical group of candidates. However, until today alkali atoms are the species routinely cooled to quantum degeneracy: very fast, efficient and in large samples. Accordingly, it is worth looking for suitable polar molecules amongst the heteronuclear alkali dimers. Figure 1.2 lists all those candidates in rising order of their permanent dipole moment d' , with all values normalized to the corresponding value of NaK.

The ratio of the molecular dipole moment and the rotational constant B

$$\mathcal{E}_c := \frac{B}{d'}, \quad (1.4)$$

called the characteristic electric field, is the natural scale for the electric field required to polarize a molecule. A large \mathcal{E}_c reveals that high electric fields are required to reach a certain polarization. The dipolar interaction is shown in form of the dipole length $a'_{dd'}$, considering fully polarized molecules.

Comparing them to Fig. 1.1, many of the candidates listed in Fig. 1.2 are promising in terms of their physical properties. However, electronic structure calculations [66] have shown that half of the heteronuclear alkali dimers undergo exothermic chemical reactions in two body collisions, which reduces the lifetime of the molecular sample. In fact, those reactions could be suppressed by confining the molecules in optical lattices or applying external electric fields [26, 67]. Nevertheless, this necessity limits the physics that can be investigated with chemically reactive species.

Figure 1.2 indicates the chemically unstable molecules by red markers. Additionally, it indicates the possible quantum statistical character of each molecule, accounting for different atomic isotopes. Considering that strongly interacting, dipolar bosons are more extensively investigated theoretically than fermions [31], the latter can subjectively be more interesting to investigate, also because fermionic properties are fundamental to all electronic phenomena. Further, it was shown that dipolar fermions, confined in a quasi two-dimensional geometry, can be stabilized against inelastic collisions [26], which can make them experimentally more convenient.

When aiming to investigate chemically stable, fermionic molecules, which are essential for probing the fermionic supersolid phase, it is evident that the choice is limited to KCs and NaK. Both have very similar properties. Whereas the former is easier to polarize, the latter has the advantage of a larger internal dipole moment. Regarding the actual implementation, a significant amount of spectroscopic data is available for NaK. Also it

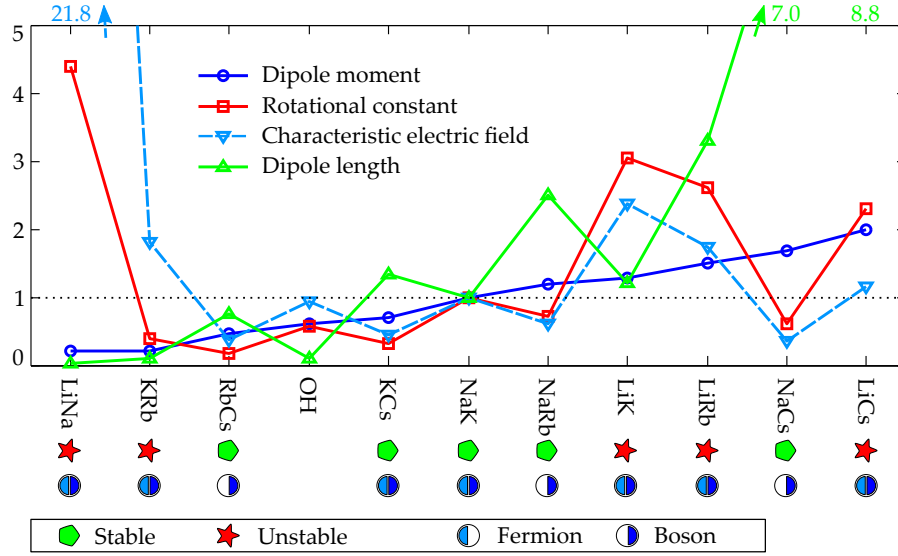


Figure 1.2: Dipole moments, rotational constants, characteristic electric field and dipole length for alkali dimers normalized to the corresponding values of NaK OH is included for comparison. For NaK we used: $d' = 2.762$ Debye, $B = 2.93 \text{ GHz} \times h$, $\mathcal{E}_{\text{char}} = 2.11 \text{ kV/cm}$ and $a'_{\text{dd}} = 3.59 \mu\text{m}$. The numbers indicate the respective values which are not depicted anymore. The lines serve as a guide to the eye. The symbols below indicate the chemical stability of the molecules in two body collisions, following [66] and their quantum statistical character.

Values for the dipole moment and equilibrium nuclear spacings are taken from [19]. The rotational constant $B = \frac{\hbar}{2mR_{\text{ave}}^2} \frac{h}{2\pi}$ of the molecules was computed using the reduced mass m and the average separation of the nuclei R_{ave} . For OH the dipole moment is $1.66758(10)$ Debye [68], the Λ -doubling is 1.667 GHz [69], and the characteristic field does not consider the angular momentum which would require a correction [70].

was shown that huge condensates of Na can be created with a high repetition rate [71, 72], whereas Cs can be difficult to condense due to inelastic collisions[73, 74].

For these reasons, this experiment works towards the creation of ultracold, fermionic, polar $^{23}\text{Na}^{40}\text{K}$ ground state molecules to test the fascinating physics which was theoretically proposed. Considering $^{23}\text{Na}^{39}\text{K}$, the possibility to work in the direction of a dipolar gas of bosons is provided, too.

In the following three chapters I will present the design of an experiment dedicated to create $^{23}\text{Na}^{40}\text{K}$ ground state molecules, and at the same time tailored to investigate the dipolar interactions between those molecules. Such an experiment can for example be used to investigate a proposed supersolid phase in two-dimensional, fermionic systems.

After a quick overview of the experimental sequence and the relevant properties of dialkali ground state molecules at the beginning of Chapter 2, I will first address topics which most ultracold gases experiments have in common: laboratory conditions, the main vacuum chamber, the laser systems for cooling the relevant atomic species, and the coils for creating the necessary magnetic fields. Referencing to those sections, the remainder of the chapter will shortly outline the most relevant steps towards the creation of ultracold $^{23}\text{Na}^{40}\text{K}$ molecules, considering the technical requirements and appropriate solutions.

Chapter 3 will address the topic of polarizing ground state polar molecules by means of electric DC fields. This includes the discussion of an electrode geometry which is actually suitable to create extremely uniform electric fields, while being adaptive enough to freely rotate the dipoles' orientation in a plane spanned by two axes of the optical lattice. Being able to rotate the electric field and change its magnitude, the full character of the dipolar interaction becomes accessible – from repulsive to attractive – from weak to strong. Within the volume of the dipole trap the residual relative irregularities of the electric field magnitude can be below 10^{-6} . In these electric fields even fully polarized molecules could be confined in a potential only $1 \mu\text{K} \times k_B$ deep, when providing support against gravity. The design of the electrode geometry also allows for strong electric field gradients enabling to address rotational states in an one-dimensional optical lattice layerwise. The splitting of rotational transitions between different layers, spaced by 532 nm, can be as high as 100 kHz.

In Chapter 4, I will introduce a very simple two lens objective, that is applicable for imaging sodium atoms with single-site resolution in an optical lattice with a lattice spacing of 532 nm. Such a high resolution is, for instance, required to identify the checkerboard pattern of the in-situ density distribution in a two-dimensional supersolid. I will present the high resolution objective, its sensitivity to manufacturing tolerances and the adaptivity to various external parameters is simulated. The results indicate that the objective is highly variable regarding the imaging wavelength and the properties of the vacuum window, implying that the objective can be of use for other experiments, too. During the performance evaluation of a test setup, at an imaging wavelength of 589 nm, the Airy radius of the objective was estimated to be $0.71^{+0.02}_{-0.03} \mu\text{m}$. In the modulation transfer function this Airy radius correspond to a spatial cutoff frequency of 1720 lp/mm. The volume under the point spread function's fast Fourier transform suggests diffraction limited performance, when compared to the corresponding volume under the fast Fourier transform of an Airy disk with 0.69 μm radius.

In summary the experiment will contain all necessary components to create and identify quantum phases, like a supersolid, in a system of fermionic, polar $^{23}\text{Na}^{40}\text{K}$ molecules: the possibility to create ultracold ground state molecules, the electric fields to polarize them and high resolution imaging to finally identify the phase.

CHAPTER 2

Experiment Setup

In this chapter I will present an experiment for creating, manipulating, and investigating ultracold polar molecules in optical lattices. The experimental setup comprises a two species quantum gas apparatus and additional components for the controlled association of ultracold molecules. Before introducing the experiment setup, the following section shortly outlines the strategy towards the creation of an ultracold gas of NaK molecules and describes their electronic ground state potential.

2.1 Overview

2.1.1 Towards Ultracold NaK Molecules

As mentioned in Chapter 1, the reported direct cooling methods for molecules seem to be far from reaching quantum degeneracy. Though, creating a quantum degenerate gas of heteronuclear ground state molecules from ultracold atomic samples appears to be within reach [25]. The strategy of the experiment described here is to assemble $^{23}\text{Na}^{40}\text{K}$ ground state molecules from an ultracold cloud of atomic ^{23}Na and ^{40}K .

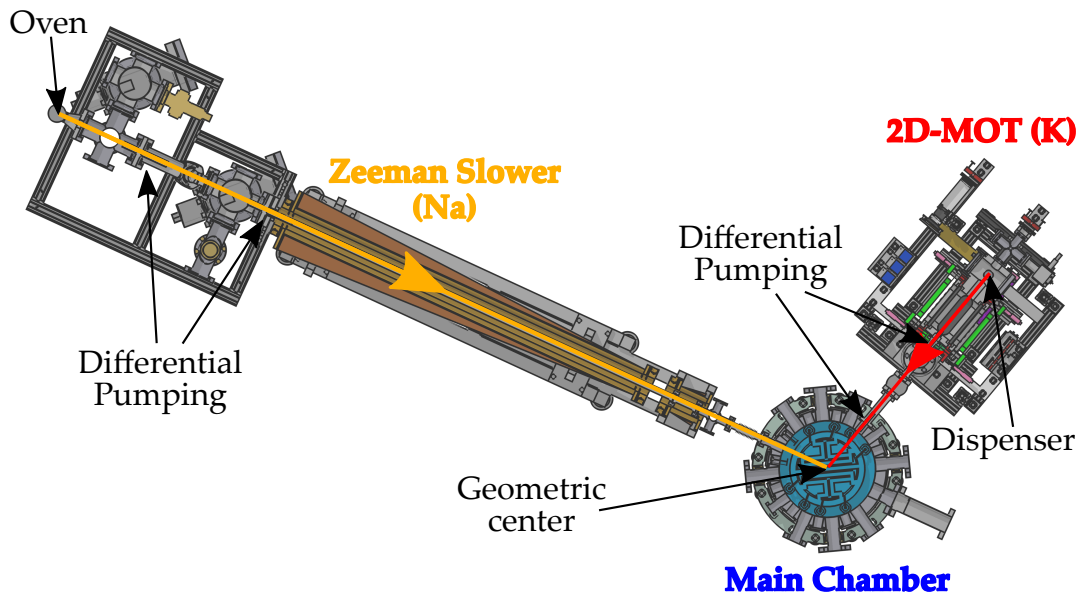


Figure 2.1: Cut of vacuum chamber, view from the top. The cut is at beam height, 300 mm above the surface of the optical table. The Zeeman slower creates a cold beam of sodium atoms, the 2D-MOT a cold beam of potassium, both going to the main chamber. In the main vacuum chamber, the atoms in the beams are then trapped in a 3D-MOT. All further steps of the experiment take place at the center of the main chamber. To ensure a good vacuum in the main chamber it is separated from the atom sources by differential pumping stages.

The ultra low temperatures are achieved in a multi-step process: Cold atomic beams of ^{23}Na and ^{40}K , provided by a Zeeman slower [75] and a two-dimensional magneto-optical trap (2D-MOT) [76], are loaded into a three-dimensional magneto-optical trap (3D-MOT) [77], in which temperatures down to the Doppler limit (^{23}Na : 240 μK [78]; ^{40}K : 145 μK [79]) can be reached. To increase the density of atoms the 3D-MOTs can

be substituted by dark spontaneous force optical traps (darkSPOTs) [80]. From those magneto-optical traps the atoms are transferred into a common magnetic trap [81], in which the mixture is cooled by evaporation [82, 83] of sodium [84]. At sufficiently low temperatures the sample is loaded into a crossed optical dipole trap, where it is cooled to quantum degeneracy [85]. In the dipole trap the atoms are associated to heteronuclear $^{23}\text{Na}^{40}\text{K}$ Feshbach molecules [86, 87, 88, 89] which are subsequently transferred to their absolute rovibrational ground state by stimulated Raman adiabatic passage (STIRAP) [90, 91]. The efficiency of the molecule creation can be increased by first transferring the atoms into a three-dimensional optical lattice, aiming for conditions in which all sites are filled with one atom of each species, before the molecules are associated [92, 93]. The ground state molecules can be used to investigate dipolar interactions in quantum-many-body systems, by varying the external confinements, or polarizing the molecules using an electric DC field. Systems in periodic potentials can be realized using a three-dimensional optical lattice with a site spacing of 532 nm. The polarizing of molecules using electric DC fields is described in detail in Chapter 3. To determine the effect of externally applied parameters the molecular sample has to be imaged. An objective which allows for high resolution imaging of atoms in an optical lattice is discussed in Chapter 4.

The vacuum chamber of the experiment is shown in Fig. 2.1. It is separated in three different regions: In the oven region of the Zeeman slower and the 2D-MOT the partial pressures of sodium and potassium are relatively high, because the creation of cold atomic beams requires a large supply of the respective atoms. In contrast, a long lifetime of atomic clouds in the magnetic trap, which is essential for reaching ultra low temperatures by evaporation, relies on excellent vacuum, on the order of 10^{-11} mbar [84]. For this reason, the oven region of the Zeeman slower and the 2D-MOT are separated from the main chamber with two differential pumping stages, each sustaining four orders of magnitude pressure difference. Also, the atomic beams can be interrupted, either by a pneumatic shutter, as in the case of the Zeeman slower, or by switching off the lasers and the magnetic fields, as in the case of the 2D-MOT.

2.1.2 Internal States - Energetic Structure of Ground State

Preparing later sections, the following paragraphs give a short overview of the ground state of heteronuclear alkali dimers [94]. As alkali atoms have only one valence electron it is reasonable to treat the molecules as a formation of two nuclei and two electrons. The Born Oppenheimer approximation separates the Hamiltonian in the electronic and nuclear contributions. This separation of the Hamiltonian leads to the potential energy curves which are plotted as a function of the internuclear separation, as sketched in Fig. 2.2.

A full treatment of the molecular Hamiltonian, which is not attempted here, would also consider angular momentum couplings. Their energetic order is represented by the different Hund's cases. Hund's case (a) is the basis for the commonly used spectroscopic notation of diatomic molecules. In this case the combined orbital angular momentum of all electrons L couples strongly to the internuclear axis. Its projection onto the latter is given by Λ : Σ , Π , Δ , ... A strong spin-orbit coupling results in the projection of the spin

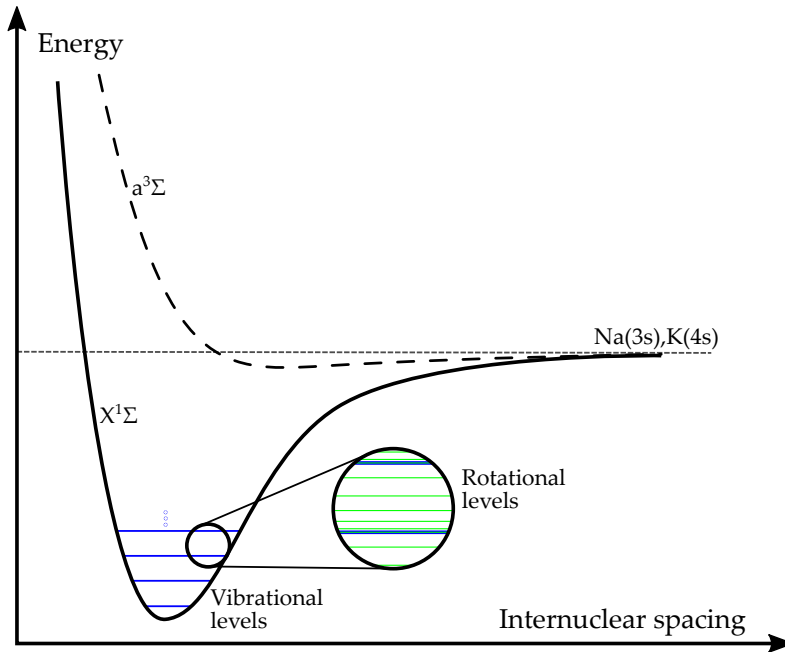


Figure 2.2: Sketch of the lowest potential energy curve $X^1\Sigma^+$ of an alkali dimer. The energies of vibrational and rotational levels of the nuclei are indicated as blue and green (light) lines. The black dashed line illustrates the $a^3\Sigma$ potential energy curve which is important for the Feshbach association and the STIRAP. The light dashed line indicates the asymptotic energy.

onto the internuclear axis. Finally, the combined projections of L and S couple with the rotation N to a total angular momentum J . The typical nomenclature, emphasizing the strong coupling of L to the internuclear axis, is:

$$X^{2S+1}\Lambda_{g/u}^{+/-}$$

Here, the first letter labels the potential energy curve, with X referring to the lowest of these. $2S + 1$ denotes the multiplicity of the spin, $+/-$ the symmetry regarding a plane containing the internuclear axis. The gerade/ungerade symmetry ($'u/g'$), expressing the electronic parity, is not applicable in the case of heteronuclear dialkalis. For the lowest potential energy curve of NaK the notation is

$$X^1\Sigma^+$$

The next higher potential is

$$a^3\Sigma$$

In Fig. 2.2 those potential curves are illustrated as a black, solid and black, dashed line. The Feshbach molecules created in the experiment are mainly supported by the $a^3\Sigma$ potential, giving them triplet spin character. The electronic ground state, ultimate goal of the molecule assembly, obviously belongs to the $X^1\Sigma^+$ potential and has singlet character.

STIRAP can bridge the transition between the triplet and the singlet state via coupling to an intermediate state which has admixture of both characters [95]. Such states are found in energetically higher potential energy curves, for example those belonging to the Na(3s) K(4p) asymptote.

The ground state potential energy curve of NaK is about $158 \text{ THz} \times h$ deep [96] and supports rotational and vibrational degrees of freedom. In the rovibrational ground state their energies can be approximated by $E_{\text{rot}} = BN(N + 1)$ and $E_{\text{vib}} = \hbar\omega_{\text{vib}}(\nu + 1/2)$.

The rotational constant B defines the energy scales necessary for polarizing a ground state alkali dimer. It can be determined using the reduced mass m and the average separation of the nuclei R_{ave} : $B = \frac{\hbar}{2mR_{\text{ave}}^2} \frac{h}{2\pi}$. Together with the molecule's internal dipole moment d' , which originates in the asymmetric electronic structure of heteronuclear molecules, the rotational constant B defines the electric field $\mathcal{E}_c = B/d'$, necessary for polarizing the molecules, as shown in Chapter 3.

2.2 Laboratory Requirements

The setup of the devised experiment requires a room of about 40 m^2 . As the laboratory conditions in this room can have an impact on the stability of the experiment, temperature and humidity are stabilized by an air conditioning (KOSS) to $(21.3 \pm 1)^\circ\text{C}$ and less than 60%, respectively. All components of the experiment which are sensitive to the ambient conditions are placed on one of the three optical tables ($1.2 \times 2.4 \text{ m}^2$, TMC) that can be isolated against vibrations with a pneumatic system. Flow-boxes (KOSS, Neuberger) installed above the optical tables, further stabilize the temperature on these to $(22.0 \pm 0.1)^\circ\text{C}$ and protect the optics from dust. The performance of the air conditioning is illustrated in Appendix A.2. If necessary, water cooling can be applied to individual components. A circulation cooling system (KÜHLMOBIL, Van der Heijden) stabilizes the water temperature to 22.0°C .

Two of the optical tables are filled with all the laser systems necessary for this experiment, including lasers for cooling and trapping atoms, as well as lasers which are used to transfer molecules to their electronic ground state. On the third (non-magnetic) optical table the vacuum chamber of the experiment was set up. In this vacuum chamber the actual experiments with ultracold atoms are performed. This requires optical components, coils for magnetic fields, electrodes for electric fields and many more things to be placed on this table, too.

All the components which need to be automatically controlled during a run of the experiment are connected to a control system (Adwin-Pro, Jäger Messtechnik) that can be programmed using a computer interface (LabView). During a run of the experiment the control system executes the complete sequence, i.e. no manual control is possible, except for an interrupt. The control system regulates all connected components via digital (TTL) or analog ($\pm 10 \text{ V}$) signals. Its timing is derived from a 100 kHz reference frequency which divides the experiment sequence in steps of $10 \mu\text{s}$. Anything which has to happen on faster timescales has to be triggered and runs independently from then on. The control system is absolutely fundamental to make timing accurate and results reproducible.

2.3 Main Chamber

The central part of the experiment is the main vacuum chamber in which nearly all steps of the experiment sequence are performed. Only the cold atomic beams, sources of the atoms, are created in the Zeeman slower and the 2D-MOT. Every other step is performed in the main chamber. Here many things come together, during the design and the experiment. A horizontal and a vertical cut of this chamber are shown in Fig. 2.3, with the major beam paths indicated.

It is a flat cylindrical chamber that is closed with two CF200 flanges¹ on the top and bottom. Two windows of 160 mm diameter are recessed in these CF200 flanges. In the horizontal plane the chamber has 22 ports of different diameter, ranging from CF16 to CF40. The four pairwise opposing CF40 windows are used for the laser beams of the 3D-MOT, the dipole trap and the optical lattice. Together with the vertical axis these CF40 windows define the main coordinate system. The axes of this coordinate system provide the most optical access to the vacuum chamber.

The large windows are recessed in the CF200 flanges. Their accessible diameter is 136.7 mm, which makes the vertical axis certainly the most prominent. The windows are recessed to reduce the spacing between them to 22 mm. On the one hand a certain spacing is necessary to provide a large volume for the 3D-MOT, on the other hand high resolution imaging as well as the creation of high electric and magnetic fields favor small spacings. The 22 mm are a good compromise. Sufficiently large 3D-MOT beams can pass. High magnetic (Section 2.5) and electric (Chapter 3) fields, as well as high resolution imaging (Chapter 4) can also be implemented.

The electric fields, required to polarize molecules, can be created using electrodes that are coated on the vacuum side of the CF200 windows. The coating is made from transparent, electrically conductive indium tin oxide (ITO). As several electrodes are coated on each of the two windows the ITO layer is not continuous. Chapter 3 explains how the geometry of the electrodes is optimized to create extremely uniform electric fields. Close to the perimeter of the vacuum window each of the ITO electrodes is covered with a gold patch. These gold patches are provided to mechanically connect the electrodes to 20 kV high voltage feedthroughs, via beryllium-copper contacts. Both, the gold patches and the beryllium-copper contacts are very well visible in Fig. 2.4.

As the windows are recessed, the coils creating the magnetic fields, for the 3D-MOT, the magnetic trap, and the Feshbach resonances, are also recessed in the CF200 flanges, bringing them closer to the atoms. A detailed description of the coils is given in Section 2.5, the mount of the lower coil is visible in Fig. 2.4.

The axes of the major coordinate system are used for the laser beams of the 3D-MOT, the optical dipole trap and the optical lattice, as well as for imaging. The latter is enabled by a combination of dichroic and flipping (KSHM 65, Owis; timescale 1 s) mirrors. The different beams are color coded in Fig. 2.3.

In the vertical direction, two lenses for imaging are mounted over the chamber. All vertical laser beams enter the vacuum chamber from below. The 3D-MOT beams for sodium (589 nm) and potassium (767 nm) are overlapped on a dichroic mirror (Laser

¹ CF is like ConFlat®, however not necessarily from Varian.

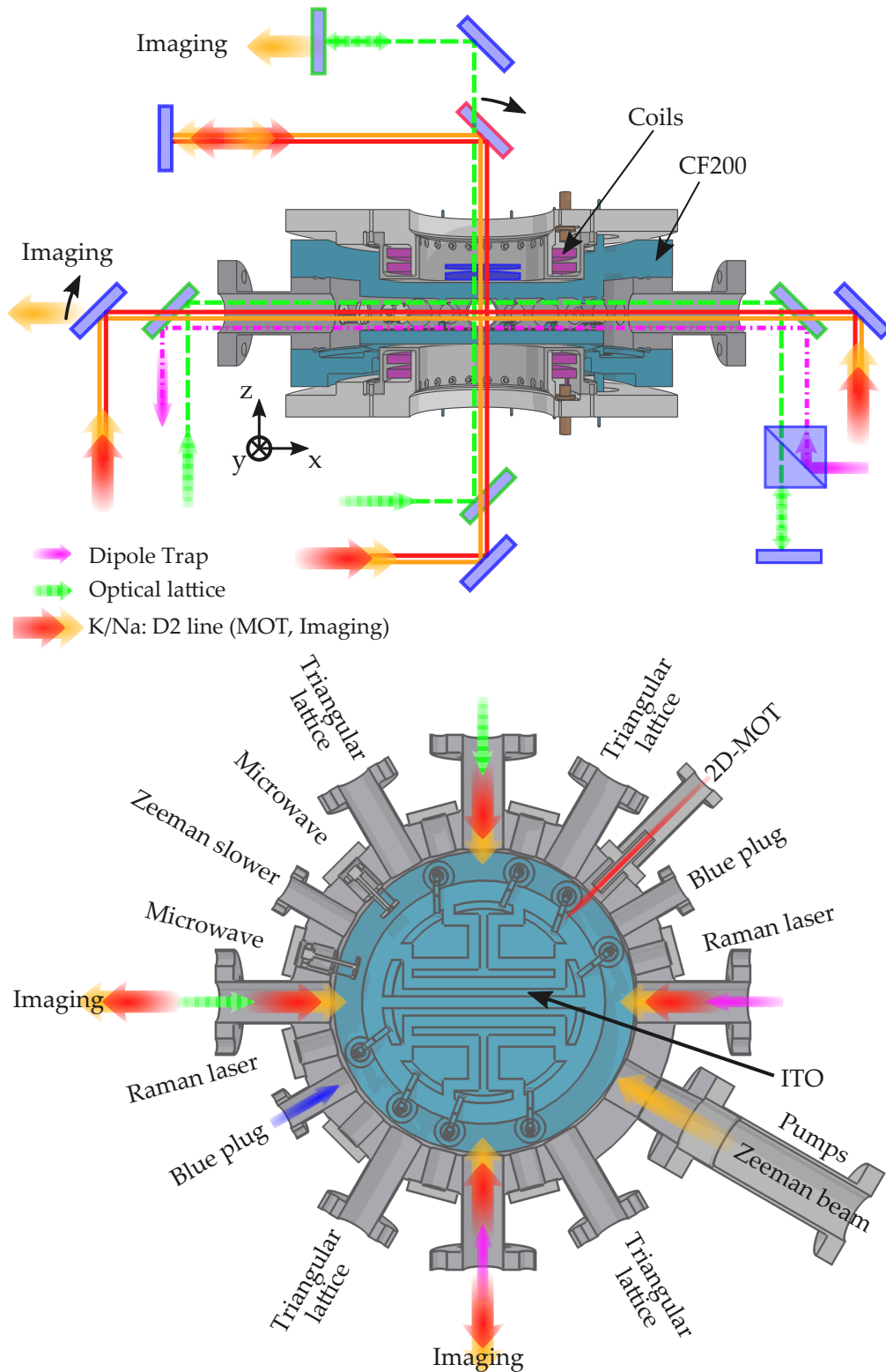


Figure 2.3: Vertical and horizontal cut of the main vacuum chamber. All beam paths are color coded. The vertical cut also shows the position of the coils of Section 2.5. The CF200 flanges with the main vacuum windows for creating electric DC fields are colored blue. The indium tin oxide coating discussed in Chapter 3 is indicated. The small bent arrows indicate flipping mirrors.

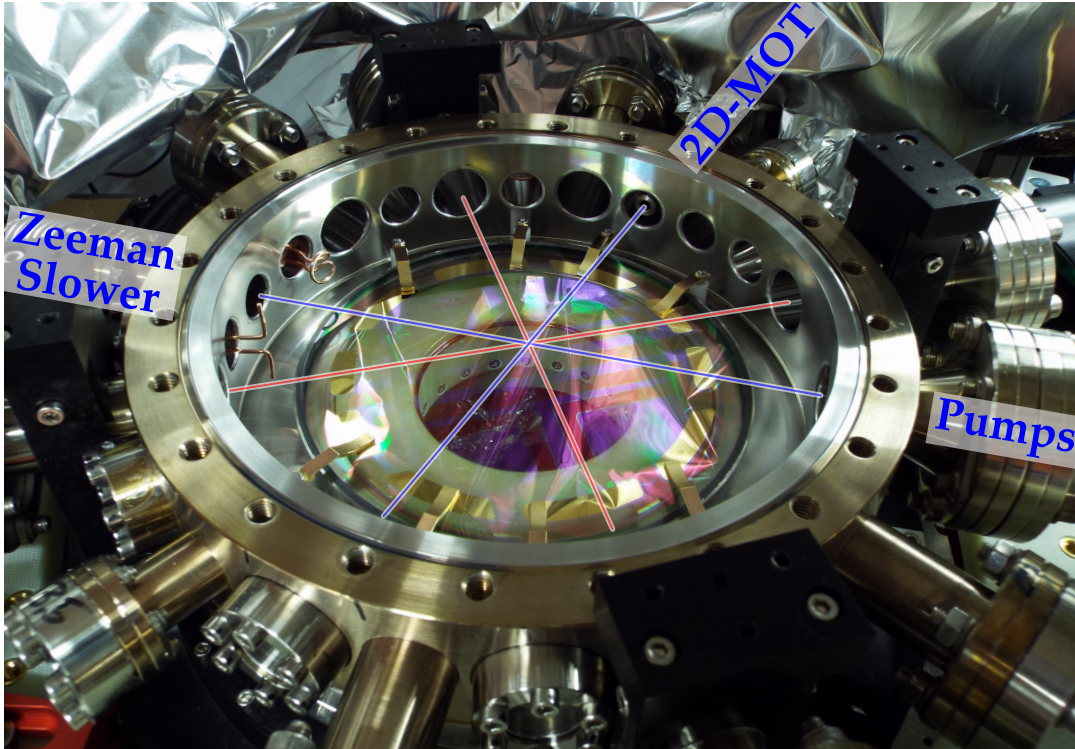


Figure 2.4: Picture of open main chamber. The top CF200 flange is taken off. The blue lines indicate the axes of the Zeeman slower and the 2D-MOT, the red lines the horizontal axes of the coordinate system. On the left and right of the Zeeman slower port a dipole and a small loop in-vacuum antenna are visible. The electrodes on the lower window can be seen as a slight violet shimmer. Their gold patches, as well as the beryllium-copper contacts are clearly visible. Through the lower window the mount of one of the coils, creating the magnetic field gradients and Feshbach fields, can be seen.

Optik). Again, a dichroic mirror is used to overlap them with the vertical lattice beam (1064 nm). After the chamber, the 3D-MOT beams and the lattice beams are again separated with a dichroic mirror and independently retro-reflected using cat eye configurations. For imaging along the vertical axis, the dichroic mirror over the chamber can be flipped. In this case the imaging light uses the same beam path as the lattice light and is later separated by a dichroic mirror. Due to the large optical access on the vertical axis high resolution imaging can be implemented. The design of a suitable objective will be discussed in Chapter 4.

On the horizontal axes the situation is very similar, except that the 3D-MOT beams are not retro-reflected. The intensity of each beam can be adjusted independently, which can be used to shift the position of the 3D-MOT. The 3D-MOT beams and the lattice beams are overlapped in the same way as on the vertical axis. The setup allows for two additional laser beams in the horizontal plane to realize an optical dipole trap at 1064 nm. They enter the vacuum chamber in the opposite directions of the lattice beams. Due to orthogonal polarizations of the lattice and the dipole trap, their beams can be overlapped and separated. To image the atoms along the horizontal axes, the 45° mirrors reflecting the 3D-MOT light into the main chamber can be flipped, similar to the vertical

axis. Absorption images are taken by illuminating the sample from the opposite window.

In addition to the three main axes, further ports provide access to the main chamber. In 45° with respect to the main horizontal axes the 2D-MOT and Zeeman slower are flanged to the chamber. Their opposite ports are reserved for the exit window of the pushing beam, in case of the 2D-MOT, and for the entrance window of the Zeeman slowing beam. Figure 2.3 indicates that these beams cross the main chamber having a direct impact on the 3D-MOT. Further ports are reserved for two in-vacuum microwave antennas, a dipole and a small loop, the blue plug of the magnetic trap, the Raman lasers and a possible triangular lattice.

The height of horizontal beams entering the main chamber is 300 mm above the optical table. The optics around the main chamber are either mounted on the optical table, or on breadboards made of fiber reinforced plastic, with brass threads (Hippe). All optics necessary to create the beams of the dipole trap and the optical lattice are mounted below the breadboards. They were prealigned on flipped breadboards. For the necessary fine adjustment the beams can be aligned by motorized mirror mounts (8821, New Focus).

Directly connected to the entrance port of the Zeeman slowing light are the ion pump (75S-DI-4V-SC-N-N, Gamma Vacuum) and the titan sublimation pump (ST22, VG Scienta) of the main chamber. The current lifetime of ^{23}Na in the unplugged magnetic trap is about 4 s while the pressure on the ion pump controller reads $1.4 \cdot 10^{-11}$ mbar (14 nA). Additional information on those measurements is given in Section 2.5.

2.4 D2 Line Laser Systems

The light for the Zeeman slower, the 2D-MOT and the 3D-MOTs is created by two laser systems. One operates on the sodium, the other on the potassium D2 line, i.e., at 589 nm and 767 nm, respectively. The fundamental requirements on these setups are given by the linewidth of the sodium $\Gamma_{\text{Na}} = 2\pi \cdot 9.792(13)$ MHz and potassium $\Gamma_{\text{K}} = 2\pi \cdot 6.035(11)$ MHz transitions. The required power can be estimated from the saturation intensities.

Light on the D2 lines is not only needed during the first cooling stages of the experiment. The laser systems are, e.g., also used to image the atoms or to optically pump atoms to a certain hyperfine or magnetic state. Both laser systems are mounted on breadboards (B60120AE, Thorlabs) which are placed on one of the optical tables. The light is transmitted to the experiment via polarization maintaining single mode fibers (PM630-HP and PM780-HP, Thorlabs). The following two paragraphs give a short overview of both systems.

2.4.1 Potassium Laser System

For trapping, cooling and manipulating potassium, the experiment relies on a system of diode lasers and tapered amplifiers, frequency locked to the crossover of the D2 line in a ^{39}K Doppler free absorption spectrum. Figure 2.5 shows the level schemes of ^{39}K and ^{40}K .

Laser cooling of ^{40}K requires light which is some Γ_{K} red detuned with respect to the closed $4^2\text{S}_{1/2}$, $F = 9/2$ to $4^2\text{P}_{3/2}$, $F' = 11/2$ cycling transition. The repump light, which

transfers atoms decaying into the $4^2S_{1/2}$, $F = 7/2$ level back into the closed cooling transition, is close to the $4^2S_{1/2}$, $F = 7/2$ to $4^2P_{3/2}$, $F' = 9/2$ transition. Many of the single components of this system were already described in a previous work [97].

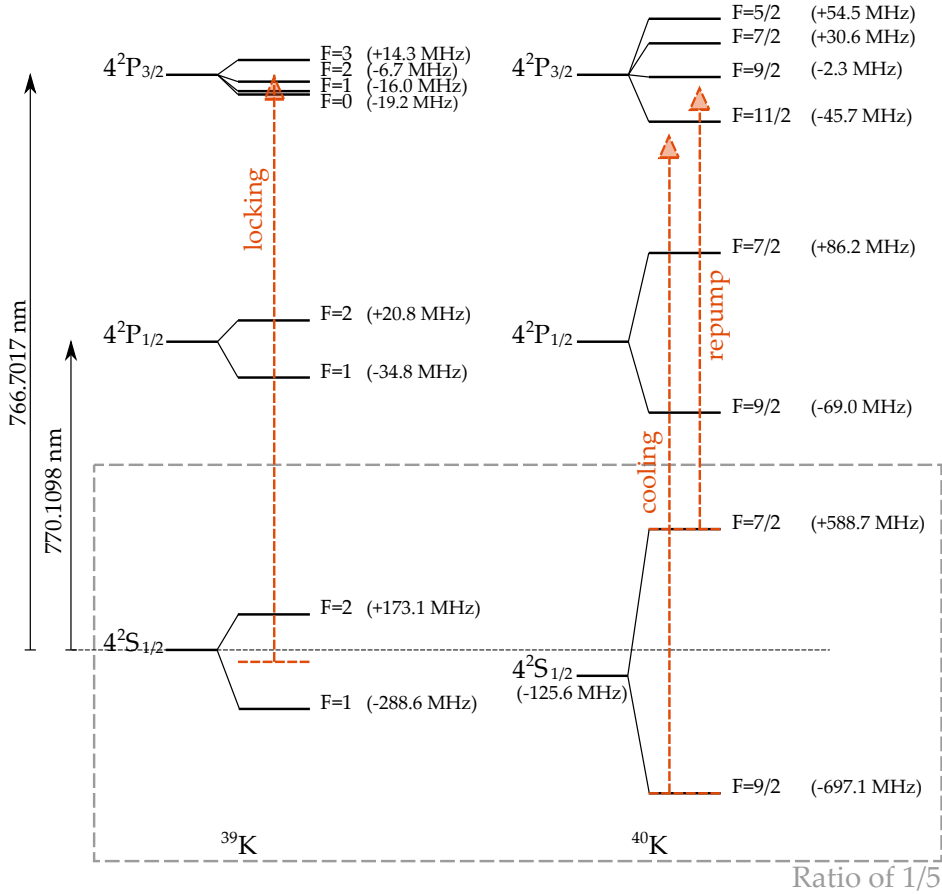


Figure 2.5: Level scheme of ^{39}K and ^{40}K . Note the inverted hyperfine structure of ^{40}K . The frequencies are relative to the respective fine structure. The dashed red arrows illustrate the locking of the master laser on a cross over in the ^{39}K spectrum, as well as the cooling and repump transitions in ^{40}K , indicating a slight red detuning of the latter lasers. This figure was also shown in [97]. The data is taken from [79].

An overview of the laser system is given in in Fig. 2.6. The frequency stability of the lasers is provided by a Doppler free frequency modulation spectroscopy [98]. Due to the low natural abundance of ^{40}K , it is convenient to lock a master laser to the crossover line in the ^{39}K D2 line spectrum, as indicated in Fig. 2.5. The frequency stability of the master laser is transferred to the cooling and repump lasers, for ^{40}K , by frequency offset locking. In both cases a single mode optic fiber coupler (F-CPL-S12785, Newport) is used to combine about 1 mW of the light with 1 mW of light from the master laser. The combined light is beat on an amplified fast photo diode (ET-2030A-FC, EOT). The signal of the photo diode is amplified and mixed with a stable reference. An analog circuit, shown in Appendix A.3, converts the frequency difference of the photo diode signal and the stable reference to an error signal which is used to stabilize the frequency spacings to the

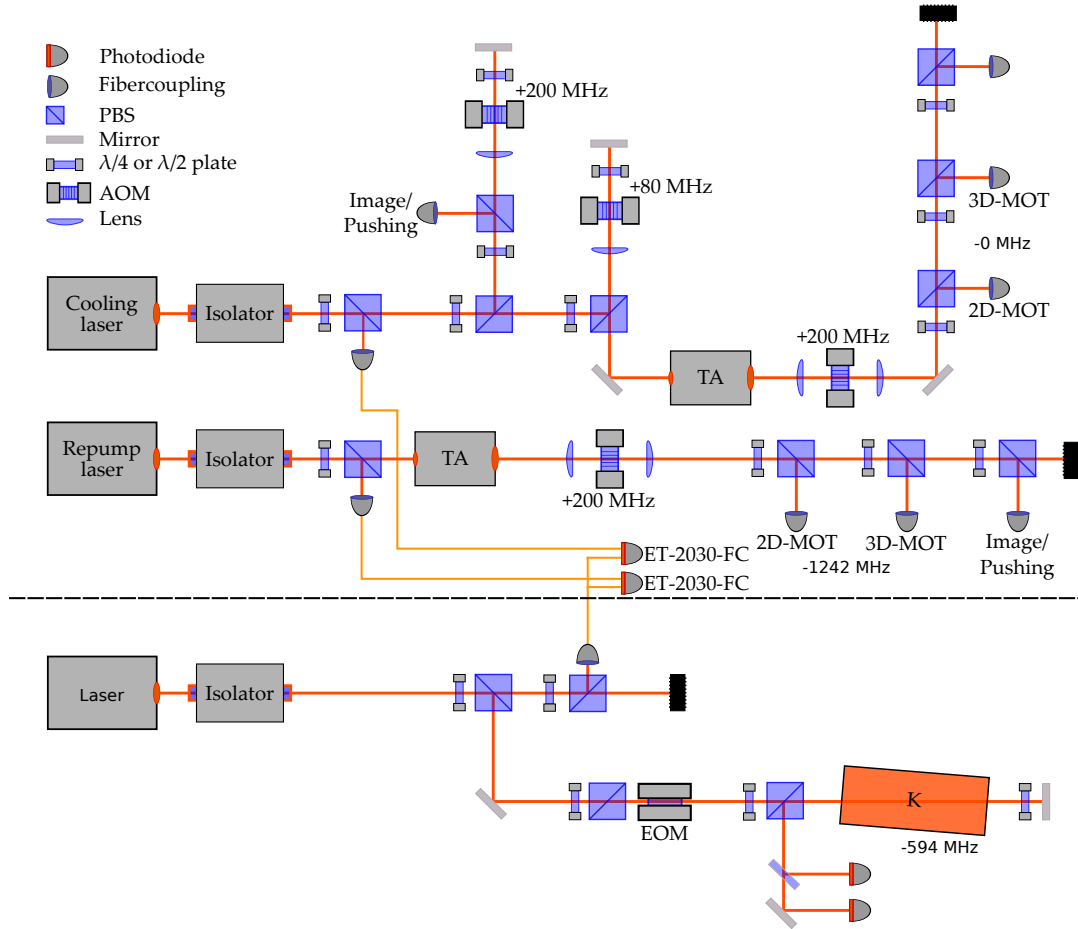


Figure 2.6: D2 line laser system for potassium. The dashed line indicates the two separated breadboards. In the lower section the frequency modulation spectroscopy of ^{39}K is shown. The vapor cell is marked by a K. The cooling and repump laser are shown in the upper section. Their power is increased by two tapered amplifiers (TA). The center frequencies of all AOMs are given. When double pass operation is indicated, the according frequency shift is twice the given number. The light is coupled into optical fibers and transmitted to the optical table. Labels indicate the purpose of the light which is coupled into the regarding fiber.

master laser via a proportional-integral (PI) controller. The offset locking scheme allows to switch between the cooling of ^{40}K and ^{39}K within a few minutes.

After the cooling and repump lasers are both amplified with a tapered amplifier, the light is split in different beams each serving a specific purpose in the experiment. With the help of acousto optic modulators (AOMs) each beam can be switched on and off on the timescale of microseconds. As AOMs do not switch the beam completely and some residual light leakage cannot be avoided, additional mechanical shutters are required. They operate on the timescale of a few milliseconds. The AOMs are also required to slightly shift the frequencies of the different beams with respect to one another. Light used for imaging, e.g., is closer to the atomic resonance than the red detuned cooling light of the 3D-MOT.

Before the cooling laser is amplified, a small amount of light is separated by means

of a PBS and frequency shifted by a 200 MHz AOM in double pass configuration. This light is used for the push beam of the 2D-MOT and for imaging. Like for all other shifts induced by AOMs in the potassium laser system, the frequency change of the light is to a higher value. The other light is shifted by a 80 MHz AOM, also in double pass configuration, before it is amplified. The amplified light is finally shifted by a 200 MHz AOM in single pass configuration and coupled in two separate fiber ports for the 2D-MOT and the 3D-MOT.

The repump laser is directly amplified and afterwards frequency shifted by a 200 MHz AOM in single pass configuration. It is also coupled in two fiber ports for the 2D-MOT and the 3D-MOT, and also an additional port for the push beam and imaging. The frequencies are also shown in Fig. 2.6.

Considering the shifts of the AOMs, the cooling laser itself operates 229 MHz blue detuned with respect to the master laser, the repump laser is 846 MHz red detuned. Those values and the respective power levels are listed in Table 2.1.

| ^{40}K | $\Delta\nu_{cool}$ MHz | $\Delta\nu_{rep}$ MHz | P_{cool} mW | P_{rep} mW |
|-----------------|------------------------|-----------------------|-------------------|-------------------|
| 2D-MOT | +229 | -846 | 90 | 45 |
| Pushing | +269 | -846 | $2 \cdot 10^{-4}$ | $1 \cdot 10^{-4}$ |
| 3D-MOT | +229 | -846 | 100 | 50 |

| ^{39}K | $\Delta\nu_{cool}$ MHz | $\Delta\nu_{rep}$ MHz | P_{cool} mW | P_{rep} mW |
|-----------------|------------------------|-----------------------|---------------|--------------|
| 2D-MOT | -587 | +18 | 90 | 45 |
| 3D-MOT | -587 | +18 | 90 | 45 |

Table 2.1: Parameters of the potassium laser system. The tables list the frequencies and powers for which 3D-MOTs of ^{40}K and ^{39}K were obtained. The frequencies are given with respect to the master laser. A '+' indicates a blue detuning, '-' a red detuning.

2.4.2 Sodium Laser System

For manipulating sodium a commercial system (MPB Communications Inc.) combining a fiber amplifier and a frequency doubling stage is used. The system is seeded by a distributed feedback laser diode (LD-1178-0030-DFB-1, Toptica) at a wavelength of 1178.3 nm. The fiber amplifier amplifies the seeding light which is subsequently frequency doubled to the required 589.2 nm. The output power of the complete system is specified to reach up to 2 W. A level scheme, indicating the cooling and the repump transition of sodium is shown in Fig. 2.7.

To obtain the various frequencies which are necessary to operate the Zeeman slower and the 3D-MOT, to polarize the atomic sample and to image it, the output of the frequency doubling is split in different beams. Their frequencies are individually shifted with AOMs. For the cooling beam of the Zeeman slower, an electro optic modulator (EOM) is used to implement the repumping light as a sideband on the cooling light. In detail, the sodium system will be described in [100]. Table 2.2 lists the frequencies

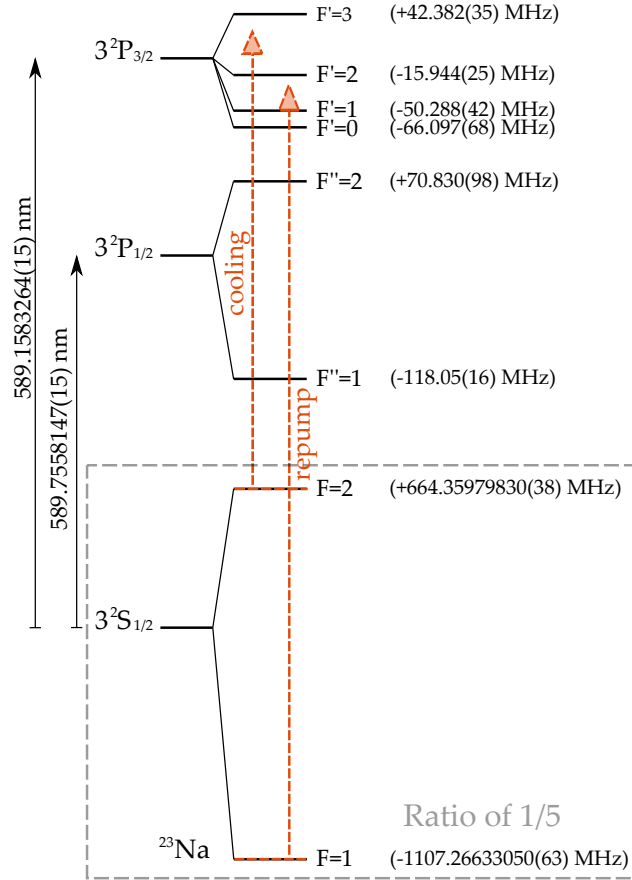


Figure 2.7: Level scheme of ^{23}Na . The frequencies are relative to the respective fine structure. The red, dashed arrows illustrate the cooling and repump transitions indicating a slight red detuning of both lasers. Illustration is based on data from [99].

| ^{23}Na | ν_{cool} MHz | ν_{rep} MHz | P_{cool} mW | P_{rep} mW |
|--------------------|------------------|-----------------|---------------|--------------|
| Zeeman | -605 | +1108 | Total: 80 | |
| 3D-MOT | -220 | +1510 | 125 | 15 |
| Pumping to $F = 1$ | -205 | - | 0.5 | - |
| Pumping to $F = 2$ | - | +1508 | - | 0.5 |
| Spin polarizing | -208 | - | 5.0 | - |
| Imaging | -205 | +1508 | | |

Table 2.2: Parameters of the sodium laser system. The table lists the parameters for which a 3D-MOT of ^{23}Na was obtained. The detunings are given with respect to the locking point of the laser (205 MHz blue of the $F=2$ to $F'=3$ transition). A '+' indicates a blue detuning, '-' a red detuning.

and powers which were found to be ideal for operating the experiment. The frequencies are given with respect to the locking point of the laser which is 205 MHz blue of the $3^2S_{1/2}$, $F = 2$ to $3^2P_{3/2}$, $F' = 3$ cooling transition.

2.5 Magnetic Fields

Besides light, the second important component to experiments with ultracold gases are magnetic fields. They act on the atoms' magnetic moments, and thus in first order on the magnetic sub-levels of the hyperfine structure. Magnetic fields are used in two major configurations. Magneto-optical and magnetic traps utilize the minimum of a strongly inhomogeneous magnetic field, whereas the manipulation of atoms via Feshbach resonances requires a uniform magnetic field magnitude at the location of the atoms.

In this experiment, both types of fields are created by a single pair of coils that is centered with respect to the vertical axis of the main chamber. When the electric currents in these coils are flowing in the same [opposite] direction, a homogeneous magnetic field [magnetic field minimum] is created at the center of the main chamber. Due to geometric constraints the coils deviate from the ideal Helmholtz configuration for homogeneous magnetic fields. The ratio between the on-axis distance of the coils $2d$ and the coil radius R is $2d/R = 4/3$, instead of 1. Therefore, homogeneous magnetic fields will be disturbed by a curvature term (Eq. (2.1)).

For a detailed description, the fields created by the pair of coils can be calculated with the equations given in [101], and the sources listed therein. Accordingly, the fields obtained from a pair of wire loops can be expanded along the symmetry axis of the coils, which coincides with the vertical z -axis of the main chamber. The following equations show the expansions for the Helmholtz and anti-Helmholtz configuration, with μ_0 being the vacuum permeability and I the electric current flowing in the loops:

$$B_H(z) = B_0 + B_2 z^2 + \mathcal{O}(z^4) = I \frac{R^2 \mu_0}{(d^2 + R^2)^{3/2}} - 1.5I \frac{(-4d^2 + R^2) \frac{R^2 \mu_0}{(d^2 + R^2)^{3/2}}}{(d^2 + R^2)^2} z^2 \quad (2.1)$$

$$B_{aH}(z) = B_1 z + \mathcal{O}(z^3) = 3I \frac{dR^2 \mu_0}{(d^2 + R^2)^{5/2}} z. \quad (2.2)$$

The corresponding expansions along the horizontal (radial) directions x and y are obtained when dividing the factors B_1 and B_2 by a factor of two. For $R = 51$ mm, which is the central radius of the coils used in this experiment and the ratio $d/R = 2/3$ the Eqs. (2.1) and (2.2) predict an approximate homogeneous field of $B_H = 0.142 \frac{\text{G}}{\text{A}} + 0.00305 \frac{\text{G}}{\text{Acm}^2} z^2$ and a gradient field of $B_{aH} = 0.0385 \frac{\text{G}}{\text{Acm}} z$ for each pair of windings. Because the coils do not resemble an ideal Helmholtz configuration, the quadratic term in the homogeneous field does not cancel. A more thorough calculation for the configuration used in the experiment is given in the next paragraphs.

2.5.1 Coil Design

The pair of coils creating the magnetic fields in this experiment were designed by computing their magnetic fields and testing the thermal stability of a prototype. A cut of the upper coil is shown in Fig. 2.8. The lower coil is the exact mirror image. The actual coils

are depicted in pink. They are split in two layers of windings which are wound on a structure of fiber reinforced plastic, shown in gray. The mount fully encloses the coils, and can be flooded with water to cool the coils. It provides an optical access of 80 mm diameter to the main chamber.

The upper part of the mount (light gray) is a rigid structure which is directly mounted to the construction holding the vacuum chamber. The coils are directly wound on this upper part of the mount, in order to increase their rigidity. The lower part of the mount (dark gray) serves as the water basin and should not experience any mechanical stress. After the parts are connected and sealed the mount can be flooded via two inlets. The outlets are on the opposite side.

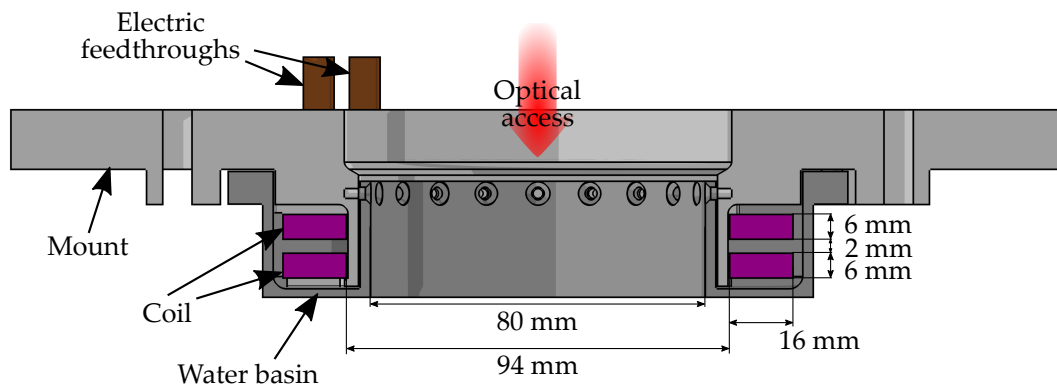


Figure 2.8: Vertical cut of top coil. The actual coil (pink) has 2×12 windings of $6.0 \times 1.2 \text{ mm}^2$ wire, gapped by 2 mm. The upper mount (light gray) is a rigid structure of fiber reinforced plastic. The coil is directly wound and glued to this structure. The water basin (dark gray) enclosing the coil experiences no mechanical stress, except the dynamic water pressure. Its thinnest walls are 2.5 mm. The lower coils is a mirror image of the top coil. The red arrow indicates the vertical optical axis of the main vacuum chamber.

The geometry of the setup does provide space for two layers of twelve windings with a wire of $6.0 \times 1.2 \text{ mm}^2$ cross section, not including the $\lesssim 0.1 \text{ mm}$ thick insulating coating. The gap between the two layers of windings is 2 mm wide. The inner diameter of the coils is 94 mm. Their vertical spacing to the center of the chamber is 27 mm.

The Electric feedthroughs connecting the coils to the outside are copper rods of 8 mm diameter. This will prevent electrochemical reactions with the coil wires and reduce ohmic heating of the uncooled feedthroughs. The feedthroughs are sealed with o-rings.

For the simulation of the magnetic field it was assumed that each winding can be approximated by a thin wire loop at its center. Again, the equations from [101] are used to simulate the resulting magnetic fields. For the anti-Helmholtz configuration the simulation predicts a magnetic field gradient of $0.408 \frac{\text{G}}{\text{Acm}}$ in the horizontal and $0.815 \frac{\text{G}}{\text{Acm}}$ in the vertical direction. In Helmholtz configuration the expected field is $3.361 \frac{\text{G}}{\text{A}}$ with a curvature of $0.0228 \frac{\text{G}}{\text{Acm}^2}$ in the horizontal and $0.0456 \frac{\text{G}}{\text{Acm}^2}$ in the vertical direction. This is confirmed by the values which were calculated for pairs of single wire loops, above.

Both field configurations were measured with a Hall sensor (Model 7030, F.W. Bell). The results are plotted in Fig. 2.9. In the anti-Helmholtz configuration the gradient in the

horizontal direction was determined by a linear fit to be $0.41(2) \frac{\text{G}}{\text{Acm}}$. It is twice the value in the vertical direction. The magnetic field in the Helmholtz configuration was measured after the center of the geometry was determined in the anti-Helmholtz configuration. The center value of the magnetic field in the Helmholtz configuration is $3.5(2) \frac{\text{G}}{\text{A}}$ with a curvature of $0.05 \frac{\text{G}}{\text{Acm}^2}$ along the vertical direction.

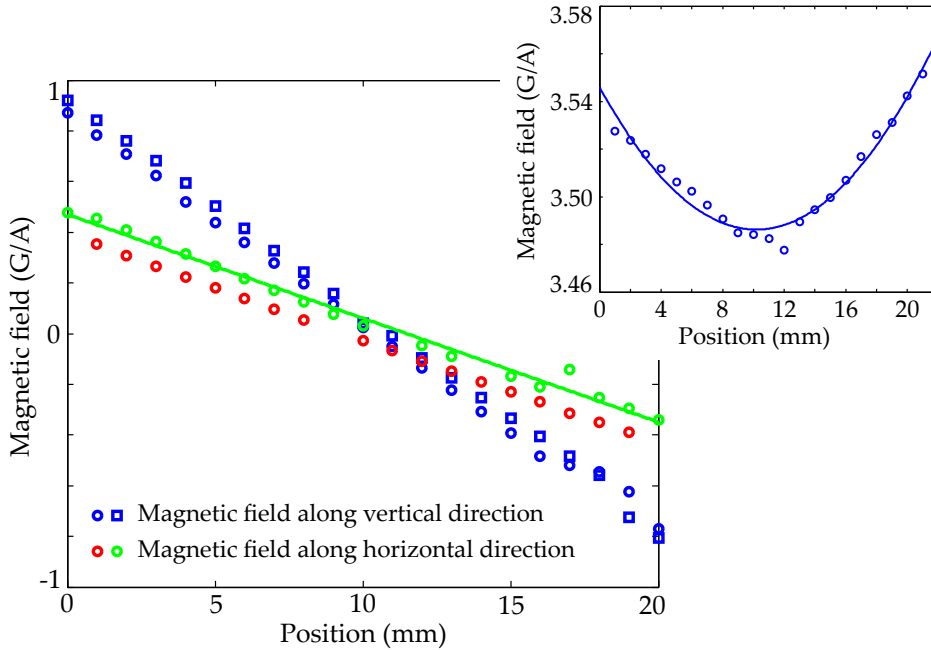


Figure 2.9: Magnetic fields measured in anti-Helmholtz and Helmholtz configuration. The main plot shows the field magnitude measured in anti-Helmholtz configuration, normalized to the current. The blue circles and squares show the field along the vertical axis and the red and green circles along the horizontal axes. The gradient in the horizontal direction is $0.41(2) \frac{\text{G}}{\text{Acm}}$. A linear fit to the green circles is shown in as a solid line.

The inset shows the normalized magnetic field in Helmholtz configuration, measured along the vertical direction. In Helmholtz configuration the field at the center is $3.5(2) \frac{\text{G}}{\text{A}}$ with a curvature of $0.05 \frac{\text{G}}{\text{Acm}^2}$ along the vertical direction.

The values of the gradient and the field magnitude measured are slightly higher than expected from the simulations. Partially, because during the measurement the coils were 1 mm closer together than in the experiment and the simulations. Accounting for this 1 mm in the simulations, a gradient of $0.41 \frac{\text{G}}{\text{Acm}}$, in the horizontal direction, and an absolute field of $3.4 \frac{\text{G}}{\text{A}}$ are predicted. This matches the measured values. Therefore, the simulated values obtained for the real spacing are reliable.

Using the currently available power supply (SM 30-200, Delta Elektronika), magnetic fields up to 670 G and magnetic field gradients up to $160 \frac{\text{G}}{\text{cm}}$ can be achieved. For the measured Feshbach resonances of ^{23}Na and ^{40}K the magnetic field magnitudes are sufficient [85, 89]. For evaporation in the magnetic trap, discussed in Section 2.8, field gradients like $220 \frac{\text{G}}{\text{cm}}$ [85] or $1000 \frac{\text{G}}{\text{cm}}$ [84] would require a power supply which provides higher currents.

In order to allow for rapid changes in the magnetic field, two one wire loops are glued on the inner perimeter of the coil mounts. They are 25 mm above or below the center of the magnetic trap and 80 mm in diameter. Due to their size and optimal location, they are also used as radio frequency or microwave antennas (Section 2.8).

In the experiment, a H-bridge based on IGBTs (CM300DY-24NF, Mitsubishi) switches between Helmholtz and anti-Helmholtz configuration of the main coils. The experiment control can initiate the switching via TTL logic [102]. The current flowing in the coils is measured with a current transducer (IT-200S Ultrastab, Danfysik) and regulated via a PI controller (Appendix A.4) that is currently directly connected to the coils' power supply.

The resistance of one coil was calculated to be 0.019Ω . At an electric current of 150 A, this leads to a dissipation of 0.4 kW. Such high powers actually require water cooling. As the coils are fully immersed, the surrounding water shields the outside, specifically the vacuum chamber, from the potentially hot coils. During the design process of the coil it was found that omitting the gap between the two layers of windings leads to thermal problems at the center of the coil when running high currents. This eventually resulted in a failure of the insulation.

The cooling efficiency for a single coil of the final design was tested at a water pressure of 2 bar, resulting in a flow of $9 \frac{\text{liter}}{2 \text{min}}$. During this test the temperature of the cooling water was measured inside the mount close to the outlet with a negative temperature coefficient thermistor. During constant operation at 150 A the cooling water was measured to warm up by 1°C . At the specified water flow, this corresponds to 0.3 kW. This deviation from the expected value can be due to two reasons. First, the thermistor might partially be shielded from the water by being glued into the mount and hence not capture the temperature increase of the water adequately. Second, also at the temperature measured at the water inlet was rising by 0.7°C , indicating a heating of the mount. Probably, not solely the water is contributing to the cooling, but heat is also transferred to the mount of the coils.

When continuously operating at 150 A and switching the cooling water on and off in intervals of 20 s (on) and 15 s (off), the maximum temperature rise at the thermistors has been measured to be 5.6°C . Indicating a slow heat transfer to the water, other mechanisms of heat transfer, or a not adequate measurement the water temperature.

The water pressure at the inflow is currently limited to 3 bar, which corresponds to $12 \frac{\text{liter}}{2 \text{min}}$. Leak tests at 5 bar with open outlet and 3 bar with closed outlet were passed by the system. Nevertheless, when the temperature of a thermistor in the coil mount rises above 60°C , an interlock turns the power supply of the coils off.

2.5.2 Compensation Cage

Residual magnetic fields at the location of the atoms are undesirable, especially when the system is sensitive the magnetic field, like during an optical molasses, or state preparation. In this setup, residual magnetic fields can be compensated with three pairs of coils set up around the optical table in a cube like configuration. Each coil is approximately quadratic with a edge length of 1.2 m. On the one hand they do not block the optical access to the experiment and create a more uniform field in a given spatial volume than smaller coils. On the other hand, considering Eq. (2.1), it is sufficiently harder to create

strong magnetic fields with such large coils.

To have a large number of uncluttered windings each coil of the compensation cage is formed by a 50-wire cable (Ölflex Classic 110 50 G 2.5, Lapp Kabel). All wires of a coil are connected in series, resulting in an overall resistance of about 2.2Ω . The field created by each pair of opposing coils can be adjusted with a pair of power supplies (PS 3032-20 B, Elektro Automatik) that are connected to the experiment control.

For one pair of coils simulations predict a gradient of $0.0081 \frac{\text{G}}{\text{Acm}}$ along the axial direction, in the Anti-Helmholtz configuration. Along the same axis the field obtained in the Helmholtz configuration is $0.38 \frac{\text{G}}{\text{A}}$ with a curvature of $0.000079 \frac{\text{G}}{\text{Acm}^2}$. At currents of 12 A, magnetic fields as high as 4.5 G are achieved.

2.6 Laser Cooling

Based on the major technical components described above, the experiment sequence for the creation of an ultracold atomic mixture can be built up step by step. A sequence always starts with laser cooling of atoms [103, 104], which was one of the most important ideas for the field of ultracold atomic gases. It can be used to cool an atom from room temperature to theoretically a few hundred microkelvin², which corresponds to a decrease in temperature of about six orders of magnitude.

The principle of laser cooling is described in many textbooks [78]: An atom is decelerated by absorbing counter propagating photons and spontaneously re-emitting them, in random directions. Assuming the kinetic energy of the atom, or the mean kinetic energy of an atomic ensemble can be related to temperature, the atom is cooled when it scatters photons in the above stated manner.

Due to the randomness of the spontaneous emission, the smallest temperatures achievable with this cooling method are given by the Doppler temperature $T_D = \frac{\hbar\Gamma}{2k_B}$ [78]. This temperature is usually significantly higher than the photon recoil limit $T_R = \frac{(\hbar k)^2}{2mk_B}$ [78] which is, at least as long as the atoms continuously scatter photons from the light field, the lower limit for laser cooling. It can in principle be achieved with so called sub-Doppler techniques, like polarization gradient cooling. Above Γ is the linewidth of the transition that is used for cooling, m the mass of the particle to be cooled, k is the absolute value of the wave vector given by $k = \frac{2\pi}{\lambda}$, with λ being the wavelength of the cooling light. The Boltzmann constant is denoted k_B . Some cooling methods involving lasers and achieving temperatures below the recoil limit were reported [105, 106].

2.6.1 Cases of ²³Na and ⁴⁰K

To cool an average atom from room temperature below the mK regime, it has to scatter on the order of 10^4 to 10^5 photons. This is only realistic for atoms providing a fast, closed cycling transition, on which they can continuously scatter photons. In alkali atoms such cycling transitions exist between certain hyperfine states of the $^2S_{1/2}$ ground state and the $^2P_{3/2}$ state situated thereover. Luckily, those transitions are well accessible with lasers.

² Including sub-Doppler techniques even a few μK .

Sodium atoms (^{23}Na) are cooled on the transition between the $3^2\text{S}_{1/2}, F = 2$ and the $3^2\text{P}_{3/2}, F' = 3$ level, labeled ‘cooling’ in Fig. 2.7. It has a linewidth of $\Gamma_{\text{Na}} = 2\pi \times 9.792(13)\text{MHz}$ [107], allowing a high photon scattering rate. Also it is closed, because atoms excited to the $F' = 3$ level can only decay to $F = 2$. Nevertheless, with a finite probability the cooling light excites atoms to the $F' = 2$ or $F' = 1$ levels, from which they can decay to $F = 1$. Due to the large hyperfine splitting of the $3^2\text{S}_{1/2}$ ground state, the atoms decaying to $F = 1$ cannot be excited by the cooling laser and are lost from the cooling transition. This leak can be closed by ‘repumping’ the lost atoms with a second laser, preferably to the $F' = 2$ level from which they can again decay into the cooling transition.

For potassium (^{40}K) the situation is very similar. A level scheme is shown in Fig. 2.5. The cooling laser operates on the transition between the $F = 9/2$ and $F' = 11/2$ levels. A repump laser on the $F = 7/2$ to $F' = 9/2$ transition closes the cycle. The according linewidth in ^{40}K is $\Gamma_{\text{K}} = 2\pi \times 6.035(11)\text{MHz}$ [79], which is nearly on the order of sodium.

2.6.2 Zeeman Slower

In a Zeeman slower [75], a collimated flux of atoms with small transversal velocities is slowed along the axial direction by resonantly scattering counter propagating photons. The scattering is continuous, as a tailored magnetic field ensures that the Doppler shift expected at a certain location along the slower is compensated by the Zeeman splitting.

A Zeeman slower is a very good option to create large samples of ultracold atomic sodium [108]. A typical slower is divided in two sections: In the first section a lump of sodium is heated in an oven, increasing the sodium vapor pressure. The atoms escape the oven through a nozzle, creating a flux of hot atoms with low transverse velocities. Thereafter, in the second section, this atomic beam is axially slowed by laser cooling. This axial slowing heats the beam transversally. When an atom was slowed by scattering n_p photons, it has gained about $\sqrt{n_p}\hbar k$ transverse momentum. Hence, a short spacing between the Zeeman slower and the 3D-MOT is important. A cut of the Zeeman slower implemented in this experiment is shown in Fig. 2.10.

In the oven a few gram of solid sodium are heated to 360°C , corresponding to a vapor pressure of 0.3mbar [109]. The hot vapor leaves the oven through a nozzle of 2mm diameter. The atomic flux is indicated by the dash-dotted arrow. Behind the nozzle, the setup allows to cool the flux of atoms in the transverse directions by a two-dimensional optical molasses. After the oven section the atoms pass two differential pumping stages, which ensure that the vacuum in the main chamber can be maintained. They also cut atoms with high transversal velocities from the beam. Between the differential pumping stages, the atomic flux can be interrupted by a pneumatic shutter.

At the end of the second differential pumping stage, the axial slowing of the atoms begins. The laser beam, slowing the atoms, is aligned with the central axis of the slower. In Fig. 2.10 it is indicated by a long yellow arrow pointing from right to left. The magnetic field, created by the coils, ensure that, even though the velocity of the atoms decreases along the slower, they are continuously on resonance with the cooling laser. As the slower is of the spin-flip type it has two coils for creating the magnetic field, partially combining the advantages of a decreasing field slower and an increasing field slower. The increasing part at the end of the Zeeman slower allows to detune the slowing light far enough from

the cooling transition to reduce its effect on the 3D-MOT. The decreasing part in the beginning keeps the magnetic field at the end of the slower reasonably low, not to affect the 3D-MOT. A third, optional coil ensures a fast drop of the magnetic field at the end of the slower, quickly shifting the atoms out of resonance with the slowing light. The combination of a decreasing and an increasing field requires to ‘flip the spin’ of the atoms between the two main coils of the slower. Implying that between the two sections the direction of the magnetic field is adiabatically reversed, i.e. the magnetic moments of the atoms follow the change of the quantization axis. This reverses the quantization axis compared to the polarization (helicity) of the cooling laser and hence the atoms are pumped to the magnetic quantum numbers of opposite sign.

The slower of this experiment is designed to capture atoms up to a velocity of $900 \frac{\text{m}}{\text{s}}$, which corresponds to 68% of the atoms in the Maxwell-Boltzmann distribution of the oven. To achieve this capture velocity the magnetic field magnitude decreases from 850 G to 0 G, before rising to about 300 G again. This final field magnitude is determined by the detuning of the slowing laser and the expected capture velocity of the 3D-MOT, which is $30 \frac{\text{m}}{\text{s}}$. The frequency detuning of the slowing laser beam with respect to the cooling transition is 400 MHz.

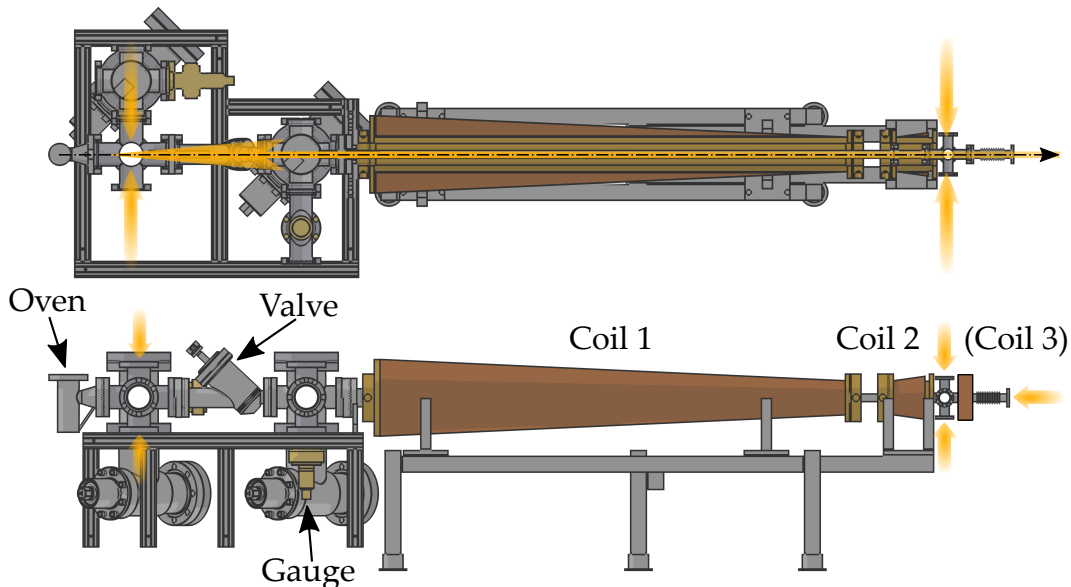


Figure 2.10: Sketch of Zeeman slower. The upper picture shows a view from the top, the lower picture from the side. A dash-dotted arrow indicates the atomic flux. The long yellow arrow pointing from right to left illustrates the slowing beam. It counter propagates the atomic beam. The other yellow arrows indicate potential locations for transversal cooling. The brown trapezoid structures depict the magnet coils which create the Zeeman splitting. A third small coil can be used to tailor the magnetic field at the end of the slower.

Due to the high pressure in the oven, the vacuum system of the Zeeman slower involves two differential pumping stages. During a failure of a vacuum window one of them proved to sustain at least two orders of magnitude in pressure difference. The volume behind the oven is pumped by two ion pumps. One pumps the volume directly

after the nozzle of the oven (RVIP-55-ST-M, Rebuilt Varian), the second one the volume between the two differential pumping stages (45S-CV-2V-SC-N-N, Gamma Vacuum). A small pump (3S-CV-1V-5K-N-N, Gamma Vacuum) after the second coil of the slower, i.e. right before the main vacuum chamber, mainly serves as an indicator for the pressure. The pressure reading on the pump directly behind the nozzle is $4.0 \cdot 10^{-8}$ mbar when the oven operates at 355°C . After the first differential pumping stage the pressure at the controller of the ion pump shows $0.7 \cdot 10^{-10}$ mbar – the pressure reading on a gauge close by is however $9.1 \cdot 10^{-10}$ mbar. The small ion getter pump at the end of the Zeeman slower shows $1 \cdot 10^{-10}$ mbar. As this reading is close to the main chamber, where the ion pump reads $1.4 \cdot 10^{-11}$ mbar, the value on the small pump is higher than expected, which can result from leak currents.

In more detail the design of the Zeeman slower has already been described in [110].

2.6.3 2D-MOT

In contrast to sodium, potassium does not require a hot oven to reach the desired vapor pressures. The potassium vapor is released from a ^{40}K enriched dispenser (Alvasource-2-K40(5.5%)-5-S, Alvatec). In this dispenser the relative amount of ^{40}K is increased from 0.01% natural abundance [111] to 5.5%. The dispenser releases potassium in a chemical reaction that is thermally activated. By heating it with an electric current of 4.4 A, the vapor pressure of ^{40}K is sufficient for the operation of the 2D-MOT. Higher currents, increase the vapor pressure and recently the operation current was changed to 6.0 A.

MOTs [77] combine laser cooling with a confining potential. The confinement results from the Zeeman splitting in a magnetic (quadrupole) field and the correct polarization of the red detuned, cooling laser beams with respect to the local axis of the magnetic field. In a 2D-MOT [76] the confinement and laser cooling are reduced to the two transverse directions, leading to the formation of a cold atomic beam along the axial direction.

In this experiment, the 2D-MOT is created in a custom made 316LN stainless steel vacuum chamber which is illustrated in Fig. 2.11. The red arrows indicate the laser beams used for cooling and repumping. The coil mounts are shown in green coloring. The elongated vacuum windows through which the cooling beams of the 2D-MOT enter are sealed with indium.

As illustrated in Fig. 2.11, three retro-reflected beams along both transverse directions are used for the cooling. Those beams are split from a single beam of 20 mm diameter, using polarizing beam splitting cubes (PBSs). To reduce the spacing between the beams, the PBSs are placed as close together as permitted by the $\lambda/2$ -plates between them. The circular polarization necessary for a MOT is achieved by $\lambda/4$ -plates directly after the PBSs and in front of the retro-reflecting mirrors. As the cooling and repump light arrive on the experiment table with perpendicular polarizations the first transversal cooling beam of each direction gets half of the total laser power, the other two a quarter, each. For the performance of the 2D-MOT it is essential that the last transversal cooling beam does not clip on the differential pumping stage to the main chamber. The resulting stray light would destroy the atomic flux. The respective power of the cooling and repump light are listed in Section 2.4.

The coils creating the magnetic field for the 2D-MOT are wound of $4 \times 2 \text{ mm}^2$

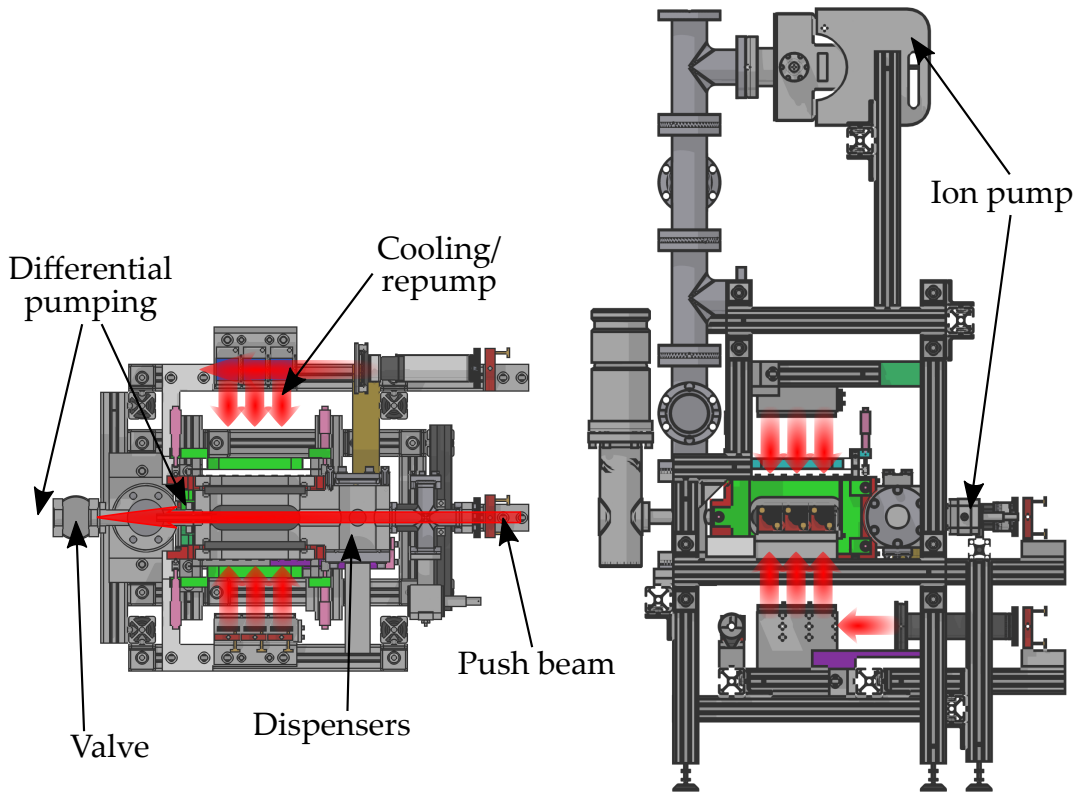


Figure 2.11: Sketch of 2D-MOT. The left picture shows a cut of the 2D-MOT vacuum chamber in the plane of the horizontal cooling beams. The right picture is a side view. Red arrows indicate the retro-reflected transversal cooling beams and the pushing beam. With an all-metal inline valve the 2D-MOT can be separated from the main chamber. Two differential pumping stages maintain the pressure in the main chamber during operation.

wire. When operated at the same current they create a magnetic field gradient of $B_1 = 0.57(2) \frac{\text{G}}{\text{cmA}}$ in the transverse directions. Currently they run at 38 A, 34 A, 39 A, 35 A (top, bottom, left, right). These asymmetric currents shift the trap zero, i.e. the axis of the cold beam in the transverse plane, such that it overlaps with the two differential pumping stages, leading to the main chamber. The high currents in the coils might result from the bad performance of the $\lambda/4$ -plates in the system.

In addition to the transversal cooling, an axial push beam can be used to accelerate the transversally cold atoms at the center of the 2D-MOT in the direction of the main chamber. This reduces the transverse divergence of the beam and adds atoms which initially moved away from the main chamber to the flux. The push beam is transmitted from the laser table to the experiment via two optical fibers containing cooling and repump light. On the experiment the cooling and repump light are combined with a fiber splitter. To clean the polarization the pushing beam first passes a linear polarizer. After having diverged to a diameter of 10 mm, it is focused (AC254-045-B, Thorlabs, $f = 45 \text{ mm}$) over a distance of 50 cm onto a spot slightly behind the first differential pumping stage. In the volume of the 2D-MOT it has a maximal diameter of 2 mm. Before entering the vacuum

chamber the beam is attenuated with neutral density filters and its polarization is converted to circular using a $\lambda/4$ -plate. We preliminary found an optimum power of $0.3 \mu\text{W}$ for the pushing beam, which enhances the performance by a factor of 1.4.

To sustain a good vacuum in the main chamber even at high pressures in the 2D-MOT, both are separated by two differential pumping stages. Each of these should be able to maintain a pressure difference of two orders of magnitude. Between these two differential pumping stages an ion pump reads a pressure of $0.9 \cdot 10^{-10}$ mbar. During the operation this pressure rises to about $2.5 \cdot 10^{-10}$ mbar which can be considered uncritical because of the following differential pumping stage.

2.6.4 3D-MOT

The cold beams of ^{23}Na and ^{40}K atoms, created in the Zeeman slower and the 2D-MOT, intersect in the main chamber where they are captured in respective 3D-MOTs [77]. A scheme of the main chamber is depicted in Fig. 2.3. The beam diameters of the 3D-MOT are about 20 mm. The used laser powers are listed in Section 2.4. As both 3D-MOTs use the same magnetic field, created by the coils described in Section 2.5, their locations overlap. A separation can only be achieved by adjusting the light pressures for the two different atomic elements independently. Higher final densities in the 3D-MOTs can be obtained by switching to dark spontaneous force optical traps (dark SPOTs) [80]. In the central region of this MOT like configuration the atoms are not repumped into the cooling transition anymore, reducing loss processes due to collisions involving excited atoms and radiation trapping.

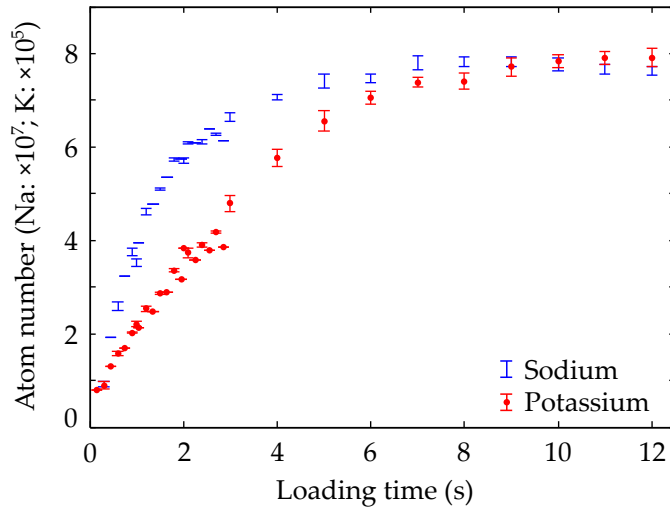


Figure 2.12: Simultaneous loading of ^{23}Na and a ^{39}K 3D-MOTs. Both species were loaded simultaneously and subsequently their fluorescence was recorded as a function of loading time. For an estimation of the atom number the y-axis has to be scaled with 10^7 [10^5] for ^{23}Na [^{39}K]. The error bars indicate the root means square error over multiple measurements. Few points were only recorded once, hence their error bar has zero extend.

Until now 3D-MOTs of ^{23}Na , ^{39}K and ^{40}K were loaded independently. A combined operation of a ^{23}Na and a ^{39}K 3D-MOT was only recently attempted. The corresponding loading curves are shown in Fig. 2.12. It was reported that potential losses in a double species 3D-MOT can be circumvented by first loading ^{23}Na and shelving it in a shallow magnetic trap while loading the 3D-MOT of ^{40}K [85]. This could not be tested, yet, as the main vacuum chamber in the setup described here is currently replaced (Section 2.7).

2.7 Magnetic Trap

Direct cooling of atoms with light is finally limited by the photon recoil energy³ of the cooling light. Magnetic traps [81], which confine atoms in a local minimum of the magnetic field, do not require light and are not limited by the recoil energy. This makes them ideal for trapping atomic samples at extremely low temperatures.

However, unlike MOTs, magnetic traps do not have an intrinsic mechanism that cools the atomic sample⁴. The extremely low temperatures have to be reached with additional techniques, like evaporative cooling which is considered in Section 2.8.

For efficient magnetic trapping the internal states of the atoms have to be prepared. After the 3D-MOT, they are pumped into a single hyperfine state F which contains several magnetic sub-levels, labeled m_F . At zero magnetic field those sub-levels are degenerate. At a finite magnetic field B their energy is shifted by

$$U_{\text{mag}} = g_F m_F \mu_B B, \quad (2.3)$$

with g_F being the hyperfine Lande g -factor and μ_B the Bohr magneton.

As a static magnetic field in free space can only have a local minimum, but no maximum [112], only the sub-levels with $g_F m_F > 0$ can be trapped in a potential created by magnetic fields. It is beneficial to pump all atoms into the sub-level with the largest $g_F m_F$, providing the strongest confinement.

Preparing the sample in such a stretched state also prevents losses due to spin relaxation. When the atomic sample is not spin polarized the timescale of spin relaxation depends significantly on the density of the sample. Assuming a rate coefficient of $10^{-11} \frac{\text{cm}^3}{\text{s}}$ [113] the relaxation can happen very fast for samples with densities of $10^{13} \frac{1}{\text{cm}^3}$, or extremely slow when the density is only $10^8 \frac{1}{\text{cm}^3}$. Other loss processes due to inelastic collisions, namely, dipolar relaxation and three body recombination, also become only relevant at high densities, where the latter will dominate [114].

While preserving substantial optical access, the magnetic quadrupole field created by the coils introduced in Section 2.5 goes to zero at its center which can violate the adiabatic condition

$$\mu_B B \gg \hbar \frac{|\dot{B}|}{B}, \quad (2.4)$$

³ Some cooling schemes involving lasers were reported to reach sub-recoil temperatures [105, 106].

⁴ Certainly there might happen some evaporative cooling in the magnetic trap itself, but this is not relevant on the timescale of typical experiments.

implicitly assumed when writing Eq. (2.3). At the center of the quadrupole trap the energetic splitting of the magnetic sub-levels is too small to ensure that the atoms' magnetic moments follow the quantization axis (direction of the magnetic field) adiabatically. Consequently, losses from the magnetic trap due to spin flips to untrapped states are reported [84, 115]. A scaling for the loss rate [115] is given by

$$\frac{1}{\tau} \sim \frac{\hbar}{m} \frac{1}{l^2}, \quad (2.5)$$

with m being the mass of an atom and l the characteristic length scale of the trap. In [72] losses due to spin flips became relevant at several 10 μK . Temperatures below about 10 μK were only achieved by optically plugging the trap. Besides the idea of optically plugging the center of the trap [2], other solutions preventing these losses at the center of the magnetic trap rely on magnetic background fields [115, 116, 117, 118]. In this experiment the trap can be plugged with a laser at a wavelength of 532 nm, preserving the advantages of a steep confinement [119, 115]. Detailed information on the 'blue' plug can be found in [120].

At high temperatures and low densities, such as after loading the atoms in the magnetic trap, most losses are due to collisions with residual background gas atoms. Therefore very good ultrahigh vacuum is required at the location of the magnetic trap.

2.7.1 Magnetic Trapping of ^{40}K

In the case of ^{40}K in the $F = 9/2$ level, all the states with magnetic quantum numbers $m_F > 0$ are magnetically trappable. For the $F = 7/2$ level all states with $m_F < 0$ can be trapped. For $F = 9/2, m_F = +9/2$ and $F = 7/2, m_F = -7/2$ the energy shifts due to the Zeeman effect are 1.40 MHz/G and 1.09 MHz/G, respectively.

In this experiment the atoms are transferred to the magnetic trap by keeping the coils already used for the 3D-MOT (Section 2.5) in anti-Helmholtz configuration and increasing the current by a factor of 1.5 to compress the 3D-MOT. When spatial overlap between the compressed 3D-MOT and the magnetic trap is achieved the cooling and re-pump lasers are switched off, successively, pumping all atoms into the $F = 9/2$ hyperfine state. After the lasers are off the magnetic gradient is ramped to 42 G/cm along the radial direction in 4 ms total ramp time.

After having transferred the atoms to the magnetic trap, the lifetime of the sample in the magnetic trap can be determined. For this measurement atoms were held in the magnetic trap for a certain time before they were re-trapped in a 3D-MOT. The fluorescence of the atoms in the 3D-MOT was imaged for a defined time and a two-dimensional Gaussian was fitted to the image. In the inset of Fig. 2.13 the volume of this Gaussian is plotted as a function of the time the atoms were held in the magnetic trap. Here, the decay time of an exponential fit to this data is the lifetime of the sample.

Unfortunately the lifetime in our magnetic trap has been decreasing over time: This decrease was verified after several bakings of the main chamber. For a time period of two months, starting April 24, 2015, the lifetime of ^{40}K in the magnetic trap is plotted in Fig. 2.13. In the first days after baking and firing the titanium sublimation pump the measured lifetime increased, while the current reading for the ion pump of the main

chamber decreased. When the controller of the ion pump showed a current of 4.6 nA the lifetime was measured to be 51(4) s. After this peak the lifetime started to decrease, while the current on the ion pump still showed a low reading. Nevertheless, the decreasing lifetime is attributed to a deteriorating vacuum at the location of the atoms.

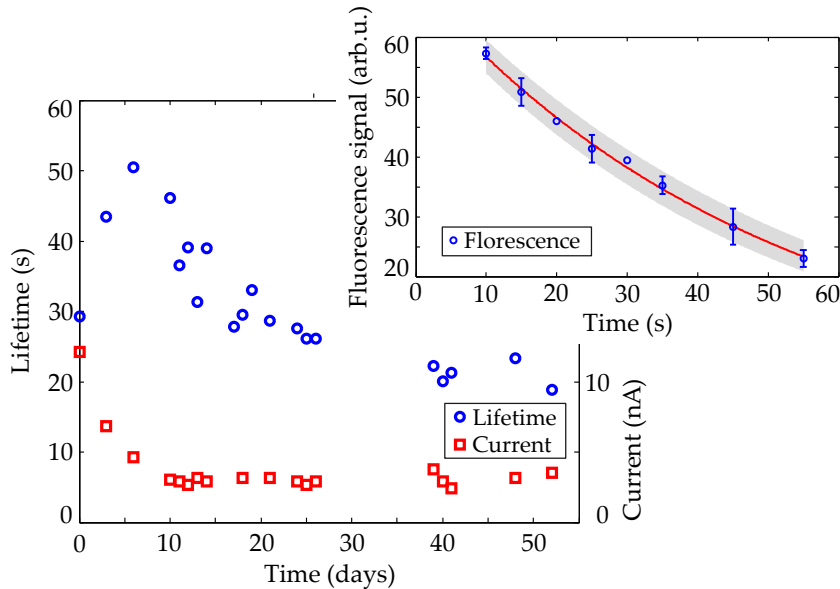


Figure 2.13: Decay of the lifetime. The blue circles in the main plot show the lifetimes of ^{40}K in the magnetic trap over a time period of two month starting at April 24, 2015. The red squares show the current on the ion pump of the main chamber in nA.

The inset shows the fluorescence signal of atomic samples, which were re-trapped in a 3D-MOT, as a function of the time they had been trapped magnetically. This data was taken on April 30, 2015, before the lifetime started to decrease. An exponential fit, shown as a red line suggests a lifetime of 51(4) s.

The inset of Fig. 2.13 shows the decrease of the atom number during a lifetime measurement. This decrease is well fitted by a exponential decay, indicating so called one-body collisions⁵, i.e. collisions with the background gas. However, the strongest indicator towards a vacuum related problem is that the decrease of the lifetime was measured after several bakings. Also, no relation between the lifetime of an atomic sample and the gradient of the magnetic trap was found, opposing two-body collisions. Actually, the decrease plotted in Fig. 2.13 is the slowest measured until now. The reason for this is not certain. Compared to previous measurements the pumping speed for some gases was increased by adding two getter pumps (Capacitorr CF16-172-2X16-10-PL, SEAS) directly to the main chamber. At the beginning of October 2015 the lifetime (measured with ^{23}Na) was about 4 s.

Until now this decrease of the lifetime cannot be attributed to a certain source. For a longer period of time the indium tin oxide (ITO) coating of the main windows was suspected to release impurities, which is not entirely unreasonable [121]. Nevertheless, after covering the ITO with an additional anti-reflection coating, a decrease of the lifetime is

⁵ It should be mentioned that two-body collisions could fit the data nearly equally well.

still observed. Plenty of others possible sources for contamination exist, also the chamber itself could be problematic. Therefore, a new vacuum chamber is set up. Due to air baking the new chamber should have a reduced hydrogen out gassing rate compared to the current chamber. Additionally, the new chamber has a larger pumping cross section. Chapter 5 will provide the latest details on the lifetime in the new vacuum chamber.

2.7.2 Magnetic Trapping of ^{23}Na

In sodium the energy shifts due to the Zeeman effect are 1.40 MHz/G and 0.702 MHz/G for the $F = 2, m_F = +2$ and $F = 1, m_F = -1$ states, respectively. This makes the trapping potential of sodium in the $F = 2, m_F = +2$ state very similar to the trapping potential of potassium in the $F = 9/2, m_F = +9/2$ state.

The lifetime of ^{23}Na in the magnetic trap did decrease like the lifetime of ^{40}K .

2.8 Evaporation and Microwaves

To reach quantum degeneracy evaporative cooling schemes [82, 83, 115, 84, 114] are still the only feasible method [1, 2, 3]. During evaporative cooling the hottest atoms of a thermally equilibrated sample are steadily removed on timescales which allow the sample to continuously re-equilibrate, thereby lowering the average energy of the sample. Due to low densities the re-equilibration in cold atom experiments can be very slow. Accordingly, it was found that slower ramps can result in larger Bose Einstein condensates [71]. The timescale of evaporation is however limited by the rate at which atoms are lost from the magnetic trap due to mechanisms which do not contribute to cooling, e.g. losses due to collisions with the background gas.

In a magnetic trap, the hot atoms can be evaporated by intentionally transferring them to an untrapped m_F state. Commonly this is achieved by slowly decreasing the frequency ν_{rf} of a radio wave, applied to the atoms, to resonantly⁶ transfer all atoms with energies higher than $m_F h \nu_{\text{rf}} - U_0$ to an untrapped magnetic sub-level with $g_F m_F < 0$, or $m_F = 0$, of the same hyperfine ground state. The floor of the potential U_0 would in our case be given by the blue detuned, plugging laser beam. This technique called radio frequency (rf) evaporation has the advantage that the depth of the trap is reduced, but the geometry of the confinement is maintained.

The same effect is achieved by transferring the hottest atoms to an untrapped magnetic sub-level of the other hyperfine ground state, by sweeping the frequency of an applied microwave (mw). When trapping two atomic species, e.g. ^{23}Na and ^{40}K this latter technique can be superior, as it addresses both species independently: In rf evaporation, the levels are continuously split by the Zeeman effect, so that a radio frequency is always resonant with transitions in both atoms, maybe at different magnetic field. With microwave evaporation, single species can be addressed due to the difference in the hyperfine splitting of the respective ground states. The hyperfine ground states of ^{23}Na and ^{40}K are split by 1770.6 MHz and 1285.8 MHz, respectively. This difference of several

⁶ $h\nu_{\text{rf}} = g_F \mu_B B$

hundred megahertz is beyond the ranges of frequency ramps required in evaporation and addressing one atomic species does not interfere with the other.

Following the equations of [113], whose notation is different from [114] but the content is essentially the same, the most important ingredients for evaporative cooling are⁷: A decrease of the particle number N has to be accompanied by a decrease of the sample's temperature T :

$$\frac{d(\ln T)}{d(\ln N)} = \beta \frac{1}{1 + \frac{\tau_{\text{ev}}}{\tau_{\text{loss}}}}, \quad (2.6)$$

an increase of the phase space density ω :

$$\frac{d(\ln \omega)}{d(\ln N)} = - \left[\beta \frac{1}{1 + \frac{\tau_{\text{ev}}}{\tau_{\text{loss}}}} \left(\frac{d}{\nu} + \frac{3}{2} \right) - 1 \right], \quad (2.7)$$

and if evaporation is to be efficient, an increase in the elastic scattering rate, quantified by the time passing between elastic scattering events τ_{el} :

$$\frac{d(\ln \tau_{\text{el}})}{d(\ln N)} = \beta \frac{1}{1 + \frac{\tau_{\text{ev}}}{\tau_{\text{loss}}}} \left(\frac{d}{\nu} - \frac{1}{2} \right) - 1. \quad (2.8)$$

Here β is the relative excess energy lost by evaporating an atom:

$$\beta = \frac{\epsilon_{\text{ev}}}{\bar{\epsilon}} - 1. \quad (2.9)$$

For $\epsilon_{\text{ev}} \gg \bar{\epsilon}$ and considering a Maxwell-Boltzmann distribution of the kinetic energy the relationship between the evaporation rate $\frac{1}{\tau_{\text{ev}}}$ and the elastic scattering rate $\frac{1}{\tau_{\text{el}}}$ is found to be

$$\frac{1}{\tau_{\text{ev}}} = \frac{1}{\tau_{\text{el}}} \frac{\epsilon_{\text{ev}}}{\sqrt{2} k_{\text{B}} T} e^{-\frac{\epsilon_{\text{ev}}}{k_{\text{B}} T}}, \quad (2.10)$$

i.e., a certain evaporation threshold ϵ_{ev} , with respect to the average energy per trapped particle $\bar{\epsilon} = \left(\frac{d}{\nu} + \frac{3}{2} \right) k_{\text{B}} T$, maximizes the evaporation rate. The relation to temperature can be obtained from the generalized equipartition theorem. Here, d is the effective dimensionality of the trap, and ν the power of the potential ($U_{\text{mag}} \sim r^\nu$) in the radial direction r . The loss processes which do not contribute to evaporation, e.g. collisions with the background gas are summarized in the rate $\frac{1}{\tau_{\text{loss}}}$.

Equation Eq. (2.6) indicates that evaporation is only efficient when the evaporation rate is fast compared to the loss rate. The combination of Eqs. (2.6) and (2.9) states that evaporation only reduces the temperature of a sample when ϵ_{ev} is higher than $\bar{\epsilon}$. But, as evaporation is only efficient when it is fast compared to $\frac{1}{\tau_{\text{loss}}}$, ϵ_{ev} cannot be chosen infinitely large, as indicated by the exponential in Eq. (2.10). Equations (2.7) and (2.8) state that traps of a lower spatial power, e.g. linear traps with $\nu = 1$, lead to a more rapid increase in phase space density and are more probable to result in runaway evaporation, which favors plugged quadrupole traps.

However, all equations indicate that for small τ_{loss} , i.e. strong losses, evaporation is not favorable.

⁷ Note, $\frac{d(\ln x)}{d(\ln y)} = \frac{\dot{x}y}{x\dot{y}}$, \dot{x} denoting the time derivative of x .

2.8.1 Evaporation in Current Situation

Considering the current lifetime $\tau_{\text{loss}} \approx 5$ s, evaporative cooling seems to be impossible in our vacuum chamber. Only a few informations are needed to derive the elastic collision rate $\frac{1}{\tau_{\text{el}}} = \sigma\sqrt{2\bar{v}}\frac{n(0)}{8}$ from experimentally determinable parameters, getting a better estimation⁸:

- At 0.2 mK the scattering cross section of sodium atoms in the $F = 1$, $m_F = -1$ state was measured to be $\sigma = (6.0 \pm 3.0) \cdot 10^{-12} \text{ cm}^2$ [84].
- The mean velocity \bar{v} can be calculated assuming a Maxwell Boltzmann distribution at 1 mK, which is currently the temperature of the sample after it was transferred to the magnetic trap: $\bar{v} = \sqrt{\frac{8k_B T}{\pi m}} = \sqrt{\frac{8k_B 1\text{mK}}{\pi 23\text{au}}} = 0.96 \frac{\text{m}}{\text{s}}$.
The temperature of 1 mK was derived by selectively removing certain velocity classes from the trap.
- The average density $\frac{n(0)}{8}$ in the quadrupole trap is calculated by using the generalized equipartition theorem $3k_B T = g_F m_F \mu_B B_1 l$, with l being the mean distance of a particle from the trap center.

Assuming $N = 10^8$ particles in the trap and an axial magnetic field gradient of $B_1 = 100 \frac{\text{G}}{\text{cm}}$ the average density of atoms in the $F = 1$, $m_F = -1$ state is

$$\frac{n(0)}{8} = \frac{3N}{4\pi l(2l)^2} = \frac{3N(g_F m_F \mu_B B_1)^3}{16\pi(3k_B T)^3} = 8 \cdot 10^6 \frac{1}{\text{cm}^3}.$$

Therefore, the elastic collision rate would be $0.007 \frac{1}{\text{s}}$. Finally, this elastic collision rate has to be divided by the amount of events needed for an atom to re-thermalize in order to get the timescale for evaporation. Sodium atoms in the $F = 1$, $m_F = -1$ ground state, being confined in a harmonic baseball trap needed 2.7 collision events⁹ to thermalize [123].

Noting that under the current conditions the lifetime in the magnetic trap is significantly below the equilibration time evaporative cooling seems to be impossible, except σ is orders of magnitude larger at 1 mK, than at 0.2 mK. Otherwise evaporation can only be effectively improved by increasing the rate of elastic collisions. This is either achieved by lower initial temperatures or a stronger confinement [115, 84]. Pumping the atoms to the $F = 2$, $m_F = 2$ ground state or increasing the magnetic gradient lead to a stronger confinement. If the initial temperature was decreased to the Doppler temperature, while the confinement was increased by a factor of 4, the initial elastic scattering rate would be higher than $10 \frac{1}{\text{s}}$.

Nonetheless, by applying a radio wave, atoms could be removed from the magnetic trap. Figure 2.14 shows the in-situ width of the atomic cloud, after the frequency of an applied radio wave was linearly decreased from 26 MHz to a final value. This final value is given on the x-axis. The frequency of the radio wave was decreased on the timescale of the lifetime $\tau_{\text{loss}} = 4$ s. The decreased width at a final frequency of 16 MHz indicates that possibly atoms with large kinetic energy were removed.

⁸ To mimic the situation of this experiment, the following calculation assumes a sample of atoms in the $F = 1$, $m_F = -1$ state, magnetically trapped in a quadrupole field.

⁹ Scattering length from $\sigma = 8\pi a^2$: $a = \pm (92(25)a_0)$ ($F = 1$, $m_F = -1$) [84];

$a = \pm (52(5)a_0)$ ($F = 1$, $m_F = -1$) [122]

$a = \pm (85(3)a_0)$ ($F = 2$, $m_F = +2$) [122].

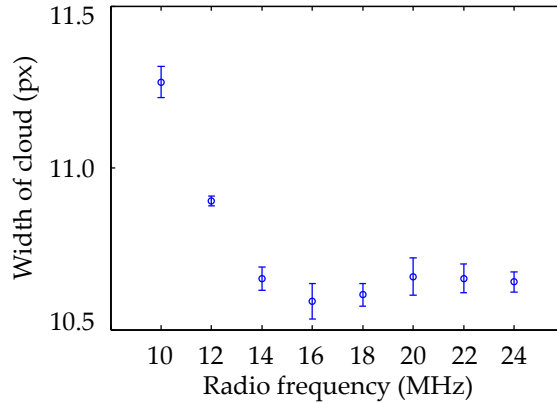


Figure 2.14: Width of atomic cloud after removal of atoms by RF ramp. Sodium atoms in the $F = 2$ state were removed from the magnetic trap by decreasing the rf from 26 MHz to a final value in 4 s. The in-situ width of the final cloud is plotted as a function of the final rf. A rf of 16 MHz corresponds to 0.77 mK. When this measurement was done the lifetime in the magnetic trap was 4 s.

2.8.2 Microwave Setup

The hyperfine splitting in the ground state of alkali atoms lies in the electronically well accessible regime of several gigahertz. Microwaves can be used to manipulate the coupling between those states, e.g. to drive transitions for evaporative cooling. For the creation of these microwaves, this experiment relies on a combination of phase locked microwave oscillators and the Toptica VFG 150¹⁰, with a frequency range from 1 MHz to 150 MHz. Mixing the signals of these frequency sources provides very stable frequencies on the one hand and high versatility on the other hand. The signals of a stable oscillator and the VFG are mixed using single sideband modulation (SSB), to suppress other sidebands and the carrier.

A sketch of the SSB circuit is shown in Fig. 2.15. Two oscillators generate microwave signals about 80 MHz above the ground state hyperfine splittings of ^{23}Na and ^{40}K (1771.6 MHz and 1285.8 MHz). The frequencies of the oscillators are 1850 MHz and 1360 MHz. They are phase locked to a 10 MHz reference. One of the two oscillators can be selected via a high frequency, high isolation switch (ZASWA-2-50DR+, Mini Circuits), which is controlled by a TTL signal of the experiment control. The signal of the selected oscillator is the carrier for the SSB.

The radio frequency signal is generated by the VFG 150 and enhanced by a low noise amplifier (ZFL-500-HLN+, Mini Circuits), before being split in two separated signals (QE-E44-442, Pulsar Microwave). Simultaneously the phase of one signal is shifted by 90° to enable the SSB. In an I/Q-mixer (MMB0102Q05LM, Meuro) the split radio frequency signals are used to modulate the carrier while suppressing the upper sideband and the carrier¹¹. Only the lower sideband is transmitted. After the modulation, the signal is additionally filtered (VLF1575, Minicircuits).

The power of the lower sideband deviates by less than 1 dB over the radio frequency

¹⁰ The properties of the Toptica VFG 150 are described in [124] and sources therein.

¹¹ The suppression can slightly be optimized by adjusting the amplitude ratio of both legs.

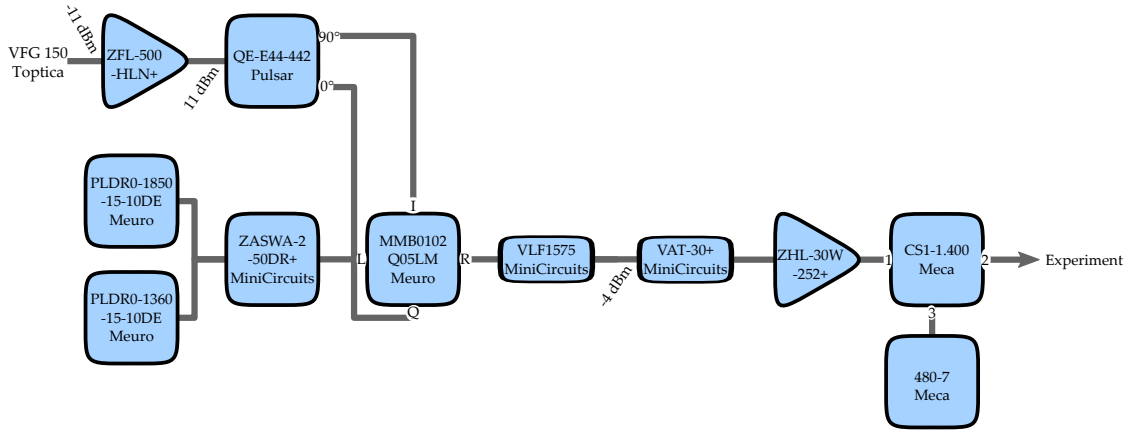


Figure 2.15: Microwave circuit. The microwave signals created with this circuit can be varied using single sideband modulation (SSB). Two oscillators locked to a 10 MHz reference provide the carrier signals for ^{23}Na and ^{40}K (1771.6 MHz and 1285.8 MHz). The modulation signal for the SSB is derive from a Toptica VFG 150. The fundamental parts for SSB are the splitter (QE-E44-442, Pulsar Microwave) and the mixer (MMB0102Q05LM, Meuro). All components are connected using SMA.

range from 10 MHz to 140 MHz. The suppression of the carrier, measured after the I/Q-mixer, is -22 dB, that of the first upper sideband¹² is -29 dB.

Close to the experiment the signal is attenuated, e.g. by 30 dB (VAT-30+, Minicircuits), before being amplified (ZHL-30W-252+, Mini Circuits) to potentially several Watt. The attenuation can be used to vary the power of the microwave signal, and more importantly suppresses noise picked up in the cable going to the amplifier. The amplified signal is sent to one of the microwave antennas of the experiment. A circulator (CS-1.400, Meca), placed between the amplifier and the antenna, prevents back reflections into the amplifier. They are dumped in an air cooled $50\ \Omega$ termination (480-7, Meca).

The Rabi frequency at the location of the atoms [125] is roughly

$$\Omega_R \approx \frac{\mu_B}{\hbar} B_{\text{mw}}, \quad (2.11)$$

B_{mw} being the amplitude of the microwave. Assuming a spherical spread of all components of the electromagnetic wave¹³, a Rabi frequency on the order of 10 kHz [126] would require the antenna to emit around 15 W of microwave power, when it is 10 cm from the atoms. Note, that the required power is quadratic in the Rabi frequency and the spacing of the atoms form the antenna. Also, especially in the near field, the relative amplitude of the magnetic field component can be beneficial.

Three loop antennas are currently available to apply radio frequency waves and microwaves to the atoms. Two of them are identical and glued on the mount of the top and bottom coil. They are about 25 mm from the center of the magnetic trap, 80 mm in diameter and their symmetry axis is centered with the atoms. Inside the vacuum chamber a small loop antenna (14 mm diameter) is available. The antenna on the lower coil

¹² At radio frequencies below 35 MHz the third order sideband is only suppressed by about -20 dB, above suppression is significantly stronger than for the carrier.

¹³ This is certainly not the case.

mount and the small loop are visible in Fig. 2.4, the dipole antenna was removed from the experiment.

The microwaves generated in this setup can be used for evaporative cooling in the magnetic trap, but also to selectively prepare ^{23}Na , ^{40}K atoms or $^{23}\text{Na}^{40}\text{K}$ molecules in a certain hyperfine state.

2.9 Dipole Trap

After evaporation in the magnetic trap the atoms would be loaded into an optical dipole trap [127]. Most commonly those traps confine atoms in the focus of a laser beam which is far red detuned with respect to all relevant atomic transitions. Due to the strong detuning photon scattering becomes irrelevant. Additionally, optical dipole traps do not require magnetic fields, thus these can be used to manipulate the trapped atoms, e.g. when associating Feshbach molecules.

The confining potential of a dipole trap originates in the AC Stark shift, which an atom, or molecule, experiences in an oscillating electric field. It can be described by [128]:

$$\Delta = -\frac{1}{2\epsilon_0 c} I \Re(\alpha) . \quad (2.12)$$

Here, I is the intensity of the light field and α the AC polarizability. The vacuum permittivity and the speed of light are denoted ϵ_0 and c . The corresponding photon scattering rate is:

$$\frac{1}{\tau_{\text{ph}}} = \frac{1}{\hbar\epsilon_0 c} I \Im(\alpha) . \quad (2.13)$$

When the optical dipole trap is far red detuned to any atomic transition, saturation effects can be neglected and α can be described by the semi-classical model of a two level atom in a monochromatic radiation field. Accordingly, the potential shift and the scattering rate can be rewritten as [128]:

$$\Delta = -\frac{3\pi c^2}{2\omega_0^3} \left(\frac{\Gamma}{\omega_0 - \omega_L} + \frac{\Gamma}{\omega_0 + \omega_L} \right) I(\vec{r}) \quad \text{and} \quad (2.14)$$

$$\frac{1}{\tau_{\text{p}}} = \frac{3\pi c^2}{2\hbar\omega_0^3} \left(\frac{\omega_L}{\omega_0} \right)^3 \left(\frac{\Gamma}{\omega_0 - \omega_L} + \frac{\Gamma}{\omega_0 + \omega_L} \right)^2 I(\vec{r}) . \quad (2.15)$$

Here, Γ accounts for the finite linewidth of the atomic transition, ω_0 is the resonance frequency of the atomic transition and ω_L the frequency of the laser field.

In a light field which is red detuned ($\omega_L < \omega_0$) with respect to the atomic transition, the AC Stark shift described in Eq. (2.14) lowers the energy of the ground state. As the shift is linear in the intensity I , a red detuned laser beam creates a confining potential, centered at its focus. In this potential the atoms and molecules can be trapped¹⁴.

¹⁴ If the laser light was blue detuned ($\omega_L > \omega_0$) with respect to the atomic transition the ground state is shifted to higher energies and atoms are repelled from the focus. This effect can be used to plug the center of the quadrupole trap to prevent losses due to spin flips.

The scattering rate $\frac{1}{\tau_p}$ has the same dependence on the intensity as the AC Stark shift, but decreases with the inverse square of the detuning. Therefore, optical dipole traps which are operated far from atomic and molecular resonances barely exhibit photon scattering, preventing heating.

2.9.1 Implementation

In this experiment the far off-resonant optical dipole trap will be formed by two crossed laser beams at a wavelength of 1064 nm. Both beams are in the horizontal plane and their foci intersect perpendicularly at the center of the magnetic trap. The beam paths are shown in Fig. 2.3.

The spatially dependent AC Stark shift of the atoms and molecules in the optical dipole trap can be estimated by means of ??, assuming that the intensity of the $I(\vec{r})$ of the laser beams can be described by a Gaussian mode:

$$I(\vec{r}) = \frac{2P}{\pi w_x(y) w_z(y)} e^{-2\left(\frac{x^2}{w_x^2(y)} + \frac{z^2}{w_z^2(y)}\right)}. \quad (2.16)$$

Here, P is the central power of the beam and y is the propagation direction. In a perpendicularly crossed trap, the confinement along the axial direction of a beam is negligible compared to the confinement created by the other beam. The waists can be substituted by their values at the foci w_0 .

The characteristic parameters of an optical dipole trap are the depth of the potential U_{dip} and the trap frequencies ω_{dip} . For the experimentally determined waists (radii) $w_{z,0} = 40 \mu\text{m}$ and $w_{x,0} = w_{y,0} = 140 \mu\text{m}$ along the vertical and the horizontal directions and a light power of 1 W per beam, Eqs. (2.12), (2.14) and (2.16) result in the parameters listed in Table 2.3.

| | Na | K | NaK |
|----------------------------------------|------|------|-----|
| $U_{\text{dip,hor}} (\mu\text{K})$ | 3.3 | 11 | 18 |
| $U_{\text{dip,ver}} (\mu\text{K})$ | 6.6 | 22 | 37 |
| $\omega_{\text{dip,hor}} (\text{kHz})$ | 0.30 | 0.54 | 0.7 |
| $\omega_{\text{dip,ver}} (\text{kHz})$ | 1.5 | 2.7 | 3.5 |

Table 2.3: Trap depths and frequencies of crossed optical dipole trap. A crossed optical dipole trap at a wavelength of 1064 nm with two equivalent horizontal beams is assumed. The beam waists are 40 μm in the vertical and 140 μm in the horizontal directions. The trap depths U_{dip} and frequencies ω_{dip} are computed for atomic Na and K and the NaK molecules in their respective ground states. For NaK the ground state polarizability at 1064 nm was used: $\alpha_{1064} = 1.2 \cdot 10^{-38} \frac{\text{Cm}^2}{\text{V}}$. The indices 'hor' and 'ver' indicate the horizontal and vertical directions.

Table 2.3 shows that for the same parameters the confinement of molecules will be significantly stronger than the confinement of the individual atoms. For estimating the trap parameters of NaK ground state molecules, their AC polarizability $\alpha_{1064} = 1.2 \cdot$

$10^{-38} \frac{\text{Cm}^2}{\text{V}}$ at 1064 nm was used. In the case of sodium and potassium, ω_0 was set to the values of the respective D1 and D2 lines.

The light for the optical dipole trap is obtained from a 42 W Mephisto MOPA (InnoLight) and transmitted to the optical table via polarization maintaining, single mode optical fibers. The fibers limit the power of the dipole trap to about 2 W per beam. The geometry of the beams and their intensity stabilization are described in detail in [120].

2.9.2 Optical Lattice

To investigate lattice physics [7] a three-dimensional, cubic optical lattice can be implemented in this experiment. Optical lattices were also shown to enhance [67] the efficiency of the molecule creation by associating them from Mott insulators [129].

When the molecules are associated in a optical lattice the system is instantaneously stabilized against collisional losses [129, 67]. Also, the molecules are directly filled into that periodic potential which is the essential ingredient to most proposals listed in Chapter 1.

In the experiment, the two horizontal axes of the optical lattice align with the axes of the dipole trap, the third one with the vertical direction. Figure 2.3 shows the beam paths. The light for the optical lattice is provided by the same laser as the light for the dipole trap, therefore the lattice constant is $1064 \text{ nm}/2 = 532 \text{ nm}$. More details about the implementation of the optical lattice are again found in [120].

2.10 Imaging

The response of a system to changes in an external parameter can be determined by repeatedly altering this parameter and collecting the relevant information about the atomic sample after each change. Most of the relevant information, like the density or the momentum distribution, can be extracted from images of the sample.

Generally, ultracold atomic gases can be imaged in two different situations: in-situ and during time of flight. In-situ refers to measuring the density distribution of a sample in the trap, whereas for time of flight the sample is released from the trap and after some time of ballistic expansion the image is taken. The density distribution measured in time of flight can very well be mapped onto the momentum distribution of the sample in the trap. In both cases care has to be taken that the imaging itself does not destroy the desired informations about the atomic sample. The sample itself is usually destroyed, because it was heated by photon scattering, or flew away. In this cases a new sample has to be created: starting from cold atomic beams, the creation of a 3D-MOT, etc. – until a new image is taken, again.

In this experiment it is planned to image the atomic samples along the three main axes of the experiment, defined by the axes of the optical lattice. To enable this the 45° mirrors reflecting the 3D-MOT light into the chamber have to be flipped as indicated in Fig. 2.3. The horizontal axes provide optical access for numerical apertures of about 0.05, the vertical axis for numerical apertures of about 0.6, allowing for high resolution imaging as described in Chapter 4. The following paragraphs will give a short introduction

to imaging ultracold gases, determining their atom number and introducing a camera program.

2.10.1 Different Techniques

For actually taking images of atomic samples, several techniques [130], such as, absorption, dark ground [131], phase contrast [132], phase contrast polarization [133], diffraction [134], and fluoresce [135, 136] imaging are commonly used. Which of those techniques is applied depends on the specific requirements of the experiment. The most widely used technique in ultracold atomic gases is absorption imaging, whereas single-atom resolved imaging in a periodic potential with a small lattice constant was until now only achieved in fluorescence images [137, 138].

During fluorescence and absorption imaging, the atoms are illuminated with near resonant photons which they absorb and spontaneously re-emit. The difference is that fluorescence images are created by collecting the re-emitted photons, whereas absorption images show the ‘shadow’ of the ‘absorbing’ atoms in the illuminating beam. Consequently, the signal in fluorescence imaging is usually less efficient, as only a small fraction of the scattered photons can be collected by the numerical aperture of the system¹⁵. In absorption images all absorbed photons, except those few re-emitted in the forward direction are registered missing.

Both methods can be used to determine the atom number of atomic samples, which is relevant during the lifetime measurements discussed in Section 2.7: For absorption imaging the atomic cloud is illuminated by a resonant laser beam. The images show the transversal profile of this laser beam at the position of the atomic cloud. Let the image of the profile on the CCD of the camera be $I_0(x', y')$, when no atoms are present. When a cloud of atoms with number density $n(x, y, z)$ is present, it imprints a shadow on the imaging beam. In the case of a laser beam with a small intensity, i.e. neglecting saturation, the shadow cast by two level atoms [78] can be described by

$$I(x, y) = I_0(x, y) e^{-\int dz \sigma n(x, y, z)} + V. \quad (2.17)$$

The cross section $\sigma = \frac{3\lambda^2}{2\pi} \frac{1}{1+4\delta^2/\Gamma^2}$ considers a detuning δ of the imaging light from the atomic resonance, but no saturation. The imaging wavelength is denoted λ . In addition to the imaging laser beam, background light V not contributing to the image (e.g. at another wavelength) is registered. Neglecting forward scattering and saturation, the atom number is:

$$N = \frac{1}{\sigma} \int dx dy \ln \left(\frac{I_0 - V}{I - V} \right). \quad (2.18)$$

Note, that the evaluation has to account for the magnification M , and the atomic sample has to be dilute enough to permit the transmission of some residual light, also in the dense regions of the atomic cloud.

¹⁵ Common numerical apertures in cold atoms experiments are significantly smaller than 1. For a numerical aperture of 0.50 about 6.7% of the re-emitted photons enter the imaging system.

Fluorescence images only register a fraction of the absorbed photons, namely those which result in photons spontaneously emitted into the numerical aperture A of the imaging system. An approximation for the fraction of photons, valid for small A , is $A^2/4$. From the number of registered photons N_p the atom number can be estimated to be [78]

$$N = N_p \frac{4}{A^2} \frac{1 + s_0 + 4\delta^2/\Gamma^2}{\tau s_0 \Gamma/2} \frac{1}{\chi}. \quad (2.19)$$

Here, $s_0 = \frac{I}{I_S}$ is the saturation parameter, with I_S being the saturation intensity, and τ is the time for which the sample was illuminated. The factor χ considers the transmission of optical elements, etc. Equation (2.19) only holds for two level atoms and does not consider the intensity decrease of the illuminating beam over the sample, re-absorption or polarization.

Absorption, as well as fluorescence imaging heat the sample by photon scattering. After absorbing n_p photons an atom acquired a recoil of $n_p \cdot \hbar \vec{k}$, and an additional momentum $\sqrt{n_p} \cdot \hbar k$ in a random direction, due to the spontaneous re-emission. These additional momenta change the position and shape of the cloud and introduce Doppler shifts. From this point of view, it is favorable to reduce the amount of absorbed photons and the illumination time.

Regarding single-atom sensitivity, which will become relevant in Chapter 4, fluorescence imaging did prove to be superior [139, 136, 137, 138, 140] over absorption imaging, as long as sufficiently deep traps, or additional cooling can be provided¹⁶. Recently, single atom sensitivity was also shown for absorption imaging [140]. However, even in the same setup, it appears to be more challenging than fluorescence imaging, due to fluctuations of the background light.

Dispersive or diffractive imaging techniques can be advantageous when imaging dense clouds of ultracold molecules. As those techniques can work at a relatively large detuning of the imaging light, they can also be applied to open transitions [142].

2.10.2 PolarCam

In this experiment, images can be recorded using an Andor iXon3 889 or a pco.pixelfly usb. Whenever images of the atomic sample are taken during the experiment, the sequence is the following: For each experiment sequence the number of images to be taken, their exposure time, and the camera settings are defined. Then, the camera is started. At the desired instant, the experiment control triggers the camera via TTL and the picture is taken¹⁷. After the defined number of images was taken a computer, the 'camera computer', reads the images from the buffer and they can be processed. In absorption images, for example, the background picture (V) has to be subtracted from the originals, when the atom number is determined using Eq. (2.18).

To change the settings of the cameras, read the pictures from their buffers and to process them, requires a software which defines the interaction between the camera and

¹⁶ In [141], e.g. 1000 photons from a single atom are registered, requiring the absorption and re-emission of about 10000 photons.

¹⁷ Note, the delay of the camera when processing an external trigger can be $5.6 \mu\text{s}$, which is on the order of the $10 \mu\text{s}$ clock time of the experiment control.

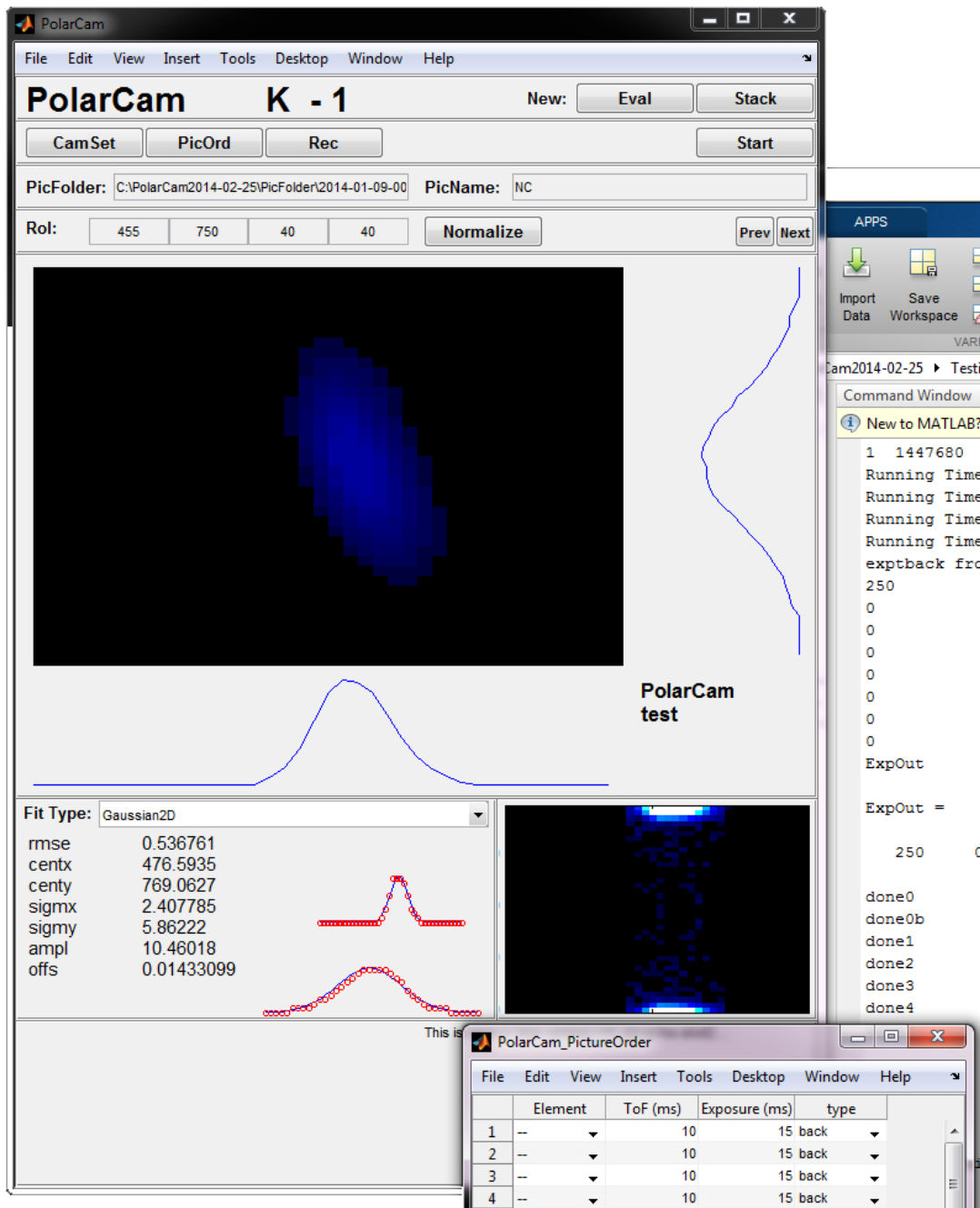


Figure 2.16: PolarCam main GUI. Main GUI of PolarCam after an image of a ^{39}K MOT was acquired. The image (after background subtraction) is shown in the central panel. Only the desired region of interest (ROI) is plotted. Below and to the right of the image cumulative cross sections are plotted. On the bottom left panel the results of a two-dimensional Gaussian fit to the selected ROI is shown. The fit parameters are given and the goodness of fit can be checked in the cross sections depicted. The panel on the lower right shows the FFT of the ROI. The 'PicOrd' table is shown in the bottom right corner.

the camera computer. The `pco.pixelfly usb` can be controlled via the PolarCam graphical user interface (GUI). The GUI is written in Matlab and interacts with the camera via a MEX-file to make use of the software development kit provided by pco. This user interface can presumably be extended to the Andor iXon if desired.

The general idea of PolarCam was to separate the process of picture taking and the experiment control as much as possible. As a consequence, no direct interaction between the camera computer and the experiment control, or the computer initializing the experiment control is necessary. Even though the latter would be possible and might provide substantial comfort.

Figure 2.16 shows a screen shot of the software during operation. In the upper panels of the GUI are several rows of buttons and text fields that can be used to define the sequence in which pictures are taken.

The two buttons in the most upper panel are reserved for post-evaluation, which is independent from the recoding of the images.

In the second panel of the GUI four buttons are found:

- ‘CamSet’ opens a sub window in which the settings of the camera, except the exposure time, could be changed. The `pixelfly.usb` does not provide any settings which require changes, thus the button ‘CamSet’ is not assigned.
- ‘PicOrd’ opens a table in which each row corresponds to an image taken during one cycle of the experiment. The four columns of the table allow certain definitions for every image:
 - The ‘Element’ (sodium, potassium, molecule) must be specified.
 - The time of flight ‘ToF’ can be specified.
 - The ‘Exposure’ time has to be specified.
 - The ‘Type’ of the picture (with atoms, without atoms, background) has to be specified.

For each different ‘Element’ specified a sub-GUI is opened which allows to evaluate each ‘Element’ independently.

- ‘Rec’ is a toggle button. When this button is pressed all images are saved under the path specified in ‘PicFolder’.
- ‘Start’ is also a toggle button. It defines the state of the camera. When this button is pressed the camera is rearmed after every cycle. Otherwise the camera is not active.

In the third row, the folder in which the images are stored (‘PicFolder’) can be defined. ‘PicName’ defines the name of the subfolder in which the images are stored. Each cycle is then numbered consecutively (*nnnn*) and the pictures taken during each cycle are labeled by ‘Element’, ‘Type’ and consecutive numbering. The images in this example are stored in a Folder ‘C:\PolarCam2014-02-25\PicFolder\2014-01-09-0003\NC \nnnn’, named, e.g., ‘K-with-1’ or ‘K-wout-1’.

The fourth row lists the region of interest (RoI) which is shown in the main axis. The main axis shows the latest image taken. In this case the RoI shows a 3D-MOT of ^{39}K . The graphs on the right and bottom show cumulated profiles of the RoI. In the panel

below various fits can be selected and if desired informations can be shown. Here a two-dimensional Gaussian is fitted to the RoI.

Taking the images is a cycle based process. Before beginning the measurement, the user specifies the sequence of images in 'PicOrd'. Each row in the table corresponds to one image taken during a cycle. Therefore, the number of rows has to correspond to the number of triggers given to the camera. After pressing 'Start' the camera will be armed and awaits triggers which are given by the experiment control. With each trigger one image is taken according to the specifications made in 'PicOrd'. When the number of triggers corresponds the number of entries in 'PicOrd' PolarCam assumes that the cycle is finished. It retrieves the images from the camera, saves the originals, subtracts background images and fits the specified functions to the RoI. At the same time the camera is re-armed to await the images of the next cycle.

The advantages of PolarCam are its modular structure and its ability to operate with any camera that is programmable in a language that is compatible with Matlab. More importantly, PolarCam can borrow any function from Matlab, for computations, fitting or plotting.

Derivations of PolarCam were used for the optimization of the high resolution imaging system discussed in Chapter 4 and for the evaluation of its performance.

2.11 Towards the Creation of Molecules

Before exploring dipolar interactions of ultracold, particles in the quantum regime, ^{23}Na and ^{40}K must be associated to heteronuclear, ground state molecules. To achieve this, pairs of ^{23}Na and ^{40}K atoms are first combined to heteronuclear Feshbach molecules [143, 89, 144] which are subsequently transferred to their electronic ground state via stimulated Raman adiabatic passage (STIRAP) [90, 25, 145].

There are two possible routes for creating of ground state molecules in this way: In the first approach the Feshbach molecules are created in the optical dipole trap and then transferred to their rovibrational ground state, using STIRAP [25, 146, 145]. This technique, however, is relatively inefficient in the creation of Feshbach molecules [147, 67] and the created molecules are constantly subject to collisions. The second route relies on a sophisticated loading of the atoms in a three-dimensional optical lattice, aiming for conditions in which all sites are filled with one atom of each species [92, 93, 148]. Due to the tighter confinement, the overlap of both species is significantly improved compared to the creation of Feshbach molecules in an optical dipole trap and the conversion efficiency could be 100% [67], while collisions are inherently prevented. In an experiment creating $^{40}\text{K}^{87}\text{Rb}$ molecules, the conversion efficiency to Feshbach molecules in the dipole trap was reported to be 25% [147]. When, in contrast, a site of an optical lattice was occupied with one ^{40}K and one ^{87}Rb atom, the conversion efficiency was 87(13)% [67, 149].

Nevertheless, the general procedure will be to assemble Feshbach molecules which are then transferred to the rovibrational ground state.

2.11.1 Feshbach Molecules

In a Fano-Feshbach [86, 87] resonance – as used in cold atomic gases [88, 150] – a system of two free atoms couples to a bound molecular state. This coupling can be used to change the scattering lengths in an atomic sample, or to convert pairs of atoms into molecules.

A description of channels and the idea of Feshbach resonances is given in [151]: Starting from a very general approach the system of two coupled channels, as shown in Fig. 2.17, is investigated. In the basis of the radial wave functions the coupled channel Hamiltonian can be written as

$$\hat{H} = \begin{pmatrix} H_{in} & V \\ V & H_{cl} \end{pmatrix}, \quad (2.20)$$

with $H_{in/cl}$ being the Hamiltonians of the incoming and closed channels. The coupling between both channels is described by V . For two atoms the coupling V is given by the dominant electric interaction V_{el} coupling and the relativistic spin-spin coupling V_{sp} [144]. Here $|\phi_{in}(r)\rangle$ and $|\phi_{cl}(r)\rangle$ are the solutions of the Schrödinger equation corresponding to \hat{H} . In the uncoupled case ($V = 0$) they go to $|\phi_{in,i}\rangle$ and $|\phi_{cl,0}\rangle$.

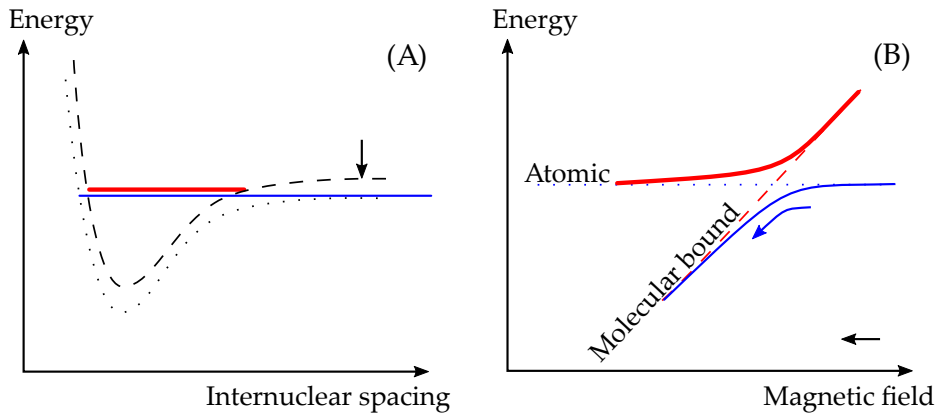


Figure 2.17: Two level model of a magnetic Feshbach resonance. (A): Potential energy curves shortly before the resonance. (B): The adiabatic energies of the two involved states as a function of the magnetic field.

The black arrows indicated how the association of Feshbach molecules evolves with time. At the beginning the thin blue line represents the incoming state of unbound atoms, the red line a bound state in the closed channel. As the magnetic field is ramped to lower values over time both states would shift through another if they were not coupled by V . Due to the coupling however the incoming state makes the transition to the molecular bound state, indicated in (B) by the blue bent arrow. Note that depending on the states involved the magnetic field dependence can be different.

A Feshbach resonance is magnetically tunable when $|\phi_{in}\rangle$ and $|\phi_{cl}\rangle$ have a different magnetic moment. This difference in the magnetic moment $\Delta\mu$ can be used to shift the potential energy curves of $|\phi_{in}\rangle$ and $|\phi_{cl}\rangle$ with respect to each other. As indicated in Fig. 2.17 this shift can be fully attributed to $H_{cl} = H_{cl}(B)$.

The position B_0 and width ΔB of the resonance can be used to describe the divergence of the s-wave scattering length

$$a_s = a_{\text{bg}} \left(1 + \frac{\Delta B}{B - B_0} \right), \quad (2.21)$$

in the vicinity of a magnetic Feshbach resonance [152, 153]. Here, a_{bg} denotes the background scattering length. The tunability of the scattering length makes Feshbach resonances extremely valuable for experiments with ultracold atomic gases.

Important for the creation of Feshbach molecules, from unbound atoms, is that the coupling V leads to an avoided crossing of the atomic and molecular states which is shown in Fig. 2.17 (B). When ramping the molecular state to lower energies, crossing the energy of the uncoupled, atomic state, two unbound atoms can form a molecular bound state [154, 155, 156] [4, 157].

Shortly after first influences of the magnetic field on interactions between different atomic species were observed [158], the first Feshbach resonances between two species of atoms were measured [159] and heteronuclear Feshbach molecules were created [143]. Those heteronuclear Feshbach molecules of ^{40}K and ^{87}Rb were produced in an optical lattice. This technique is also feasible for other species like ^{87}Rb and ^{133}Cs [129] and, as mentioned above, results in higher transfer efficiencies, compared to the association in an optical dipole trap.

For ^{23}Na and ^{40}K a 29(2) G wide Feshbach resonance at $139.7_{-1.4}^{+2.1}$ G was used to create an ensemble of ultracold Feshbach molecules [89]. In this case the molecules were, created via radio frequency association in an optical dipole trap. The background scattering length was determined to be $-690_{-130}^{+90} a_0$ and the difference in the magnetic moment of the bound molecular state to the unbound atomic state was found to be $\Delta\mu = 2.4\mu_B$. Here a_0 and μ_B are the Bohr radius and magneton. The entrance channel of this Feshbach resonance with sodium in the $|F = 1, m_F = 1\rangle_{\text{Na}}$ and potassium in $|F = 9/2, m_F = -5/2\rangle_{\text{K}}$ hyperfine ground state is predominantly of triplet character, so is the closed channel [95].

In our experiment the magnetic field for the creation of Feshbach molecules will be created by the coils introduced in Section 2.5. The determined field of 139.7 G can be reached by applying a current of about 41 A.

2.11.2 Ground State Transfer

Loosely bound Feshbach molecules can be transferred to their absolute rovibrational ground state using STIRAP [90, 25]. This coherent technique transfers the molecules exclusively to the selected internal state, introduces only a negligible amount of heat into the ultracold system, bridges the gap between the triplet Feshbach and the singlet ground state, and can be very effective [25]. STIRAP was intensely treated theoretically [90] and to determine the requirements for the ground state transfer the most relevant results are summarized here.

According to the model [90] illustrated in Fig. 2.18, STIRAP transfers a system from an initial state $|1\rangle$ to a final state $|3\rangle$ by coupling to an intermediate state $|2\rangle$, which is never populated during the transfer. This avoids a decrease in the transfer efficiency due to a potentially lossy intermediate state $|2\rangle$. The coupling of $|1\rangle$ and $|3\rangle$ to the

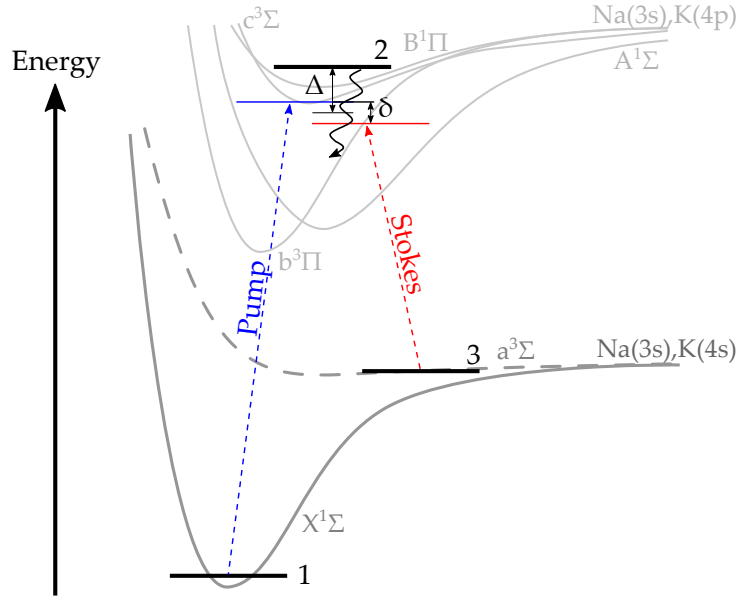


Figure 2.18: Lambda scheme of STIRAP transfer. A system is coherently transferred from an initial state $|1\rangle$ to a final state $|3\rangle$, using the coupling to an intermediate state $|2\rangle$, which is never populated during this process. The potential energy curves of the molecular states are indicated by the gray lines. The frequency Δ indicates the common detuning of the pump and Stokes laser with respect to $|2\rangle$ and δ the frequency mismatch between them.

intermediate state $|2\rangle$ is initiated by a pump and a Stokes laser. The common detuning of both lasers with respect to state $|2\rangle$ is denoted Δ , their relative detuning δ . The transfer is determined by the ratio of the Rabi frequencies Ω_S and Ω_P that are induced by the Stokes and the pump laser. To achieve a transfer without populating $|2\rangle$ the Stokes laser precedes the pump laser which enables an efficient transfer even when the intermediate state $|2\rangle$ has a non zero decay rate γ .

The process is considered to be locally (in time) adiabatic [160] when

$$\left| \frac{\dot{\Omega}_P \Omega_S - \Omega_P \dot{\Omega}_S}{\Omega_P^2 + \Omega_S^2} \right| \ll |\omega^\pm - \omega^0|. \quad (2.22)$$

A global criterion [90] for adiabaticity can be expressed in terms of the root mean square Rabi frequency $\Omega_{\text{rms}}(t) = \sqrt{\Omega_P^2 + \Omega_S^2}$ when all pulses can be considered smooth. This global criterion requires

$$\Omega_{\text{rms}} \tau' > 10, \quad (2.23)$$

where τ' is the separation of the pump and the Stokes pulse. Even under these ideal conditions the fraction of population transfer decays exponentially

$$P^0 = e^{-\frac{\gamma}{\Omega_{\text{rms}}} \left(\frac{\pi^2}{\tau} + \frac{\delta^2 \tau}{2} \right)}, \quad (2.24)$$

in γ and δ^2 [161]. Equation (2.24) shows that losses due to γ can be minimized by large pulse areas $\Omega_{\text{rms}}\tau$, where τ denotes the length of the pump and the Stokes pulses. In turn, large pulse lengths τ require a small δ , i.e. a minimal relative detuning of the pump and the Stokes laser.

The presence of laser frequency noise in the STIRAP laser system was simulated in [161]. The results give valuable insight on the properties a STIRAP system should have: They show that correlated frequency noise is not really problematic for the transfer efficiency, as it can be considered as a continuous change of the common detuning Δ . Severe are the influence of partially or fully uncorrelated noise. In the former case the transfer efficiency oscillates with the pulse area, while fully uncorrelated frequency noise is fundamentally limiting. It was found that in the presence of fully uncorrelated noise the transfer efficiency is maximized when the laser frequency is strongly pulled towards the desired value in every time step. In this case the noise in the model becomes white [161]. To consider this noise the expression for the transfer efficiency can be extended to $P = P^0 P^n$, with

$$P^n = e^{-\frac{D\tau}{2}}. \quad (2.25)$$

The transfer is hence fundamentally limited by D which describes the bandwidth of the white noise [161]. To achieve $P^n > 0.9$ at a pulse duration of $10 \mu\text{s}$ the uncorrelated laser linewidth should be smaller than $2\pi \cdot 3 \text{ kHz}$.

The model used [161] assumed cos-pulse shapes separated by one pulse width τ and it was emphasized that the results are good for large pulse areas $\Omega_{\text{rms}}\tau \gg 1$.

The applicability of STIRAP to the creation of heteronuclear, ultra cold ground state molecules was already shown for $^{40}\text{K}^{87}\text{Rb}$ [25], $^{87}\text{Rb}^{133}\text{Cs}$ [146], and recently also for $^{23}\text{Na}^{40}\text{K}$ [145]. In the latter experiment the Feshbach resonance goes from a channel with sodium and potassium in the $|F = 1, m_F = 1\rangle_{\text{Na}}$ and $|F = 9/2, m_F = -9/2\rangle_{\text{K}}$ states to the molecular triplet state $|a^3\Sigma^+ \nu = 19, J = 1, F = 9/2, m_F = -7/2\rangle$ via radio frequency association. STIRAP, utilizing the mixed ($|c^3\Sigma^+ \nu = 35, J = 1\rangle$, $|B^1\Pi \nu = 12, J = 1\rangle$) intermediate state, transfers the molecules to the $|X^1\Sigma^+ \nu = 0, J = 0\rangle$ ground state. The momentum transfer during this STIRAP should correspond to about 30 nK. The efficiencies of Feshbach association and STIRAP transfer were reported to be 10% [91] and 75% [145], resulting in $5 \cdot 10^3$ ground state molecules [145]. Experiments with $^{40}\text{K}^{87}\text{Rb}$ achieved about $3 \cdot 10^4$ molecules with a STIRAP efficiency of 83%, and brought unity transfer probability into play [25].

Ground state molecule formation was also proposed and shown to work without the Feshbach association of molecules before the STIRAP [92, 162, 163].

In this experiment it is planned to bridge the gap between the Feshbach molecules and the molecular ground state via an intermediate state originating from the mixing of the $B^1\Pi$ and $c^3\Sigma$ potential energy curves [95, 164]. For the STIRAP two lasers, at 816 nm and 573 nm, respectively, locked to a high finesse cavity, are set up [100, 165]. Aiming for a relative linewidth of 1 kHz, the current cavity was designed to have a free spectral range of 2.0 GHz at a linewidth of 127 kHz [166].

Presuming the successful creation of ultracold polar molecules, the next chapter will show how those can be polarized.

CHAPTER 3

Electric Fields

Chapter 1 highlighted heteronuclear, ground state alkali dimers as excellent candidates to investigate dipolar interactions in quantum-many-body systems. The main argument for dialkalis was their large internal, electric dipole moment d' . Another point is the tunability of the molecules' electric dipole moment in the lab frame. Its magnitude and direction can be adjusted by external, electric fields. Therefore, the same system can be investigated with differently strong and attractive or repulsive dipolar interactions.

In the rest frame of the NaK ground state molecule, the internal dipole moment arises from the two electronically different atoms on the internuclear axis. A fact captured by the concept of electronegativity [167]. For a NaK molecule, it predicts a slight shift of the electron distribution towards the sodium atom¹. The shift results in an electric dipole moment in the molecule's rest frame. The actual computation of this internal dipole moment or determining it experimentally is far more involved and slightly varying results were reported: $d' = 2.76$ D, $d' = 2.56$ D, $d' = 2.72(6)$ D, $d' = 2.76$ D [19, 168, 169, 170].

In contrast, the Hamiltonian of a molecule in the unperturbed lab frame has inversion symmetry, and its eigenstates are also eigenstates of the parity operator. Therefore, the molecules do not have a dipole moment. Compared to the molecule's rest frame where inversion symmetry is broken by the two different atoms there is no such axis in the lab frame. In this situation the ground state molecule can be very well approximated by a rigid rotor with rotational constant B :

$$H_{ij}^0 \sim B \cdot [N_i(N_i + 1)] \delta_{ij}. \quad (3.1)$$

A detailed treatment is, e.g., found in [171]. Here, the Kronecker delta is denoted δ_{ij} . The eigenstates of the rotor Hamiltonian, the spherical harmonics $|N, m_N\rangle_i$, are specified by the quantum number N and its projection m_N , which are summarized in the collective indices i and j . Naturally, the spherical harmonics are parity eigenstates and do not show a dipole moment.

When applying an electric DC field $\vec{\mathcal{E}}$ to a polar molecule, the coupling of the molecule's internal dipole moment \vec{d}' to this field breaks the inversion symmetry of H_{ij}^0 and mixes states of different parity. The new eigenstates have a finite dipole moment and are obtained by diagonalizing

$$H_{ij} \sim B \cdot [N_i(N_i + 1)] \delta_{ij} - {}_i\langle N, m_N | \vec{\mathcal{E}} \cdot \vec{d}' | N, m_N \rangle_j. \quad (3.2)$$

This chapter will discuss which features of an electric DC field are desirable when polarizing molecules and how these features can be implemented in an electrode geometry, which creates the fields.

After quantifying the polarization as a function of the applied electric field, the effect of the Stark shift on the confinement of molecules in optical dipole traps will be investigated. In this context it was found that already small spatial variations of the electric field magnitude can lead to a deconfinement of the molecules. Therefore devising an electrode configuration which creates extremely uniform electric fields is essential. The other requirements on the electrode geometry stem from experimental requirements.

In summary, the electrode geometry should enable an electric field up to $10 \frac{\text{kV}}{\text{cm}}$, corresponding to a polarization of 68% (1.9 D) in the case of NaK. The direction of the field

¹ The electronegativities of sodium and potassium are: Na: 0.93; K: 0.82.

should be continuously rotatable in a vertical two-dimensional plane, to tune the alignment of the dipoles. Relative spatial deviations in the magnitude of the field should be suppressed to avoid a deconfinement. An exception to the latter are intentionally created field gradients, which can be used for addressing rotational states of molecules in single layers of a one dimensional optical lattice. Those requirements are in detail summarized at the beginning of Section 3.3.

In Section 3.3 an electrode geometry, enabling all these requirements, will be devised. The design of the electrode geometry was refined by simulations with COMSOL Multiphysics.

The content of this chapter is going to be published elsewhere [172]. The following text is to some extent identical to this publication.

3.1 Molecules in Electric Fields

The effects of external electric DC fields on polar ground state molecules are described by Eq. (3.2). It can be rewritten in dimensionless quantities:

$$H_{i,j} \sim [N_i(N_i + 1)] \delta_{ij} - E \cdot \langle N, m_N | \cos \theta | N, m_N \rangle_j . \quad (3.3)$$

In this dimensionless representation, energies are given in units of B , and electric fields E are in units of the characteristic electric field $\mathcal{E}_c = B/d'$. Hence, the coupling between rotational states is directly indicated by E . For the $^{23}\text{Na}^{40}\text{K}$ ground state, the internal dipole moment $d' = 2.76 \text{ D}$ [170] and the rotational constant $B = 2.83 \text{ GHz} \times h = 0.136 \text{ K} \times k_B$ [170] result in a characteristic electric field $\mathcal{E}_{c,\text{NaK}} = 2.04 \frac{\text{kV}}{\text{cm}}$. Here, h and k_B are the Planck and Boltzmann constants. The values for other heteronuclear alkali dimers are shown in Fig. 1.2.

After diagonalizing Eq. (3.3), the ground state energy of the rotor model is:

$$U_A = \langle A | H_{\text{diag}} | A \rangle , \quad (3.4)$$

with $|A\rangle$ being the new ground state, which corresponds to the rotational state $|0,0\rangle$ when $E \rightarrow 0$. In the cases of $E \ll 1$ and $E \gg 1$ the ground state energy is quadratic and linear in E , respectively, resembling the quadratic and linear Stark shift.

Implicitly Eq. (3.3) assumes that electric field changes are slow, i.e. adiabatic, compared to the scale given by B . As the ground state $|A\rangle$ is coupled to higher states, fluctuations δE in the electric field create a finite probability for transferring molecules from the ground state to one of the excited states. Considering the coupling of $|A\rangle$ to the next state, the fluctuations of the electric field have to be smaller than the timescale given by the rotational constant [173]:

$$\frac{\partial E}{\partial t} \ll 12 \frac{B}{h} . \quad (3.5)$$

For NaK, $\frac{B}{h}$ is on the order of $100 \frac{\text{kV}}{\text{cm}} \text{ GHz}$, or $10 \frac{\text{kV}}{\text{cm}}$ per 0.1 ns – a ramping speed far from being experimentally relevant. Applying the corresponding formula from [174] to different electric field ramps, as well as numerically solving the Schrödinger equation, support Eq. (3.5).

Equation (3.2) indicates that the direction of the applied electric field determines the direction of the induced dipole moment in the ground state $|A\rangle$. The magnitude of the induced dipole moment is obtained by taking the first derivative of $U_A(E)$ with respect to E :

$$\gamma = -\frac{\partial U_A}{\partial E}. \quad (3.6)$$

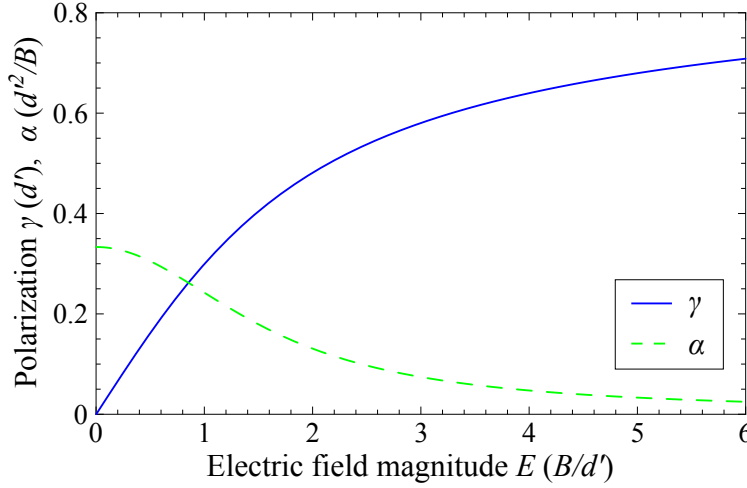


Figure 3.1: Solid line: Polarization γ of the dipole moment in space-fixed frame. The dashed line: α , is the second derivative of U_A with respect to E , i.e. the first derivative of γ .

Figure 3.1 plots the polarization γ as a function of E . The polarization γ is a relative quantity in units of d' . It rises linearly for $E \ll 1$, the region of the quadratic Stark shift, and saturates for $E \rightarrow \infty$, where the Stark shift is linear. In the intermediate region the coupling of $|0,0\rangle$ to higher rotational states provides a smooth transition between both regimes. At $E = 5.0 B/d$ a polarization of $\gamma = 0.68$ is reached. For NaK ground state molecules this corresponds to 1.9 D at 10 kV/cm.

As the direction and magnitude of the induced dipole moment depend on the direction and magnitude of the applied electric field, the latter must be easily tunable to change the characteristics of the dipolar interaction during the experiment.

Due to the Stark shift in $U_A(E)$, the spatial potential of a ground state molecule is affected by small variations δE from the uniform field E_0 , $E_0 \gg \delta E$. This can have an effect on the confinement of the molecules in a optical dipole trap. This is investigated in the following. Figure 3.2 shows how small deviations δE alter U_A . By expanding $U_A(E)$ in δE different corrections can be quantified.

$$U_A(E_0 + \delta E) \approx U_A|_{E_0} - \gamma|_{E_0} \delta E - \frac{1}{2} \alpha|_{E_0} \delta E^2 + \mathcal{O}(\delta E^3). \quad (3.7)$$

For $E \rightarrow 0$ deviations δE barely have an impact, because the first order correction to U_A , the polarization γ , vanishes. In this case the dominant non-zero correction is of second order, described by $\alpha = -\frac{\partial^2 U_A}{\partial E^2}$.

For $E \rightarrow \infty$, γ saturates, higher order corrections go to zero, and U_A becomes linear in δE . In the intermediate regime corrections of higher orders could be significant, these

were however evaluated to be small². Therefore, U_A can be truncated after the first order in δE , when $E \rightarrow \infty$:

$$U_A(E_0 + \delta E) \approx U_A|_{E_0} - \gamma|_{E_0} \delta E + \mathcal{O}(\delta E^2). \quad (3.8)$$

As the experiment aims for highly polarized molecules, and the impact of deviations δE on U_A is most severe and linear at large electric fields, Eq. (3.8) is a good choice for the following estimates.

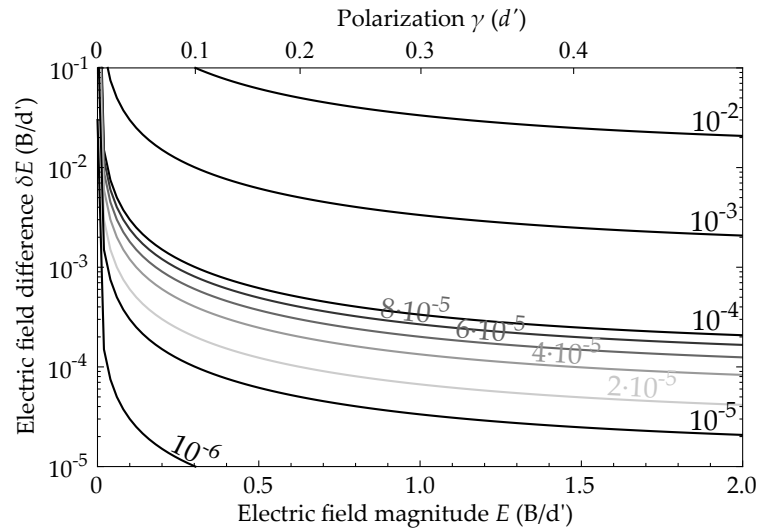


Figure 3.2: Contours of Stark shift due to perturbation. Stark shift of a polarized molecule due to a variation δE in the electric field. The contours are in units of B . The lower x-axis shows the applied electric field E_0 , the upper x-axis the corresponding polarization γ of a molecule. The y-axis denotes the change δE of the electric field.

3.2 The Effect of Electric Fields on Trapped Molecules

In the experiment the molecules are confined in an optical dipole trap and are polarized by means of external electrodes. Figure 3.3, in which the induced dipoles are illustrated as black arrows, sketches this configuration: The overall confinement of the NaK molecules is provided by a red detuned, far off-resonant, horizontally crossed optical dipole trap, indicated by two red beams along the x and y direction. A vertical one-dimensional optical lattice can be added in which the molecules are confined in quasi two-dimensional layers. Further lattice beams along the directions of the dipole trap can imprint a full three-dimensional optical lattice (not depicted). The electrodes, sources of the electric field, are depicted as gray rods, extending in the y direction. The signs of their potentials are indicated by '+' and '-'. In the depicted configuration the electric field leads to a vertical orientation of the induced dipoles. Spatial variations of the electric field magnitude lead to a spatially dependent Stark shift that can overcome the confinement of the

² For $\delta E < 0.01 E_0$, the corrections to U_A , higher than first [second] order, are smaller than $1 \cdot 10^{-4}$ [$2 \cdot 10^{-7}$].

molecules in the optical dipole trap. Deriving the upper limit for the spatial variations, at which a confinement can still be maintained, is the topic of this section.

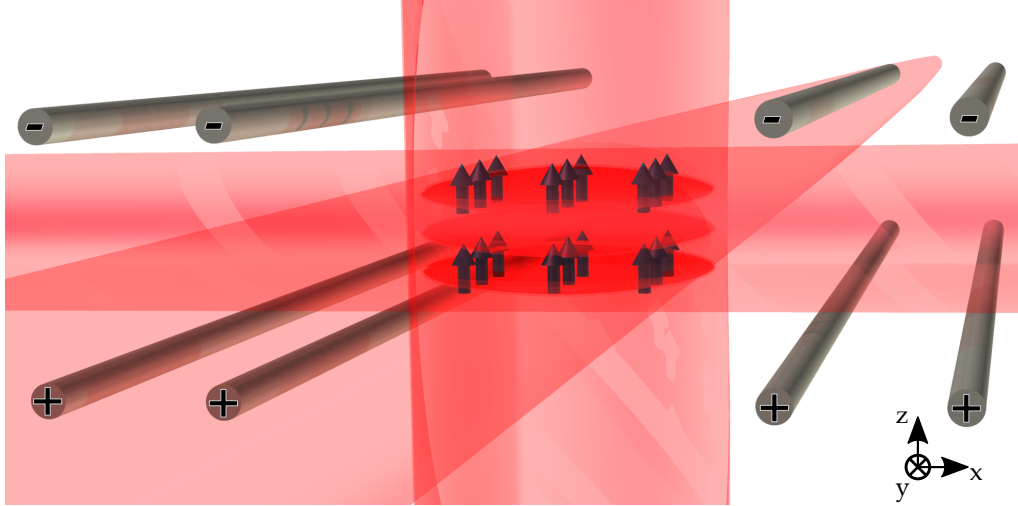


Figure 3.3: Polarized molecules in vertical optical lattice. Scheme of molecules confined by a horizontal, crossed dipole trap and one-dimensional optical lattice in the vertical direction. The beams of the dipole trap are in the horizontal x - y plane, the optical dipole trap beam aligns with the vertical z direction. The gray rods indicate electrodes extending in the y direction. They create a vertical electric field in the x - z plane. Indicated by arrows, the field polarizes the molecules along the same direction.

When being exposed to an applied electric field, a trapped polar molecule experiences a combination of the dipole trap's confining potential and the Stark shift, due to E :

$$U_{\text{tot}} = U_{\text{dip}} + U_{\text{A}}(E) . \quad (3.9)$$

For simplicity the following considerations are limited to the horizontal coordinate x . The treatment in the other two directions is analogous. The confinement, provided by the dipole trap, can be parametrized as a Gaussian profile:

$$U_{\text{dip}} = -U_{\text{dip},0} e^{-2(x/w_0)^2} = -U_{\text{dip},0} e^{-2\tilde{x}^2} , \quad (3.10)$$

with a trap depth $U_{\text{dip},0}$, in units of B , and the spatial dimension $\tilde{x} = \frac{x}{w_0}$, normalized to the dipole trap waist w_0 . For a molecule in the rovibrational ground state the potential created by the electric field, given in Eq. (3.8)

$$U_{\text{A}}(E(\tilde{x})) = U_{\text{A}}|_{E_0} - \gamma|_{E_0} \delta E(\tilde{x}) + \mathcal{O}(\delta E^2) ,$$

can perturb the confinement provided by the dipole trap. As this can result in a deconfinement of the molecules, a spatially uniform electric field is desired.

3.2.1 Different Contributions of the Electric Field

The influence of the electric field on the trapping of the molecules is highlighted when expanding E in a Taylor series of \tilde{x} . This approach is especially suitable when the characteristic length scale l of the electrode geometry is much larger than w_0 , because terms

of the order \tilde{x}^n scale with $(\frac{w_0}{l})^n$. In this setup $l = 10$ mm and $w_0 = 0.1$ mm, hence higher order term are naturally suppressed and gradients and curvatures dominate the spatial variation of the electric field magnitude.

Comparing the Taylor series with the potential of the optical dipole trap, will leads to upper limits for the gradient and the curvature of the electric field. Assuming that the centers of the dipole trap and the electrode geometry coincide, which is for now convenient, the series is given by

$$E(\tilde{x}) = E_0 + E_1\tilde{x} + E_2\tilde{x}^2 + \mathcal{O}(\tilde{x}^3). \quad (3.11)$$

By using \tilde{x} , the gradient E_1 and curvature E_2 correspond to the absolute field change³ over the length scale of the dipole trap and can be directly compared to the spatially uniform term E_0 .

Combining Eqs. (3.8), (3.10) and (3.11) the total potential is given by

$$U_{\text{tot}} \approx -U_{\text{dip},0}e^{-2\tilde{x}^2} + U_A|_{E_0} - \gamma|_{E_0} [E_1\tilde{x} + E_2\tilde{x}^2] + \mathcal{O}\left([E_1\tilde{x} + E_2\tilde{x}^2]^2\right). \quad (3.12)$$

The Taylor series of U_A , is valid for large electric fields E_0 and small deviations $E_1\tilde{x}, E_2\tilde{x}^2 \ll E_0$, with $|\tilde{x}| \leq 1$. The limits derived in the following sections will show how these assumptions and the results derived are consistent.

As summarized in Fig. 3.4 the gradient term E_1 tilts the overall potential U_{tot} along a certain direction. Such a tilt reduces the trap depth, indicated by the black arrow. The quadratic term E_2 reduces the trap depth, as well as the trap frequency in at least one spatial direction [112], flattening the trap.

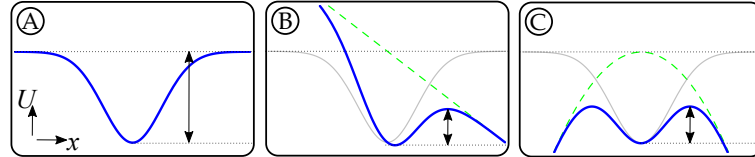


Figure 3.4: Deformation of trap potential. The blue line indicating the overall potential U_{tot} along the x axis is deformed due to different electric fields contributions. (A) shows the cross section of an unperturbed optical dipole trap potential U_{dip} . (B) visualizes the effect of an additional potential gradient along the x direction, (C) of a curved potential. The additional potentials are indicated as green, dashed lines. The arrows indicate the trap depth of the resulting potential.

The values of E_1 and E_2 at which the variation of the electric field overcomes the confining potential of an optical dipole trap are derived now. The effect of an electric field gradient can be determined when neglecting E_2 in Eq. (3.12):

$$U_{\text{tot}} \approx -U_{\text{dip},0}e^{-2\tilde{x}^2} - \gamma|_{E_0} [E_1\tilde{x}]. \quad (3.13)$$

³ To obtain the actual gradient and curvature E_1 and E_2 must be divided by w_0 and w_0^2 , respectively.

The minimum of such a potential, shown in Fig. 3.4 (B), exists only for an electric field gradient E_1 smaller than⁴:

$$E_{1,\text{lim}} = \frac{2}{\sqrt{e}} \frac{U_{\text{dip},0}}{\gamma|_{E_0}}. \quad (3.14)$$

When reducing Eq. (3.12) to E_2 instead of E_1 :

$$U_{\text{tot}} \approx -U_{\text{dip},0} e^{-2\tilde{x}^2} - \gamma|_{E_0} [E_2 \tilde{x}^2], \quad (3.15)$$

as illustrated in Fig. 3.4 (C), the corresponding limit for curvature can be derived. It was found that trapping is only possible for curvatures smaller than

$$E_{2,\text{lim}} = \frac{2U_{\text{dip},0}}{\gamma|_{E_0}}. \quad (3.16)$$

Table 3.1 compares $E_{1,\text{lim}}$ and $E_{2,\text{lim}}$ which depend nearly equally on $U_{\text{dip},0}$ and γ . Two exemplary values are shown in the last column.

| Coefficient | Limit | NaK _{68%} |
|--------------------|------------------------------------------------------|-----------------------------------------------------------------|
| $E_{1,\text{lim}}$ | $\frac{2}{\sqrt{e}} \frac{U_{\text{dip},0}}{\gamma}$ | $2.7 \cdot 10^{-4} \frac{\text{kV}}{\text{cm}} \frac{1}{w_0}$ |
| $E_{2,\text{lim}}$ | $2 \frac{U_{\text{dip},0}}{\gamma}$ | $4.5 \cdot 10^{-4} \frac{\text{kV}}{\text{cm}} \frac{1}{w_0^2}$ |

Table 3.1: Limits on electric field gradient and curvature. For electric field gradients and curvatures above the given values trapping cannot be maintained. The second column lists the limiting values, as the absolute field change over w_0 in dimensionless quantities. The last column shows exemplary values for NaK molecules polarized to 68% and confined in an optical dipole trap, like described in the text.

The exemplary values given in the last column are computed considering an optical dipole trap at a wavelength of $\lambda = 1064 \text{ nm}$. At this wavelength the ground state AC polarizability of NaK is $\alpha_{AC} = 1.2 \cdot 10^{-38} \frac{\text{Cm}^2}{\text{V}}$. The beam waist and the light power were assumed to be $w_0 = 100 \mu\text{m}$ and $P = 1 \text{ W}$, resulting in a trap depth⁵ of $U_{\text{dip},0} \times B = 10 \mu\text{K} \times k_B = 0.21 \text{ MHz} \times h$. Dividing $10 \mu\text{K} \times k_B$ by the rotational constant of NaK converts the trap depth to the dimensionless representation $U_{\text{dip},0,\text{NaK}} = 7.4 \cdot 10^{-5}$. For comparison: Over the distance w_0 , the change in the potential due to gravity is $7.4 \mu\text{K} \times k_B$.

Aiming for a polarization of 68%, both limits on the spatial variations of the electric field are more than four orders of magnitude lower than the $10 \frac{\text{kV}}{\text{cm}}$ needed to polarize

⁴ This limiting value disregards losses due to tunneling across the barrier on the open side of the tilted potential, which is indicated by the black arrow, in Fig. 3.4. However, those tunneling events become only relevant for $E_1 \approx E_{1,\text{lim}}$ and can therefore be neglected for the derivation of $E_{1,\text{lim}}$.

⁵ $U_{\text{dip},0} \times B = \frac{\alpha_{AC}}{\pi \epsilon_0 c} \frac{P}{w_0^2}$. Here, ϵ_0 is the vacuum permittivity and c the speed of light.

NaK. This justifies the assumption of $E_1\tilde{x}, E_2\tilde{x}^2 \ll E_0$ for $|\tilde{x}| \leq 1$, while indicating how crucial an elaborate electrode design is going to be.

The formulas in Table 3.1 also reveal that deconfinement can be overcome by a deeper dipole trap. This is either achieved by a higher light power P or a tighter waist w_0 . The waist of the trap is however usually determined by other experimental requirements related to the evaporative cooling and the molecule association.

Another way to enhance the confinement is to support the dipole trap by an optical lattice. Using the same beam parameters the small lattice constant creates a significantly tighter confinement than the waist of the dipole trap and losses can be strongly suppressed. Still, the tilt of the lattice can lead to a modified tunneling behavior between lattice sites [175].

Until now it was assumed that the symmetry center of the electric field coincides with the center of the dipole trap. In a system with electric field curvature it is also necessary to consider an offset \tilde{x}_0 between the center of the electric field and the center of the dipole trap:

$$U_{\text{tot}} \approx -U_{\text{dip},0}e^{-2\tilde{x}^2} + \gamma|_{E_0} [E_{2,x_0}(\tilde{x} - \tilde{x}_0)^2] \quad (3.17)$$

In the case of $\tilde{x}_0 \rightarrow \infty$ or $\tilde{x}_0 \rightarrow 0$ the respective limits for gradient or curvature are obtained. The turnover from a curvature to a gradient dominated behavior happens when \tilde{x}_0 becomes larger than $2\sqrt{e}$. It is possible to give an exact analytical limit on E_{2,x_0} :

$$E_{2,x_0,\text{lim}} = \frac{2U_{\text{dip},0}}{\gamma|_{E_0}} \left(1 - \frac{\eta^2}{9}\right) e^{-\frac{1}{18}\eta^2}, \quad (3.18)$$

with⁶ $\eta = \zeta + \frac{4\tilde{x}_0^2}{\zeta} - 2\tilde{x}_0$ and $\zeta = \sqrt[3]{-8\tilde{x}_0^3 + 3\sqrt{81\tilde{x}_0^2 - 48\tilde{x}_0^4} + 27\tilde{x}_0}$. A simple approximation for the limit of curvature is:

$$E_{2,x_0} \ll \frac{U_{\text{dip},0}}{\gamma|_{E_0}} \frac{1}{\sqrt{e} \cdot \tilde{x}_0 + 0.5}. \quad (3.19)$$

It deviates by at most 20% and gives the correct results for $\tilde{x}_0 \rightarrow \infty$ and $\tilde{x}_0 \rightarrow 0$.

3.2.2 Addressing Single Layers Using Electric Field Gradients

Intentionally nonuniform electric fields can be desirable for the experiment. An electric field gradient can provide the basis for manipulating the rotational states of molecules in a single layer of a one-dimensional lattice, while preserving the original state of the molecules in neighboring layers: Due to the gradient, the Stark shift of the rotational states will be different in every layer, making the transition energies between rotational states different, too. By applying a microwave of a certain frequency, it is hence possible to drive the transition in only a single layer selectively. In other layers the transition

⁶ Note that for $81 - 48\tilde{x}_0^2 < 0$, $\zeta = \sqrt[3]{2^3\tilde{x}_0^3 \times e^{i\phi}}$, and accordingly $\eta = 2\tilde{x}_0e^{i\phi} + \frac{2\tilde{x}_0}{e^{i\phi}} - 2\tilde{x}_0 = 2\tilde{x}_0(e^{i\phi} + e^{-i\phi})$, hence $E_{2,x_0,\text{lim}}$ is still real.

is detuned. This is useful for preparing molecules in single layers independently, e.g. when implementing theoretical proposals [37]. Above it was noted that deconfinement resulting from an electric field gradient will be less problematic, when the latter aligns with the axis of the optical lattice, which is the case in the considered configuration.

A microwave pulse, however, has a finite bandwidth. Hence, a transition is only restricted to a single layer, when its energy is detuned by more than this bandwidth in the neighboring layers. To obtain a 20 kHz splitting between two layers, which are spaced by 532 nm, an applied electric field gradient of $0.97 \left(\frac{\mathcal{E}_c}{w_0}\right)$ is required, when considering the transition from the ground state $|A\rangle$ to the state $|B\rangle$, which corresponds to the rotational level $|1,0\rangle$ for $E \rightarrow 0$. In the case of NaK molecules, this corresponds to $2.0 \cdot 10^2 \frac{\text{kV}}{\text{cm}^2}$, which is unlikely to be achieved experimentally.

These high gradients can be eluded by applying a uniform electric background field E_0 . At sufficiently high background fields, the molecules enter the regime of the linear Stark shift and larger splittings are achieved with smaller gradients. Figure 3.5 shows how the difference in the transition energy σ , between $|A\rangle$ and $|B\rangle$, in neighboring layers increases with the electric background field E_0 . At $E_0 = 0.50 (\mathcal{E}_c)$ the required gradient already reduced to $5.2 \cdot 10^{-3} \left(\frac{\mathcal{E}_c}{w_0}\right)$. For NaK this corresponds to $1.1 \frac{\text{kV}}{\text{cm}^2}$. At $E_0 = 1.5 (\mathcal{E}_c)$ the necessary gradient has again reduced by more than a factor of two.

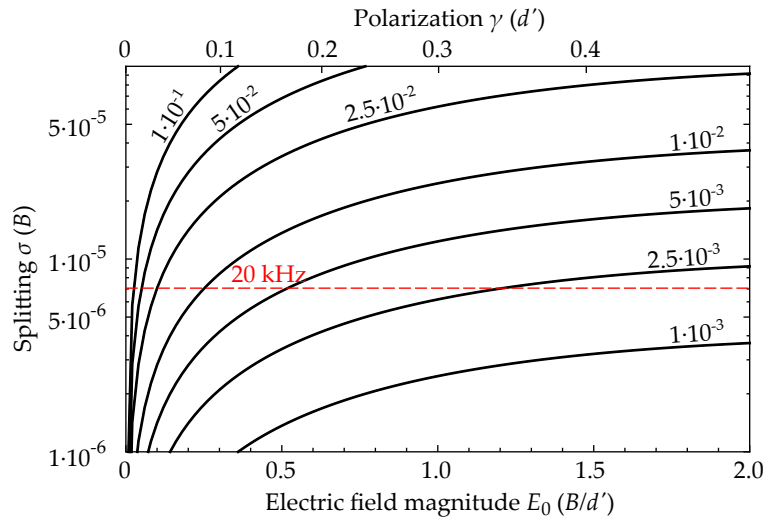


Figure 3.5: Gradient for splitting of layers. The contours give the gradient, in units of $\frac{\mathcal{E}_c}{w_0}$, necessary to achieve a certain splitting σ of the transition from $|A\rangle$ to the next ‘rotational’ level, $|B\rangle$, between two layers of an optical lattice spaced by 532 nm. The lower x-axis shows the applied a background field E_0 , the upper x-axis the corresponding polarization γ . A splitting of $\sigma = 20$ kHz, corresponding to a typical bandwidth of a microwave pulse, is indicated by the dashed line, for the case of NaK.

The above considerations also imply that a microwave pulse of a certain bandwidth implicitly sets a limit on spatial variations of the electric field: If the splitting of the addressed transition varies by more than the bandwidth over the volume of the trap, not all molecules go through the transition equally – also in optical lattices.

3.3 Electrode Configuration

After elaborating the general requirements on the electric fields, their actual implementation can be considered. Before drafting the electrode configuration which is required for the creation of the electric fields, the experiment setup, i.e. the main vacuum chamber's geometry, and the requirements on the electric fields are briefly reviewed.

The electrodes are implemented in the main vacuum chamber. A cross section of the chamber is sketched in Fig. 3.6. The central region is indicated by the sketch of a polar molecule. At this location, the molecules will be confined in the optical dipole trap and polarized by the applied electric field. Closest to this region are the two main vacuum windows of the chamber on which the electrodes are coated as an indium tin oxide (ITO) layer. ITO is electrically conducting and at the same time transparent in a broad range of the visible spectrum. This solution preserves huge optical access, while arbitrary electrode shapes can be defined on the surfaces of the vacuum windows. The diameter of the windows is 160 mm. Their spacing is 22 mm.

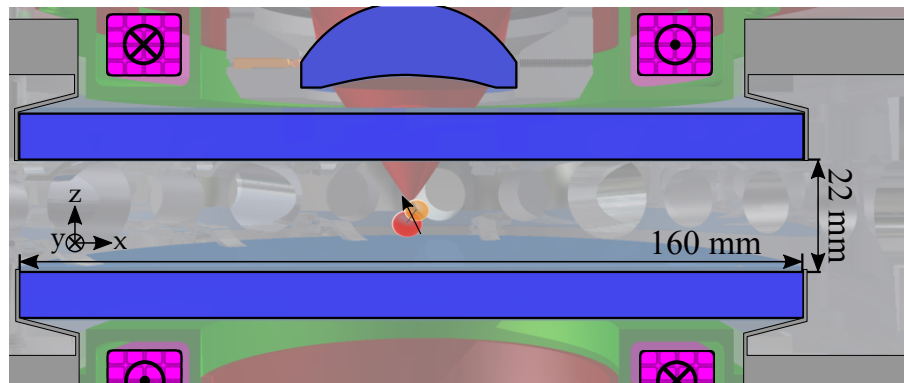


Figure 3.6: Cross section of vacuum chamber. with coils and high resolution imaging lens. The solenoids creating the the magnetic fields are shown in pink. The gray structures indicate the flanges in which the vacuum windows are mounted. The two main windows themselves are shown in blue. They are spaced by 22 mm. In the center of the upper solenoid the first lens of the high resolution imaging system is depicted. The sketch of a polar molecule in the center indicates the location of the trapping region.

As the main axis of the experiment is along the z direction, it is advantageous when the electric field can be rotated in a plane containing this axis and another axis of the optical lattice, e.g. in the x - z plane. Rotations in this plane will be obtained by the superposition of a very uniform field pointing along the x direction and a very uniform field pointing along the z direction.

One limit on the design of the electrodes is set by the possibility of surface discharging. In tests on air it was found that discharging between two ITO stripes will be avoided when they are separated by 7 mm or more and the potential difference between them does not exceed 10 kV. With surface discharging being highly dependent on the conditioning of the surface, these 7 mm are not necessarily the required spacing for the final setup.

In summary, the requirements on the electric fields in a polar molecules experiment are:

- The direction of the electric field should be rotatable at least in a two-dimensional plane spanned by two axes of the optical lattice, to explore the full variety of the dipolar interaction (Eq. (3.2)).
- The magnitude of the electric field should be tunable, to adjust the magnitude of the interaction (Fig. 3.1).
- The relative deviation of the field magnitude over w_0 should be below 10^{-5} , to maintain the confinement in an optical dipole trap, also at high polarizations (Table 3.1).
- An electric field gradient of about $10^{-2} (\frac{\xi_c}{w_0})$ should be available, to address transitions between rotational states in single layers of an optical lattice (Fig. 3.5).

When all four requirements on the electric fields can be fulfilled the electrode system can provide an extremely versatile repertoire of electric field configurations.

Using the turning knobs of electrode geometry and electric potentials, this section will lead the way to an ITO electrode layout which provides variable uniform electric fields for polarizing a trapped sample of molecules. For the experiment it is desirable to find the simplest and most robust electrode configuration fulfilling the requirements listed at the beginning of this section. Therefore, the first geometry investigated was the parallel plate capacitor.

3.3.1 Plate Capacitors

Parallel plate capacitors create very uniform fields at their geometric center. Thus they are highly applicable in experiments requiring uniform electric fields. However, the direction of their electric fields can only be changed by either turning the plates, or by using a second capacitor with a linearly independent electric field direction.

Considering two orthogonal capacitors with a plate spacing of 22 mm, the dimensions of the plates in this setup would be limited to about $136 \times 15 \text{ mm}^2$ to avoid discharging. The curvature-to-magnitude ratio resulting from this geometry is $|E_2/E_0| = 2.4 \cdot 10^{-5} (w_0^{-2})$. At field amplitudes of $E_0 = 10 \text{ kV/cm}$ this is already on the order of the critical curvature derived in Table 3.1. Hence, other possibilities are investigated.

3.3.2 Four Rods

An invitingly symmetric configuration are four infinitely long rods, extending in the y direction, which are arranged on the corners of a rectangle in the x - z -plane, as shown in the insets of Fig. 3.7. This arrangement is similar to a cylindric configurations with even higher symmetry [176]. The horizontal and vertical distances between the axis of the rods are $2l_1$ and $2l_2$, respectively. The electric potentials applied to the rods are $\pm V$.

In this configuration, vertical electric fields can be created by applying a potential $-V$ to the upper electrodes and a potential $+V$ to the lower electrodes. To obtain horizontal fields the applied potentials have to revolve by one rod. This configuration is analytically solved and the curvatures of the electric field magnitudes are plotted in Fig. 3.7. They are normalized by the electric field magnitude E_0 at the geometric center of the configurations, where the molecules would be trapped. Hence, the results are independent from

the applied potentials $\pm V$. In order to obtain results which are independent from the actual electrode spacing, the curvatures were also multiplied by $(l_2/w_0)^2$.

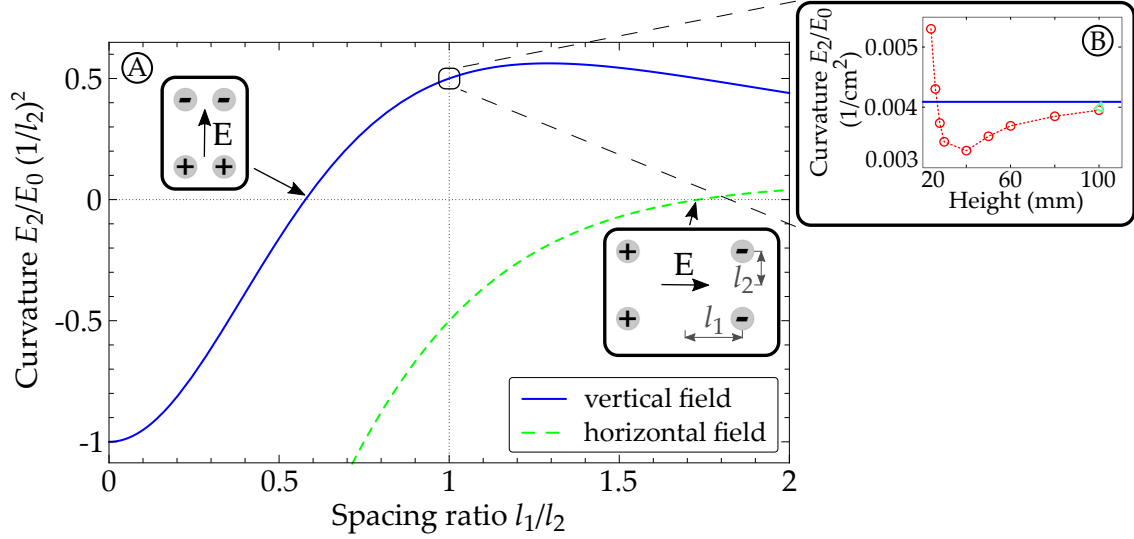


Figure 3.7: Curvature-to-magnitude ratio of electric field in case of four infinite rods. (A): Blue, solid line: Curvature-to-magnitude ratios of vertical electric field, $E_{2,v}/E_{0,v}$ normalized by the vertical electrode spacing l_2 , as a function of the horizontal to vertical electrode spacing ratio l_1/l_2 . Green, dashed line: Analog for horizontal fields $E_{2,h}/E_{0,h}$. The horizontal and vertical spacing for the electrodes are l_1 and l_2 . Insets: Geometric layout of four infinite rods in the x - z -plane. The electric potentials are indicated by '+' or '-'. The spacings correspond to the geometries for which the curvatures of vertical or horizontal electric fields vanish ($l_1/l_2 = 0.58$ or $l_1/l_2 = 1.7$), respectively.

(B): Blue line: Analytic solution for $E_{2,v}/E_{0,v}$ in case of $l_1 = l_2 = 11$ mm. Red circles: Results of COMSOL simulations, plotted as a function of the height of the volume which was used for the simulation. The diameter of the volume was 160 mm. The rods had a length of 133 mm. The lines serves as guide to the eye. Green triangle: the diameter of the volume was increased to 200 mm.

In the symmetric case, $l_1 = l_2 = l$, the curvature is, neglecting the sign, the same for vertical and horizontal fields $E_{2,v}/E_{0,v} = -E_{2,h}/E_{0,h} = 0.5(l_2^{-2})$. For $2l = 22$ mm the ratio is $|E_2/E_0| = 4.1 \cdot 10^{-5} (w_0^{-2})$.

Figure 3.7 directly indicates how the curvature of the electric field magnitude can be reduced. Because the field magnitude scales as $E_0 \sim V/l$, and accordingly the curvature in a fixed volume like $E_2 \sim Vw_0^2/l^3$, larger spacings l result in less deviation due to curvature, when considering the same probe volume. The potentials V required to maintain an electric field E_0 scale only linear and the positive effect would be quadratic in l .

When varying the ratio l_1/l_2 , the curvature E_2/E_0 changes significantly. At $l_1/l_2 = 0.58$, the curvature of the vertical field crosses zero, the same happens for horizontal fields at $l_1/l_2 = 1/0.58 = 1.7$. When canceling the curvature of a field pointing in the vertical direction with a ratio of $l_1/l_2 = 0.58$, the curvature of the horizontal field is $E_{2,h}/E_{0,h} = -1.50$. Therefore, two rectangular electrode configurations are required to obtain vertical and horizontal fields without curvature.

3.3.3 Configuration of Eight Rods

A combination of four ‘inner’ and four ‘outer’ electrodes can also be used to mutually compensate curvatures. If the spacings of the inner electrodes had a ratio

$$l_{1,i}/l_{2,i} < 0.58 \tag{3.20}$$

and the ratio of the outer electrodes was

$$l_{1,o}/l_{2,o} > 0.58, \tag{3.21}$$

the curvatures for vertical and horizontal fields can be canceled.

The insets (A), (B) and (C) of Fig. 3.8 illustrate how the desired fields are created. In (A) a vertical field is created by applying positive electric potentials to the lower and negative potentials to the upper electrodes. The curvature of the joint field of the inner ($l_{1,i}/l_{2,i} < 0.58$) and outer ($l_{1,o}/l_{2,o} > 0.58$) electrodes will be canceled, provided the potentials of the inner $\pm V_{\text{inner}}$ and outer $\pm V_{\text{outer}}$ electrodes are correctly adjusted. For horizontal fields, as shown in (B), the same idea holds, only the roles of inner and outer electrodes are interchanged⁷. Gradients in the vertical direction are obtained by adding an additional potential $+V_{\text{grad}}$ to the outer electrodes, as illustrated in (C). Different field magnitudes and directions in the x-z-plane are obtained by linear combinations of the given fields.

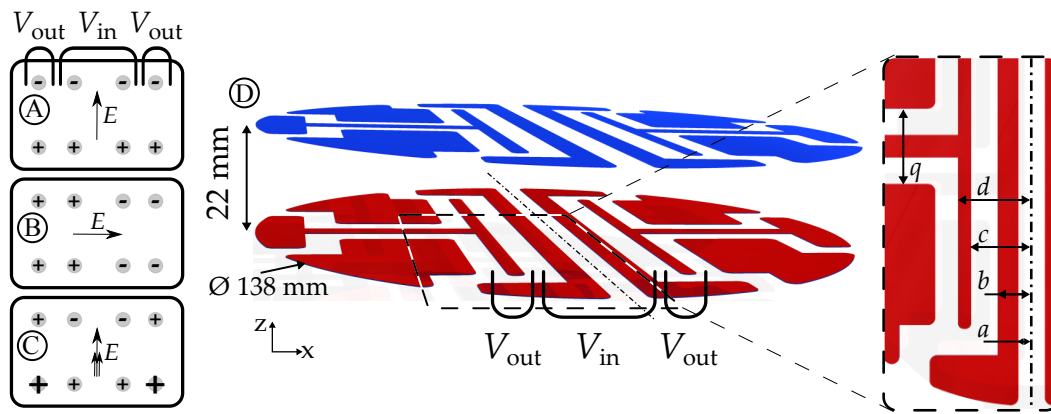


Figure 3.8: Layout of ITO electrodes. (A), (B) and (C) are, like in Fig. 3.3, cross sections through the electrodes, in this case of an eight rods system. The outer (inner) circles correspond to the outer (inner) electrodes. Three possibilities how the electrodes can be charged are shown. ‘+’ and ‘-’ only indicate the sign of the applied potential. (A) [B]: a uniform electric field in the z [x] direction is created. (C): corresponds to (A) with a superimposed gradient along the z direction. (D): The layout of the electrodes. Blue and red distinguish the coating on the upper and the lower window. Both are respective mirror images. The separation of both coatings is 22 mm, their diameter 138 mm.

A rendered graphic of the final ITO coating is shown in Fig. 3.8(D). It adopts the idea of eight rods. Eight ITO electrodes are coated on the upper, as well as the lower

⁷ The outer electrodes’ spacing ratio is $l_{2,o}/l_{1,o} < 0.58$ and its curvature can be compensated by the inner electrodes with $l_{2,i}/l_{1,i} > 0.58$.

window, respectively. The four central electrodes on each window are part of the eight ‘rods’ geometry. For the coating on the lower window (red) brackets identify the inner and outer electrodes. The four corner patches on each window shield the inside of the chamber from electric stray fields and can be used to compensate undesired gradients, which originate from manufacturing tolerances.

The curvature of the electric field magnitude is minimized by optimizing the free parameters a, b, c, d, q of the geometry, marked in the detail view of Fig. 3.8. The parameters were optimized in simulations, which were carried out with COMSOL Multiphysics. During the optimization the spacing of two electrodes was required to be at least 7 mm, to avoid surface discharging between different electrodes, as noted above. However, small spacings provide a better shielding of the molecules from stray fields. Hence, the spacing of the central gap was set to 7 mm, setting the value of the first parameter to $a = 3.5$ mm. The central gap in the coating also serves as a doorway for lasers far in the infrared that are absorbed by the ITO.

In Section 3.2.1, it was found that deviations in the electric field magnitude stem mainly from gradients and curvatures. Gradients in the electric field magnitude are avoided by the mirror symmetries of the electrodes’ geometry. Curvatures can only be minimized by optimizing the geometry of the electrodes, i.e. the free parameters b, c, d, q , while keeping the potentials on all electrodes similar, to avoid discharging between them.

The performance of a certain geometry was evaluated by importing it to COMSOL Multiphysics and computing the electric field magnitude⁸ created by the inner electrodes and the electric field magnitude created by the outer electrodes, in the cases of vertical and horizontal fields. Accordingly, for every geometry simulated, four curvatures of the electric field magnitude are extracted. Those are the curvature created by the inner electrodes and the curvature created by the outer electrodes, for vertical and horizontal fields, respectively: $E_{2,in,v}$, $E_{2,out,v}$, and $E_{2,in,h}$, $E_{2,out,h}$. This implies that inner and outer electrodes were always treated independently. When the field of the inner electrodes was simulated, the potential on the outer electrodes was set to zero, and vice versa. The electric potentials, which were applied to simulate the electric field created by the inner or outer electrodes had all the same absolute value V . The actual sign of the potential applied to a certain electrode is indicated in Fig. 3.8 (A) and (B). In this way every curvature computed is related to the same applied potential V .

Therefore, the inverse ratio of the curvatures which are created by the inner and outer electrodes indicates the ratio of the potentials which have to be applied to the electrodes to cancel curvature: $V_{in}/V_{out} = |E_{2,out}/E_{2,in}|$, or in other words:

$$V_{in}E_{2,in} + V_{out}E_{2,out} = 0. \quad (3.22)$$

⁸ When the electric field created by the inner and outer electrodes points in the same direction, it is sufficient to approximate the electric field by its magnitude. Neglecting the vector properties is a sufficient approximation, as the direction of the electric field generated by the inner and outer electrodes only differs slightly, over the volume of the dipole trap. Up to $w_0 = 0.1$ mm away from the symmetry center vertical fields created by the inner or the outer electrodes deviate by less than 10^{-4} from the z direction. As small deviations of the field’s direction enter the magnitude quadratically, neglecting those directional variations results in an error below 10^{-8} .

After computing these ratios for several geometries and both field directions, curves as shown in Fig. 3.9 are obtained. In this figure the curvature ratios $E_{2,in}/E_{2,out}$ for vertical and horizontal fields are plotted as a function of the parameter b . It is used to determine the parameter b which minimizes the potential difference between neighboring electrodes, on the same window. This potential difference is minimized for a curvature ratio of -1 [-3], in the case of vertical [horizontal] fields. For vertical fields the ratio is close to the desired value over a large range of b . Only for large b the curvature ratio is going to zero, as the inner electrodes extend far in the region of $l_1/l_2 > 0.58$ and compensate their field curvature themselves. For horizontal fields the curvature ratio is closest to -3 at $b = 9$ mm.

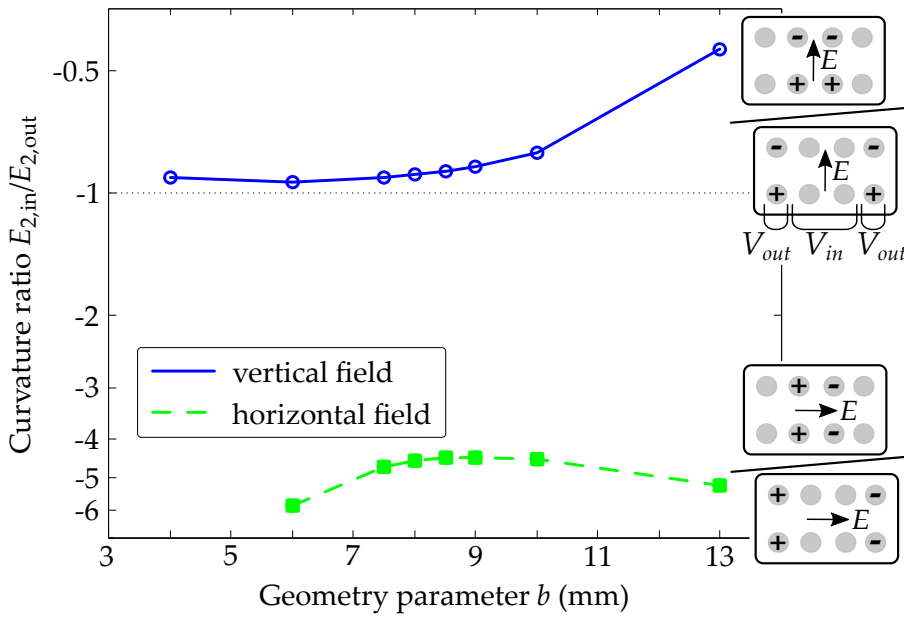


Figure 3.9: Curvature ratio of inner and outer electrodes. Ratio $E_{2,in}/E_{2,out}$ as a function of b . Blue points: Curvature ratios of vertical fields. Green squares: Curvature ratios for horizontal fields. The dotted line indicates the desired value of -1 for vertical fields. The insets indicate the configurations for which the ratios were taken. The lines serve as a guide to the eye.

For $b = 9$ mm the curvature of vertical [horizontal] fields⁹ can be exactly canceled by applying the potentials in a ratio of $V_{in,v}/V_{out,v} = 1/0.86$ [$V_{in,h}/V_{out,h} = 1/4.4$]. As noted above, the electric field magnitude is linear in the applied potential V , therefore changes in the potential are directly converted to the field. The curvature scales with $(w_0/l)^2$ and is more stable against those changes. Fluctuations in V are attenuated correspondingly. Considering a vertical electric field without curvature, a rise of $V_{out,v}$ by 5% affects the overall field magnitude by about $4.1 \cdot 10^{-3}$. The resulting relative curvature is only $9.7 \cdot 10^{-7}$, on length scales of the dipole trap (100 μm). Similarly this holds for the

⁹ The magnitude of the vertical field is dominated by the inner electrodes. Their electric field magnitude at the center is by a factor of eleven larger than the corresponding value of the outer electrodes. The outer electrodes only correct the curvature of the vertical field. The horizontal field is by a factor of three dominated by the outer electrodes.

potential of the inner electrodes and horizontal fields.

The same optimization can be performed for the other geometrical parameters. As the desired minimal spacing between electrodes is 7 mm, c cannot become smaller than $16.0 \text{ mm} = 9 \text{ mm} + 7 \text{ mm}$, which is its optimum value. The results do not strongly depend on d and q , thus small values were chosen, to enhance the effect of the corner patches. In summary the parameters of our electrode configuration are: $a = 3.5 \text{ mm}$, $b = 9.0 \text{ mm}$, $c = 16.0 \text{ mm}$, $d = 19.0 \text{ mm}$, $q = 20.0 \text{ mm}$.

A gradient allowing to address transitions between rotational states layerwise, as considered in Section 3.2.2 can be created by adding a potential V_{grad} to the outer electrodes. Due to the symmetry of the electrodes, the background field E_0 does not change. Adding $V_{\text{grad}} = +8.46 \text{ kV}$ to all outer electrodes results in a gradient of $3 \frac{\text{kV}}{\text{cm}^2} = 3 \cdot 10^{-2} \frac{\text{kV}}{w_0 \text{cm}}$. This gradient is sufficient to create the splitting considered in Section 3.2.2. The corresponding (vertical) electric background field of $1 \frac{\text{kV}}{\text{cm}}$ is obtained by $V_{\text{in,v}} = \pm 1.29 \text{ kV}$ and $V_{\text{out,v}} = \pm 1.11 \text{ kV}$.

The main purpose of the corner patches is to shield stray fields and to compensate unforeseen imperfections in manufacturing like a relative tilt of the vacuum windows¹⁰. Assuming that $10 \mu\text{K}/w_0$ are the critical potential gradient for the dipole trap, the electric field gradient must be smaller than $2.2 \cdot 10^{-4} \frac{\text{kV}}{w_0 \text{cm}} = 2.2 \cdot 10^{-2} \frac{\text{kV}}{\text{cm}^2}$ when the molecular sample is polarized to 68%, i.e. at an electric field of 10 kV/cm . At an electric field of 10 kV/cm , this gradient corresponds to a relative window tilt of about 0.29° . As the measured relative tilt of the windows in this setup is $(0.024 \pm 0.042)^\circ$ compensation is unnecessary.

The simulations were validated by comparing the analytic solution provided in Fig. 3.7 to results obtained with COMSOL Multiphysics. The solid, blue line in Fig. 3.7 (B) is the analytic solution for $E_{2,v}/E_{0,v}$ in the case of $l_1 = l_2 = 11 \text{ mm}$. The red circles are the corresponding values obtained by simulating a system of four 133 mm long rods. For each of the circles the height of the cylindrical volume in which the solution is computed was increased, starting from 24 mm up to 100 mm. The diameter of the volume was always 160 mm. Only for the green triangle the diameter was increased to 200 mm. With increasing height (volume), the values are converging to the analytical solution.

3.3.4 Main Windows

After the design of the ITO coating is determined it can be implemented in the experiment. This was done under the assumption of having a magnetic transport to the main vacuum chamber, which requires a lot of space. Hence, the ITO coating was deposited on vacuum windows with 160 mm diameter which are recessed in a CF200 flange, as shown in Figs. 3.6 and 3.10.

The material of the flange is 316LN stainless steel, the material of the sleeve holding the vacuum window 304L. The magnetic permeability of the sleeve was measured by MPF Products to be 1.005 to 1.010. These numbers are below the values usually expected for 304L (< 1.02) and tend to be comparable to those of 316LN. Between the window and the knife edge of each flange eight high voltage feedthroughs are arranged in a

¹⁰ The gradients they can compensate are $3 \cdot 10^{-2} \text{ kV/cm}^2$ along the y direction and $6 \cdot 10^{-2} \text{ kV/cm}^2$ along the x direction.

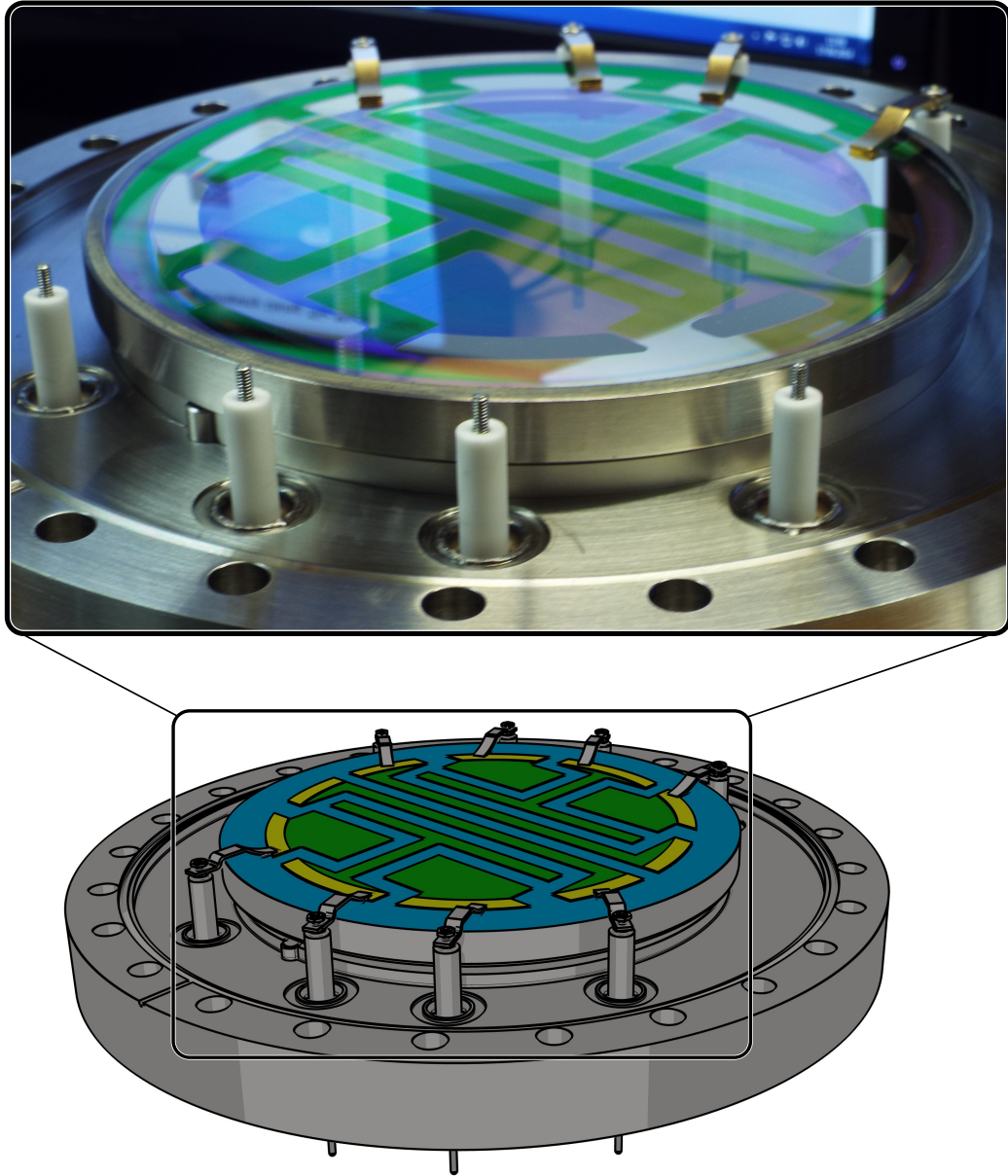


Figure 3.10: Electrodes on windows. The rendered graphic shows the CF200 flange (vacuum side). The flange, as well as the feedthroughs and the beryllium copper contacts colored gray. The window itself is depicted blue, the ITO coating green and the gold contacts yellow. The picture above shows a section of the flange (vacuum side). Four of the beryllium copper contacts are not mounted in this picture. The ceramic isolations of the high voltage feedthroughs are white. The ITO shows in a slight blue. A picture of window mounted in the main chamber is shown in Fig. 2.4.

mirror-symmetric configuration. This arrangement provides a 120 mm wide trace for the magnetic transport.

The vacuum windows themselves were anti-reflection coated on both sides, using magnetron sputtering (Optical coating system EOSS, Fraunhofer IST). On the vacuum side of the windows the ITO electrodes were deposited on top of the anti-reflection coating by pulsed DC sputtering from a ceramic target (DYSCUS, Fraunhofer IST). To contact the ITO coating 6 mm wide patches of a thick gold layer were deposited on the ITO with titanium as an adhesive layer in between. These gold patches are contacted to the high voltage feedthroughs via beryllium copper contacts. This compact arrangement – all on two flanges – is advantageous, because the whole configuration can be preassembled and is mounted to the chamber in form of the two CF200 flanges.

The ITO layer itself is 167 nm thick. As the transmission of ITO in the infrared is less favorable, the coating has a gap in the center where infrared vertical beams can pass. This gap is specified by the parameter a . The measured transmission of a single window at the sodium D2 line (589 nm) is > 99% in the regions without ITO and > 92% in the regions with ITO. At a wavelength of 1064 nm the transmission is 99.9% in regions without ITO, e.g. at the central gap. Detailed plots of the transmission, properties of the ITO and a summary of the layer structure can be found in Appendix A.5. The specific sheet resistance of the ITO was estimated to be $450 \mu\Omega\text{cm}$. The capacitance of the electrodes is negligible compared to the capacitance of the high voltage cables and hence could not be measured. The capacitance of the 2.5 m long, unshielded cables was measured to be 50 pF.

The most important points regarding the treatment of the vacuum windows are:

- The coating should never be cleaned with acid or basic solvents.
- It is best to use isopropanol or ethanol and a soft wipe for cleaning.
- The maximum temperature for the baking the flange itself is 200°C .
- Due to the ITO coating, baking should however not exceed 150°C [177].

3.4 Conclusion

Here a suitable electrode design for polarizing ultracold molecules was described. The requirements on the system were determined by considering the character of the dipolar interaction and investigating the effect of deviations in the electric field magnitude on the confinement of a polar molecule in an optical dipole trap.

All features of the dipolar interaction can be studied when the magnitude and the direction of the electric field at the location of the molecules can be changed. Using this electrode design, changing the direction and magnitude is possible by adapting the potentials on the electrodes creating the fields, while maintaining the confinement of the molecules in an optical dipole trap.

In context of the latter, it was found that gradients and curvatures are the main sources of electric field deviations in the volume of the dipole trap, because the ratio of the dipole trap waist to the characteristic length scale of the electrode geometry is only $\frac{0.1 \text{ mm}}{10 \text{ mm}} = 0.01$. The electrode geometry was designed to exclude gradients by symmetry. Curvatures are canceled by the geometry of the electrodes and the correct choice of the applied poten-

tials. In the volume of the optical dipole trap, the resulting electric field magnitude can be as uniform as $< 10^{-6}$, even when accounting for substantially false adjusted electric potentials.

The electrodes will be capable of creating electric fields which are continuously rotatable in a plane spanned by a horizontal and the vertical axis of the optical lattice. The maximum electric field magnitude will be about 10 kV/cm, which sufficient to polarize ground state molecules of NaK from zero to 68% of their internal dipole moment.

By applying electric field gradients along the direction of a one-dimensional optical lattice the rotational states of the trapped molecules can be addressed layerwise. At a background field of $1 \frac{\text{kV}}{\text{cm}}$ [$2 \frac{\text{kV}}{\text{cm}}$] the expected gradient of $3 \frac{\text{kV}}{\text{cm}^2} = 3 \cdot 10^{-2} \frac{\text{kV}}{w_0 \text{cm}}$ splits the transition between the two lowest rotational states ($|A\rangle, |B\rangle$) in two neighboring layers of an optical lattice (with 532 nm lattice constant) by 57 kHz [103 kHz].

The optical access given by the huge vacuum windows was mainly preserved, as the electrodes are implemented as a transparent indium tin oxide coating.

CHAPTER 4

High Resolution Imaging

The implementation of high resolution imaging in experiments with ultracold atomic gases paved the road to unprecedented analysis and manipulation of quantum phases in optical lattices. It allows the visualization of strongly correlated quantum systems in optical lattices down to the single-site [137, 138]. In combination with single atom sensitivity, it enables the extraction of correlation functions without loss of information due to coarse graining.

Since the very recent first implementation, many effects could be carefully analyzed on the single particle level. Among those are the superfluid to Mott insulator transition [138, 178], spreading of correlations [179], quantum walks [180] and nonlocal order in low dimensional systems [181]. Using tomographic methods, like an axial scan of the objective over multiple slices [182], the first step towards the imaging of three dimensional ensembles was done.

Recently, several high resolution systems were implemented for the elements ^{174}Yb [183], ^{40}K [184, 141] and ^6Li [185] extending the variety beyond the already implemented ^{87}Rb [137, 138] systems. It is however astonishing that no high resolution imaging system for sodium was reported until now, despite the comparably short wavelength of 589 nm on the commonly used D2 line.

In experiments with ultracold polar molecules, high resolution imaging is of great advantage to identify phases which can be distinguished by microscopic properties of their density distribution, as in the case of a checkerboard pattern [32]. At same time objectives with high spatial resolution allow the creation of tailored light potentials [137, 186] and the manipulation of ensembles on the single particle level [187].

This chapter introduces a two lens objective, applicable for imaging sodium atoms on the D2 line with single-site resolution in an optical lattice with 532 nm spacing. Its point spread function was measured by imaging gold nanoparticles at a wavelength of 589 nm. It corresponds to an Airy radius of 0.71 μm . The field of view has a radius greater than 0.1 mm. The working distance is about 22 mm. Simulations suggest that the objective can be adapted to vacuum windows between 6 mm and 10.5 mm thick, and to all imaging wavelength between 589 nm and 1100 nm. Smaller wavelength might be possible, but have not been tested experimentally.

The following sections will point out how NaK can be imaged, summarize imaging and define quality criteria for imaging systems. The main sections introduce the design of the objective and describe how it was experimentally characterized.

The content of this chapter will also be published elsewhere [188]. The following chapter is to some extent identical to this publication.

4.1 Imaging of Molecules

All experiments listed above use fluorescence imaging to obtain single-site resolution, even though it was shown that single atom sensitivity can also be obtained with absorption imaging [140]. Still, fluorescence imaging did prove to be superior in this respect [139, 136, 137, 138, 140], as single atom sensitivity in absorption images is limited by fluctuations of the background light. For high resolution, fluorescence imaging in optical lattices the detection of around 1 000 photons per atom was reported [141], which means a single atom scatters more than 10 000 photons. In an experiment directly imag-

ing KRb ground state molecules each molecule was scattering only 1.2 photons, due to the missing closed cycling transition [142]. A discrepancy of about four orders of magnitude.

The nearby solution is to split the molecules into their atomic constituents, which have closed cycling transitions. Each lattice site which was originally occupied by a molecule would then contain one sodium and one potassium atom. It is favorable to image the sodium atoms, due to the shorter wavelength of the D2 line. Before imaging sodium, potassium has to be removed from the optical lattice, to avoid light assisted collisions. This can be done by parametric heating [189] in the spirit of [190]: Benefiting from the different trap frequencies of sodium and potassium, the latter can be transferred to a higher band of the optical lattice, and subsequently be removed by means of gravity, e.g., via reducing the depth of the vertical optical lattice.

The efficiency of splitting the molecules into atoms might limit the single molecule sensitivity. For KRb the creation efficiency was reported to be 87(13)% [67]. The high uncertainty, however, was attributed to fluctuations in the STIRAP efficiency, which can in principle be 100%. Hence, detection fidelities on the order of 95%, which were reported for high resolution experiments [184, 185], will be feasible if the phase noise between both STIRAP lasers is small.

After having removed potassium, the sodium atoms can be detected via fluorescence imaging. During the imaging process it is important to prevent heating of the sample, due to photon recoil. A cooling mechanism must be provided. Optical molasses cooling as implemented for Rb [137, 138] could be challenging for light atoms like sodium [191], which experience a high velocity increase due to photon recoil. Suitable techniques for cooling and imaging sodium in an optical lattice, might be Raman side-band [192, 184, 185] and electromagnetically-induced-transparency cooling [193, 141], which were recently used for imaging atoms in optical lattices with single-site sensitivity.

Opening the way to cost efficient high resolution imaging of ultracold samples, this chapter introduces a two lens, long working distance objective. It is applicable for single-site detection of sodium in optical lattices with a lattice constant of 532 nm.

4.2 Imaging

The need to design special high resolution imaging systems for cold atom experiments stems from the typically thick windows of their vacuum chambers. Those create aberrations which cannot be corrected by commercial microscope objectives. In this experiment, the objective has to be adapted to a 9.525 mm thick window made of Corning HPFS 7980 fused silica. The specifications of that window are sufficient for high resolution imaging. Still a customized objective is necessary to correct for the window itself. In the following, I will first summarize the imaging process and the design strategy. I will then discuss the quantities that will be used to define the quality of the imaging system, with respect to aberrations.

4.2.1 General Terms

Here, imaging denotes the process of mapping a quasi two-dimensional object onto a two-dimensional image. In Fig. 4.1 a system of lenses realizes this mapping between the object plane (Obj) and the image plane (Img). This system of lenses is for now called imaging system. The charge-coupled device (CCD) of the camera is not considered to be part of the imaging system, even though its properties are important for the final result.

Often it is practical to divide the imaging system in two parts: The objective and the imaging lenses. In Fig. 4.1 both are indicated by one of the lenses. The objective will be designed for an infinite conjugate ratio. Accordingly, the object is placed in the focal plane of the objective which would create an image at infinity. The imaging lenses map this virtual image onto a real one in the image plane, the CCD of the camera. Another way to think of this process is that light emitted by a point source in the object plane is collimated by the objective and then focused onto the image plane by the imaging lenses.

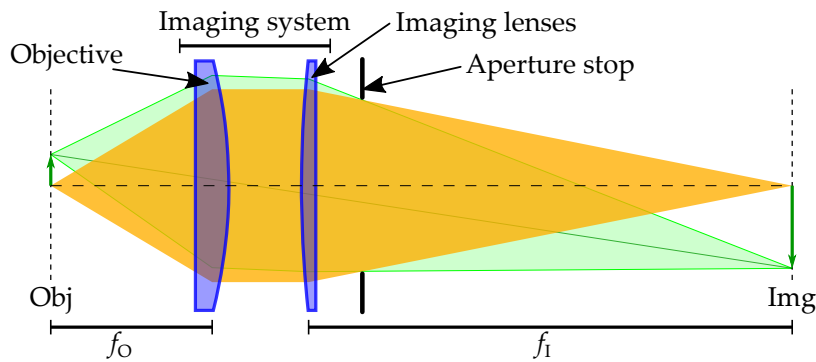


Figure 4.1: Sketch of a typical imaging system. The green arrows indicate the object and the image. A system of lenses maps an object from the object plane (Obj) onto the image plane (Img). In this case the objective is infinite conjugate, i.e. it forms an image at infinity that the imaging lenses map onto the image plane. f_o and f_i are the focal lengths of the objective and the imaging lenses.

The objective being infinite conjugate, separates the object side of the imaging system from the image side. Its a clear division of labor: the objective is adapted to the object, the imaging lenses to the image. Therefore, the design of the objective, which is usually the critical task, is completely independent of the actual image and the imaging lenses. This is also the reason why the CCD is not really considered here – the design of objective is independent from the CCD.

An example for the independence of objective and imaging lenses is the magnification

$$M = \frac{f_i}{f_o}. \tag{4.1}$$

It can be adjusted to nearly any value by changing the focal length of the imaging lenses f_i . No adjustments of the objective are required.

As two completely independent systems are designed, and the imaging lenses are going to be uncritical, this work focuses solely on the optimization of the objective. It can simply be optimized by improving the collimation of light emitted by a point source in the object plane to a quasi plane wave.

4.2.2 Quality Criteria

Before beginning the design, criteria for quantifying the performance of the imaging system should be defined. In the time domain, a system is well characterized by its response to a step function. In the same way, imaging systems can be characterized by their response to a point source emitting light. The image of a point source is called the point spread function (PSF). It reveals the spread of an image of a point source. Even the most perfect imaging system will exhibit such a spread, because the light field creating the image is diffracted on the aperture stop of the system.

With Fourier optics¹, the shape of the diffraction pattern can be calculated. As the light is diffracted on the aperture stop, the PSF is the square of the absolute value of the exit pupil function's Fourier transform:

$$\text{PSF} = |\mathcal{F}[P(x, y)]|^2, \quad (4.2)$$

$P(x, y)$ being the complex valued exit pupil function. In the ideal case, of no aberrations, $P(x, y)$ describes a spherical wavefront in the exit pupil and is zero outside.

In an aberration free imaging system with a circular aperture stop, the image of a point source is described by an Airy disk

$$\text{PSF} \sim \left(2 \frac{J_1(r)}{r}\right)^2. \quad (4.3)$$

A cross section of an Airy disk is shown in Fig. 4.2. Its geometry is determined by J_1 , the first order Bessel function of first kind. The radial coordinate r is centered with the ideal image of the point source in the image plane.

The first radial root of the Airy disk is called Airy radius r_{Airy} . It is solely determined by the system's numerical aperture A and the imaging wavelength λ :

$$r_{\text{Airy}} = \frac{1.22\lambda}{2A}. \quad (4.4)$$

The Rayleigh criterion states that two point sources can be resolved when they are spaced by at least the Airy radius. This statement implicitly rescales the Airy radius, in principle an effect observed in the image plane, to the object plane. This will also be done here. According to this convention, the Airy radius of a system is then obtained using the numerical aperture of the object side in Eq. (4.4).

Even though the Airy radius is widely used to specify resolution, structures smaller than the Airy radius still can be imaged with a significant residual contrast. This becomes evident when computing the Fourier transform of the PSF. Its magnitude, the modulation transfer function (MTF), gives the contrast as a function of the spatial frequency.

$$\text{MTF} \sim |\mathcal{F}[\text{PSF}]| \quad (4.5)$$

¹ Note that the following relations consider the paraxial approximation and incoherent light.

Using Fourier optics an image I_i is obtained by rescaling the object I_o with the magnification M and convolving it with the PSF

$$I_i(x_i, y_i) = I_o(x_o, y_o) \circ \text{PSF}.$$

The coordinates in the object plane and image plane are denoted (x_o, y_o) and $(x_i, y_i) = M \cdot (x_o, y_o)$.

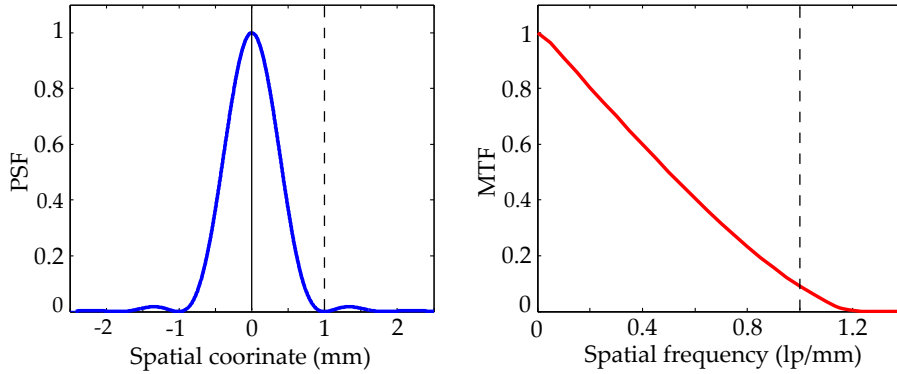


Figure 4.2: Relation between Airy disk and MTF. The left graph shows the profile of an Airy disk with an Airy radius of 1 mm. The right graph the corresponding MTF as a function of the spatial frequency in line pairs per mm ($\frac{\text{lp}}{\text{mm}}$). At the frequency corresponding to the Airy radius the MTF still shows significant contrast. The cutoff frequency is at $1.22 \frac{\text{lp}}{\text{mm}}$.

The MTF is hence the response of a system to a sinusoidal intensity pattern. Figure 4.2 shows the cross section of an Airy disk and the corresponding MTF, which was computed via a fast Fourier transform (FFT). The MTF indicates that, as mentioned above, at spatial frequencies above the inverse of the Airy radius the contrast can still be sufficient. The contrast actually does not go to zero until the cutoff frequency

$$f_c = \frac{2A}{\lambda} . \tag{4.6}$$

The MTF is directly related to the contrast transfer function (CTF) [194], which is the systems response to an infinite square wave pattern. Square wave patterns are more commonly available on test targets, like the USAF 1951 resolution chart, but they are often limited to a finite number of bars. In such a case the measured contrast has to be corrected for finite size effects [195, 196].

4.2.3 Aberrations

In reality, physical limitations, imperfections in the design or manufacturing tolerances make it impossible to avoid aberrations. Therefore, imaging systems cannot solely be quantified by their numerical aperture and the imaging wavelength, i.e. the Airy radius or the cutoff frequency. Informations about the aberrations are required. Comprehensive lists of aberrations can be found in the vast variety of books on optics [197]. The following paragraph focuses on their quantification.

The smallest spot in the image plane is formed when the phase front exiting the imaging system is spherical. In this case the PSF corresponds to the Airy disk. In a system with aberrations, the phase front exiting the imaging system deviates from the ideal spherical shape, as illustrated in Fig. 4.3. The deviations from the ideal spherical shape depend on the type of aberrations and can be expressed as an additional phase factor multiplied to the exit pupil function

$$P(x, y) \rightarrow P(x, y) \cdot e^{i\phi(x, y)} . \tag{4.7}$$

When comparing different systems, the additional phase factor is summarized in form of its root mean square, the so called root mean square wavefront error (RMS). It summarizes the aberrations of a system in a single number, usually given in units of $\lambda_{633} = 632.8 \text{ nm}$. It is consensus to classify a system as diffraction limited², when the RMS wavefront error is below 0.072λ , with λ being the imaging wavelength.

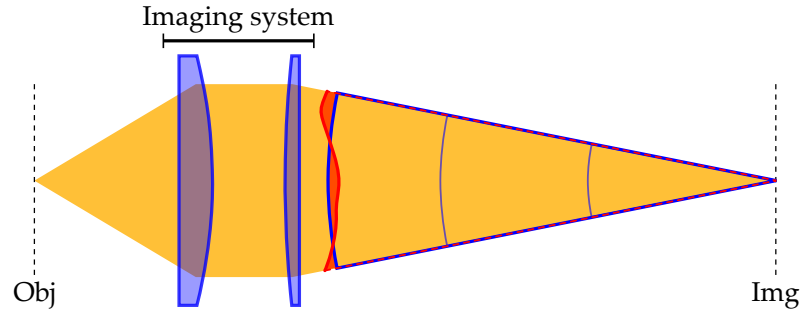


Figure 4.3: Illustration of the wavefront error, shown in red. Due to imperfections of the imaging system the exiting wavefront deviates from the ideal spherical shape. The root mean square deviation from this ideal shape can be used to quantify aberrations.

According to Eq. (4.2) the additional phase factor of Eq. (4.7) requires the central value of the PSF to be less than in the ideal case.

$$\text{PSF}_{\text{RealSystem}}(0) \leq \text{PSF}_{\text{IdealSystem}}(0) \quad (4.8)$$

The Strehl ratio expresses this inequality, directly indicating how close a real system is to its aberration free counterpart. It is defined as the central value of a system's PSF divided by this value the same system would have if no aberrations were present.

$$\text{Strehl} = \frac{\text{PSF}_{\text{RealSystem}}(0)}{\text{PSF}_{\text{IdealSystem}}(0)} \leq 1 \quad (4.9)$$

A value close to 1 indicates an aberration free system. In practice a system is considered diffraction limited when its Strehl ratio is above 0.80. Due to the properties of Fourier transformations, the Strehl ratio can also be determined by comparing the volume below the system's MTF to that of the same system without aberrations [196]³:

$$\text{Strehl} = \frac{\iint \text{MTF}_{\text{RealSystem}} df_x df_y}{\iint \text{MTF}_{\text{IdealSystem}} df_x df_y} \quad (4.10)$$

In the presence of aberrations, the MTF exhibits a sag at medium frequencies. In bad cases this sag can even touch zero. The value at the origin and at the cutoff frequency are however fixed.

² The resolution of the system can be considered to be limited by the diffraction on the aperture stop.

³ Actually I would prefer: $\text{Strehl} = \frac{\iint \text{OTF}_{\text{RealSystem}} df_x df_y}{\iint \text{OTF}_{\text{IdealSystem}} df_x df_y}$, with OTF being the optical transfer function $\text{OTF} \sim \mathcal{F}[\text{PSF}]$ and accordingly $\text{MTF} \sim |\text{OTF}|$. In the case of diffraction limited systems, i.e. $\Im(\text{MTF}) \rightarrow 0$ and accordingly $\text{MTF} \rightarrow \text{OTF}$, Eq. (4.10) holds.

Until now, different points in the object plane were not distinguished. As the imaging quality usually decreases with the distance from the optical axes it is necessary to define a field of view in which the imaging is diffraction limited. Due to the radial symmetry of most imaging systems, the field of view can be represented by the distance from the optical axis for which the Strehl ratio is above 0.80. In practice the field of view can also be limited geometrically by the size of the CCD divided by the magnification.

4.3 Ideal System

After having defined criteria which can be used to rate an imaging system, the requirements on a specific imaging system can be expressed. For the design of a high resolution objective, operating at 589 nm, the following demands were stated:

- i) An Airy radius smaller than $0.7\ \mu\text{m}$, to permit single-site resolution in an optical lattice with a lattice constant of 532 nm [138].
- ii) The imaging system should be diffraction limited, to profit from the small Airy radius.
- iii) The diffraction limited field of view must have a radius of $100\ \mu\text{m}$, to acquire images of complete two-dimensional layers.
- iv) The design has to be simple, to avoid complications.
- v) Costs should be low, to keep the implementation realistic.

Fulfilling requirement i) is simple, in principle. At the sodium D2 line an Airy radius below $0.7\ \mu\text{m}$ requires a numerical aperture of at least 0.52. The difficulties hide in the combination of i), ii) and iii) which requires to minimize the aberrations of a system with a high numerical aperture, also for objects far from the optical axis. The points iv) and v) are tackled on the way.

The objective was optimized with the ray tracing and optimization software Zemax 12. Because the objective is designed to be infinite conjugate, the imaging lenses, which are expected to be uncritical, did not have to be considered for the optimization. However, it is important to include the vacuum window, through which the atoms are going to be imaged, in the optimization. As mentioned above, this window is the only reason for a custom objective, i.e. its impact on the imaging system is significant.

Finally, a situation as shown on the left side of Fig. 4.4 is obtained: The light emitted by a point source passes the vacuum window and is collected by the objective. For the optimization in Zemax it is convenient to mirror the optical setup, as shown on the right side of Fig. 4.4. In this configuration the objective can be optimized to focus a collimated beam to a diffraction limited spot by minimizing the RMS. Note that the mirroring turned the object plane into the image plane.

4.3.1 Optimization Definitions

In detail, the following situation for the optimization is defined: The objective is optimized under the assumption of radial symmetry with respect to the optical axis. In the reversed system the required numerical aperture of 0.52 corresponds to an image space

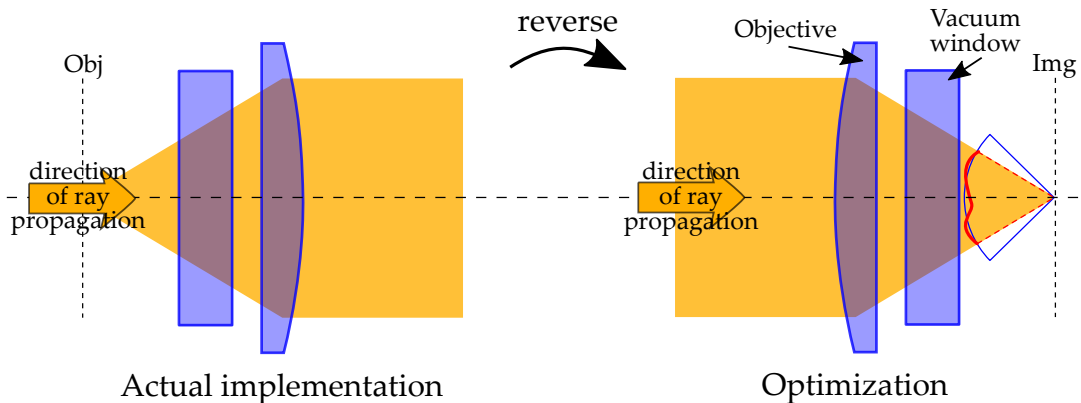


Figure 4.4: Illustration of optimization. In Zemax beams usually propagate from left to right. The left side shows the major components which have to be considered. The right side shows the mirrored configuration which is used for optimization. In this reversed configuration the RMS, indicated by the red line, is minimized. Boundary conditions like a maximum thickness of optical elements, etc. have to be considered. The horizontal, dashed line indicates the optical axis.

f-number⁴ of 0.96. To ensure an optimal shape of all surfaces also slightly outside of the required apertures the image space f-number was set to 0.89 during the optimization.

To optimize the objective over the required field of view three collimated, incoming light fields were defined. One of them is parallel to the optical axis. It will be focused on the intersection of the image plane and the optical axis and defines the center of the field of view. The other two light fields enter the objective under slightly different angles, such that their chief rays intersect the image plane at 50 μm and 100 μm distance from the optical axis. These three fields ensure that the objective will be optimized over the desired field of view with 100 μm radius.

The design wavelengths are set to 0.5891 μm , 0.5892 μm and 0.5893 μm to avoid a singularity in the performance.

After those general settings an initial geometry of the optical elements was implemented in Zemax. It was found that the objective requires two lenses⁵ to meet the desired specifications. Figure 4.5 shows the already optimized design as an example.

In Zemax optical elements are defined using successive surfaces. Their type, shape and the material between them defines the optical elements. For the optimization all properties of the surfaces and materials can be varied. On the surface Img, the last surface in Fig. 4.5, the performance of the objective, in this case the RMS, is evaluated. In the experiment this surface would correspond to the location of the atoms which are going to be imaged (reversed system). Accordingly, the spacing between Img and surface 7 is 11 mm to simulate the space between the vacuum window and the atoms. The surfaces 6 and 7 define the 9.525 mm thick vacuum window made of Corning HPFS 7980. Because the vacuum chamber already exists, all parameters of the three surfaces 6, 7 and Img were fixed during the optimization. Also the spacing between the surfaces 5 and 6 was fixed,

⁴ f-number = $\frac{\text{focal length}}{\text{entrance pupil diameter}}$

⁵ In the beginning it was not clear that the objective will use two lenses. A solution with only a single lens was also attempted, but finally rejected as it was not adaptable enough.

and with it the distance of the objective to the vacuum window.

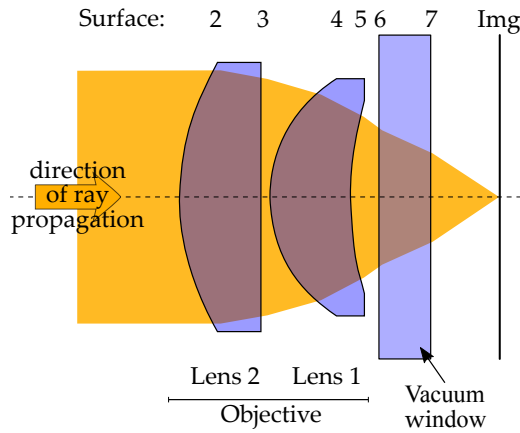


Figure 4.5: Optical elements of the optimization. For the optimization of the objective all optical elements are mirrored. In this reversed configuration the objective focuses a collimated beam entering from the left onto the plane of atoms which is now the image plane. The surfaces have the same numbering as in the optimization.

The shapes and spacings of the surfaces 2, 3, 4 and 5, which define the lenses of the objective, as well as the glass type of the lenses were optimized under certain restrictions on the shapes. Convex surfaces, namely 2 and 4 could be aspheric⁶, whereas 3 and 5 were restricted to be spheric. This restriction on surface 3 and 5 reduces manufacturing tolerances. During first optimizations it was found that good results could be obtained with a plane surface 3, which again reduces manufacturing tolerances and costs.

Having set the restrictions on the surfaces, a merit function with further geometric constraints was defined. The merit function aimed to reduce the RMS of all defined fields, at the specified wavelengths and for the given image space f-number. The geometric constraints in the merit function are necessary to obtain realistic results, not a lens several meters thick.

4.3.2 Optimization Results

During the first optimization, it was found that glasses with a low refractive index tended to result in a better performance. As images will only be taken at a single wavelength, chromatic aberrations are irrelevant and a single glass type is used for both lenses. This is N-BK7, a very common glass with relatively low refractive index. N-BK7 is robust, relatively hard and hence good to process.

The geometric results of the optimization are summarized in Table 4.1. When increasing the image space f-number to 0.96, which corresponds to the desired numerical aperture of 0.52 in the real system, the desired Airy radius of 0.69 μm was obtained. The RMS is below 0.03, the Strehl ratio 0.98. Both numbers indicate a diffraction limited performance. Figure 4.7 shows that the simulated ideal MTF is extremely close to the

⁶ The equation for the shape of aspheres is: $z = \frac{cr^2}{1 + \sqrt{1 - (1+k)c^2r^2}} + \alpha_1r^2 + \alpha_2r^4 + \alpha_3r^6 + \dots$; r is the radial coordinate, z the axial one.

| Surface | Type | Radius (mm) | Thickness (mm) | Glass |
|---------|--------------|-------------|----------------|--------|
| Obj | Plan | Infinity | Infinity | |
| 2 | Even Asphere | 45.017 | 15.000 | N-BK7 |
| 3 | Sphere | Infinity | 1.752 | |
| 4 | Even Asphere | 25.883 | 15.000 | N-BK7 |
| 5 | Sphere | 65.929 | 6.500 | |
| 6 | Plan | Infinity | 9.525 | C79-80 |
| 7 | Plan | Infinity | 11.000 | |
| Img | Plan | Infinity | | |

Table 4.1: Surfaces as given in the Zemax lens data editor. These values are already the results of the optimization. The coefficients of the aspheric surfaces are: [Surface 2: $\alpha_1 = 0$; $\alpha_2 = -9.483 \cdot 10^{-7}$; $\alpha_3 = -6.754 \cdot 10^{-10}$] [Surface 4: $\alpha_1 = 0$; $\alpha_2 = -1.272 \cdot 10^{-7}$; $\alpha_3 = -8.936 \cdot 10^{-10}$]. All other terms are zero.

diffraction limit of the system. The first inset shows that the diffraction limited field of view has a radius of about $150 \mu\text{m}$. The corresponding depth of field can be estimated to be approximately $2 \mu\text{m}$ from the second inset.

On the one hand those results are comparable to experiments which have shown single-site resolution [138] in a lattice with $0.532 \mu\text{m}$ spacing. On the other hand all clear apertures of the system can, despite the large working distance of more than 22 mm , be significantly smaller than 2 in , which is practical and cost-efficient.

After having optimized the design of the objective, the imaging lenses can adapted to create a magnification of about 40. This magnification provides a sufficient sampling rate [198], of $\frac{40 \cdot 0.69 \mu\text{m}}{6.45 \mu\text{m}} = 4.3$, on the CCD of a pco.pixelfly usb ($1392 \times 1040 \text{ px}^2$), with a pixel size of $6.45 \times 6.45 \mu\text{m}^2$, while still enabling a geometric field of view of $220 \times 170 \mu\text{m}^2$. This field of view is now set by the CCD of the camera and the magnification, but it is well balanced with the $150 \mu\text{m}$ radius which was obtained in the optimization of the objective. Based on the effective focal length of the objective $f_O = 41.3 \text{ mm}$ a magnification of 40 requires the focal length of the imaging lenses to be 1.65 m . A pair of two identical lenses (PLCX-50.8-1545.0-UV, CVI) with a combined focal length of $f_I = 1678 \text{ mm}$ provides a magnification of $M = 40.6$. The large focal lengths, i.e. radii, of these lenses ensure reduced spherical aberrations and less sensitivity to misalignments.

Simulating the combined system of the objective and the imaging lenses the Airy radius in the image plane is $28 \mu\text{m}$ ($= 40.6 \cdot 0.69 \mu\text{m}$). The Strehl ratio and RMS are above 0.97 and below 0.03, respectively. This confirms that the imaging lenses do neither reduce the numerical aperture nor the performance of the system.

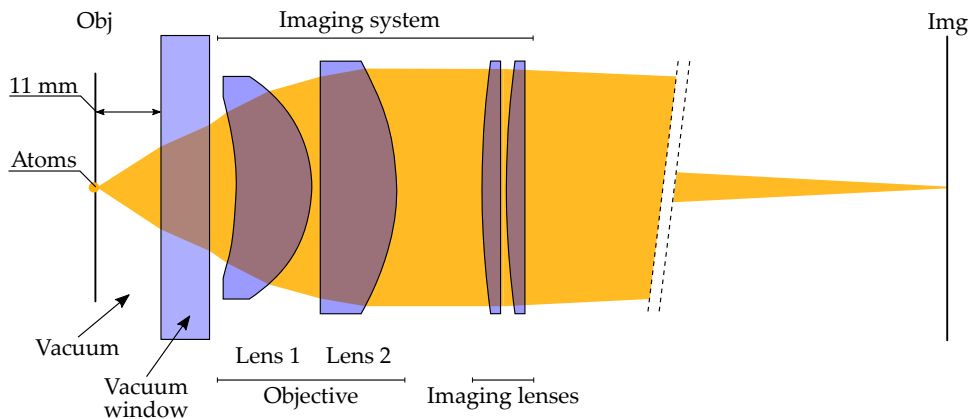


Figure 4.6: Cross section of the imaging system. The supposed sample of atoms is in the object plane (Obj). After propagating 11 mm of vacuum the light from the object passes a 9.525 mm thick vacuum window made from Corning HPFS 7980. Directly behind the window the imaging system, composed of the objective and the image forming lenses, collects the light emitted from the object plane. The objective consists of the two lenses to be designed. It creates an infinite conjugate image which the image forming lenses map onto the image plane (Img). The numbering of the lenses is consistent with Fig. 4.5.

4.4 System Tolerances

In reality, the performance of the imaging system which was calculated in Section 4.3 will suffer from manufacturing tolerances. The tolerances for the lenses of the objective are given in the upper part of Table 4.2.

In this section, Zemax is used to estimate the influence of these manufacturing tolerances and the properties of the vacuum window on the performance of the imaging system. For the following tolerance analysis, all parameters of the system were fixed, except the spacings of the surfaces 3 and 4, as well as 5 and 6, i.e. the distance between the lenses and the distance of the objective to the vacuum window. As this section will refer to those spacings multiple times they will be denoted as 3-4 and 5-6.

4.4.1 Tolerances of the Objective

The manufacturing tolerances of the lenses, as listed by the manufacturer, are given in Table 4.2. Because the lenses built for the objective might actually show such deviations from the ideal specification, it is important to consider their effects. Either their effects are sufficiently small, or the deviations have to be compensated, for example by the mounting position of the lenses. A tolerance analysis in Zemax showed that the most problematic tolerances listed in Table 4.2, namely those of center thickness and radii, can be compensated by adjusting the spacings 3-4 and 5-6. Therefore, those spacings must be variable in our objective. This is not undesirable because variable axial spacings come with other major benefits, which are discussed below.

The remaining most critical tolerances ('worst offenders') are: surfaces which are not centered with the optical axis due to the diameter tolerance, irregularities of the aspheric surfaces and tilts of the surfaces with respect to the optical axis due to centering errors.

The corresponding RMSs, listed in the lower section of Table 4.2, are all small enough, to permit diffraction limited performance at a f-number of 0.96.

Table 4.2 also indicates that the system is comparably insensitive to the mounting of individual components. The highest RMS in this context, related to a centering error of lens 1, is only 0.030. This reduces the requirements on the precision of the mount in which the lenses are placed.

| Tolerances | | | Value | Unit | | |
|-----------------------------|--|--|----------------|---------------------|--|--|
| Tolerance | | | | | | |
| Center thickness | | | ±0.1 | (mm) | | |
| Radii | | | 3 | (λ_{633}) | | |
| Diameter | | | +0.00 -0.02 | (mm) | | |
| Irregularities (aspherical) | | | 0.3 | (λ_{633}) | | |
| Centering error | | | 0.5 | (arcmin) | | |
| Irregularities (spherical) | | | 0.1 | (λ_{633}) | | |

| Worst offenders | | | Value | Unit | RMS wavefront error (λ_{633}) for $F_{\#} = 0.89$ for $F_{\#} = 0.96$ | |
|-----------------------------|-----------|--|---------|----------|------------------------------------------------------------------------------------|-------|
| Tolerance | Element | | | | | |
| Diameter | Surface 4 | | ±0.015 | (mm) | 0.089 | 0.066 |
| Irregularities (aspherical) | Surface 2 | | -0.0002 | (mm) | 0.15 | 0.064 |
| ⋮ | | | | | | |
| Irregularities (aspherical) | Surface 4 | | +0.0002 | (mm) | 0.054 | 0.051 |
| Diameter | Surface 5 | | ±0.015 | (mm) | 0.064 | 0.048 |
| Centering error | Surface 6 | | ±0.49 | (arcmin) | 0.060 | 0.044 |
| Centering error | Surface 7 | | | | | |
| ⋮ | | | | | | |
| Centering error | Lens 1 | | ±0.49 | (arcmin) | 0.037 | 0.030 |
| ⋮ | | | | | | |

Table 4.2: Manufacturing tolerances of lenses and resulting RMS. The upper table lists the manufacturing tolerances of the lenses, as provided by the manufacturer. The lower table shows the RMSs resulting from the most critical of those tolerances, in decreasing RMS, according to our analysis. The two columns show the RMS for a system with image space f-numbers ($F_{\#}$) of 0.89 and 0.96. The RMS is given in units of the wavelength $\lambda_{633} = 632.8$ nm. It is computed for the reversed system shown in Fig. 4.5. As the most critical tolerances, radii and center thicknesses, can be compensated via the spacings between the surfaces 3-4 and 5-6 they are not listed in the table.

For the f-number 0.96 the quadratic sum of all RMSs expected from tolerances is 0.12. This is not diffraction limited, but still considered to result in ‘nearly perfect image quality’ [199]. The MTFs shown in Fig. 4.7 confirm this. They show that the ideal

system nearly reproduces a diffraction limited system. An axial shift of the image plane (reversed system) by $1\ \mu\text{m}$, denoted as defocus, still permits diffraction limited performance. When surface 4 is off center with respect to the optical axis by $15\ \mu\text{m}$ still results in a diffraction limited performance, even though the diameter tolerance of surface 4 is the worst offender of performance. For double the off-center of surface 4 the MTF sags more significantly, indicating that the relation is not linear.

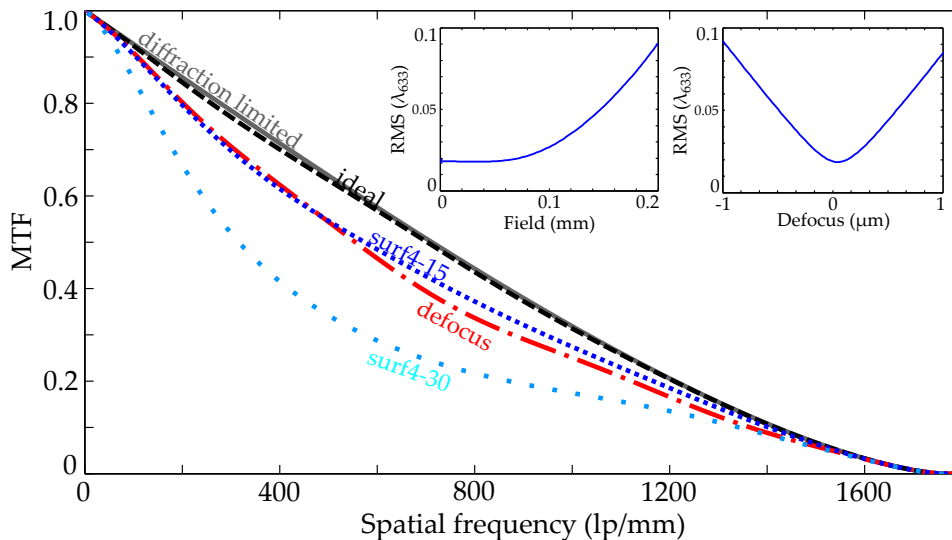


Figure 4.7: Simulated modulation transfer function of the system shown in Fig. 4.5. As the objective is radially symmetric cross sections of the MTF are shown. In the case of non symmetric aberrations the stronger affected cross section is shown.

The gray line indicates the MTF of a diffraction limited system with a numerical aperture of 0.52. The black dashed line includes the aberrations of the ideal, perfectly aligned system. The red, dash dotted line shows the effect of a $1\ \mu\text{m}$ axial shift of the image plane. The dotted lines indicate the effect when surface 4 is off center with respect to optical axis by $15\ \mu\text{m}$ or $30\ \mu\text{m}$.

The insets show the RMS as a function of the distance of the focal point from optical axis (Field) and as a function of an axial shift of the image plane (Defocus).

4.4.2 Effect of Compensators

Above, it was shown that the variable axial spacings 3-4 and 5-6 are necessary to optimize the objective to diffraction limited performance. In addition to the most critical tolerances of the objective, most properties of the vacuum window can also be compensated by adjusting them⁷. To determine the ultimate performance of the objective it was optimized after all parameters were fixed and the constraints on the 'compensators', 3-4 and 5-6, were released. This instantaneously led to a slightly improved off axis performance of the objective, shown in Table 4.3.

⁷ Due to their radial symmetry those 'compensators' are most effective for tolerances which are radially symmetric.

| System | Distance 3-4 (mm) | Distance 5-6 (mm) | Strehl on-axis | Strehl off axis |
|--------------|-------------------|-------------------|----------------|-----------------|
| Re-optimized | 1.762 | 6.498 | 0.99 | 0.98 |
| Original | 1.752 | 6.500 | 0.99 | 0.97 |

Table 4.3: This table compares the spacings 3-4 and 5-6 in the reoptimized system to the originally designed system. In the reoptimized system the constraints on the spacings 3-4 and 5-6 were released. The last two columns compare the Strehl ratios on the optical axis and 0.1 mm away from it.

As the spacings 3-4 and 5-6 are used to optimize the objective in the experiment, it is crucial to know which effect they have on the performance. Figure 4.8 indicates that the objective is significantly more sensitive to the spacing 5-6, but also an incorrect adjustment of 3-4 reduces the Strehl ratio. A non optimal adjustment of one spacing can, however, be compensated by the other one. In this case a drop of the Strehl ratio is not visible for the values shown.

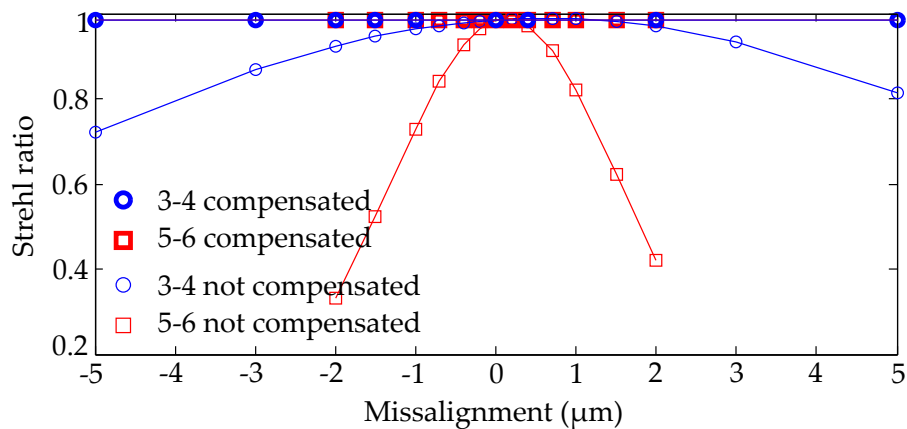


Figure 4.8: Strehl ratio for varying spacings 3-4 and 5-6. The thin blue circles and red squares give the Strehl ratio for an objective in which the spacing 3-4 or 5-6 was varied from the optimal value while the respective other spacing was not optimized. The amount of variation is given on the x-axis. The thick blue circles and red squares show the Strehl ratio for an objective in which the respective other spacing was optimized. All lines serve as a guide to the eye.

4.4.3 Air versus Vacuum

The objective is designed for operation on the vacuum chamber, but it is tested in an environment on air. During these tests the volume between the vacuum window and the test target is not empty, but filled with air. The effects can be computed in Zemax by replacing the vacuum between surfaces 7 and 1mg by air. When compensating this with the spacings 3-4 and 5-6 the Strehl ratios on the optical axis and 100 μm away from it, i.e. on the boundary of the desired field of view, stay the same. Table 4.4 compares the Strehl ratios and the correct spacings 3-4 and 5-6 for both situations, on vacuum and on air.

| System | Distance 3-4 (mm) | Distance 5-6 (mm) | Strehl on-axis | Strehl off axis |
|--------|-------------------|-------------------|----------------|-----------------|
| Air | 1.762 | 6.498 | 0.99 | 0.98 |
| Vacuum | 1.786 | 6.490 | 0.99 | 0.98 |

Table 4.4: The table compares spacings 3-4 and 5-6 and the Strehl ratio of the ideal objective, when operated in a test setup on air or on the vacuum chamber. For both cases the spacings 3-4 and 5-6 were optimized. This comparison only considers the change of the refractive index, not the bending of the vacuum window due to the atmospheric pressure. This bending is treated independently in Section 4.4.5.

4.4.4 Other Wavelength

The possibility to adjust the spacings 3-4 and 5-6 is however not only necessary to compensate manufacturing tolerances. It makes the objective extremely versatile, too. Due to the variable axial spacings, the objective can be used to image atoms at other wavelengths. The necessary adjustments of the spacings 3-4 and 5-6 are shown in Fig. 4.9. The Strehl ratio (not depicted) confirms diffraction limited performance over the whole wavelength range. Nevertheless, the resolution is proportional to the Airy radius, which increases linearly with the wavelength. At shorter wavelengths the resolution should become better, but aberrations like surface irregularities will have a stronger effect and might prevent diffraction limited performance. Consulting Table 4.2 a slight improvement at shorter wavelengths is, however, expected.

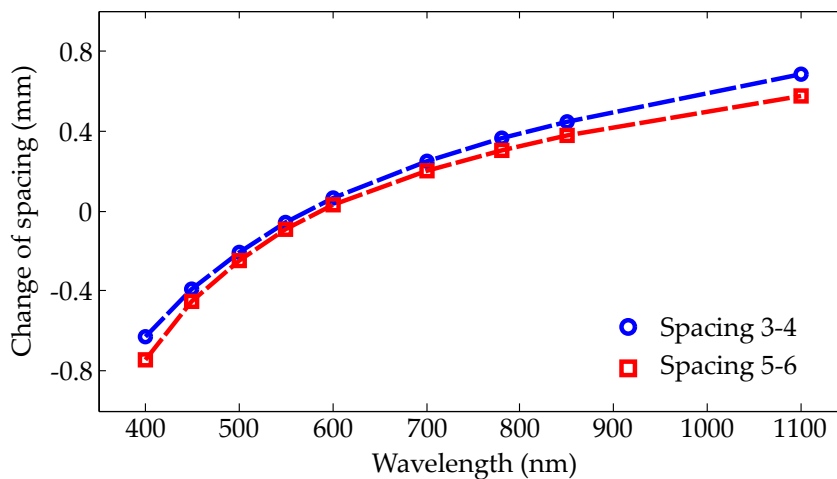


Figure 4.9: Adjustments of the spacings 3-4 and 5-6 which optimize the objective as a function of the wavelength. The blue circles and red squares show the changes necessary for an optimal performance. The reference spacings are 1.762 mm for 3-4 and 6.498 mm for 5-6. The Strehl ratio ranges from 0.96 at 400 nm to 0.99 at 1100 nm. All lines serve as a guide to the eye.

The system cannot be operated outside the wavelength range given in Fig. 4.9, as below 400 nm N-BK7 and above 1100 nm HPFS 7980 become non transmissive.

4.4.5 Window Properties

The wavelength is not the only parameter to which the objective can be adjusted. It can also be adapted to a great variety of vacuum window properties and hence to many different experiment chambers.

An example is the adjustability to any window thickness between 6 mm and 10.5 mm, while a Strehl ratio of at least 0.97 can be maintained. The necessary changes of the spacings 3-4 and 5-6, plotted in Fig. 4.10, are linear in the window thickness. It is not possible to adapt the objective to thicknesses above 10.8 mm, as the spacing 3-4 would become negative. Below a thickness of 8 mm the diffraction limited field of view starts to decrease this is however tolerable down to 6 mm.

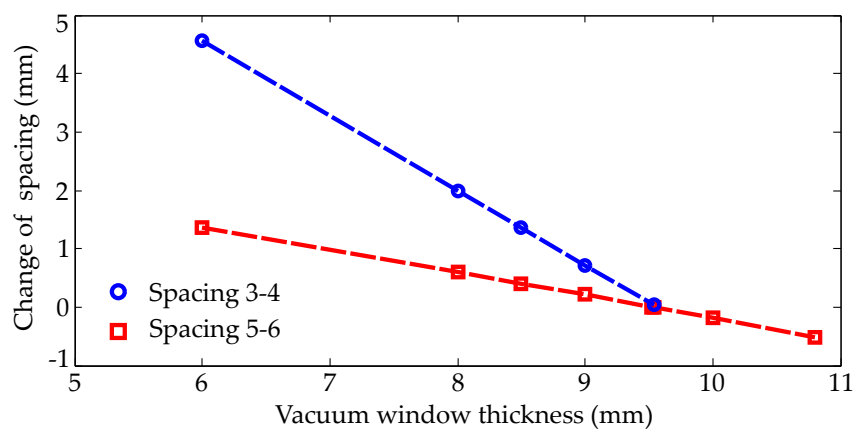


Figure 4.10: Adjustment of the spacings 3-4 and 5-6 to a different vacuum window thickness. The blue circles and red squares show how the spacings 3-4 and of 5-6 have to be adjusted to provide an optimal performance at different thickness of the vacuum window. The reference spacings are 1.762 mm for 3-4 and 6.498 mm for 5-6. For thinner and thicker windows the on-axis Strehl ratio does not drop significantly. All lines serve as a guide to the eye.

As noted above the vacuum window bends under atmospheric pressure. In Zemax this bend was modeled by spheric surfaces, corresponding to a quadratic approximation of the window deformation in the central region. Figure 4.11 shows the necessary adjustments of the spacings 3-4 and 5-6 to compensate the bending at different radii down to 1 m. When compensated, the performance of the objective is diffraction limited over the complete field of view, at all bending radii shown.

However, the Strehl ratios of the non optimized and optimized objective show, that a compensation of the window bend is absolutely necessary for diffraction limited performance. For this experiment, the bending radius of the windows was measured to be 14 m, confirming that it can be compensated.

Due to the radial asymmetry, a tilt or wedge of the vacuum window cannot be fully compensated by adjusting the spacings 3-4 or 5-6. Meanwhile, tilting the objective permits a diffraction limited performance up to 0.94° tilt or 0.16° wedge. Figure 4.12 indicates that a wedge has stronger effects on the performance than at tilt. In this setup the tilt of the vacuum windows was measured to be below 0.1° . The wedge of the window is specified to be below 0.003° . This means, both do not limit the imaging performance.

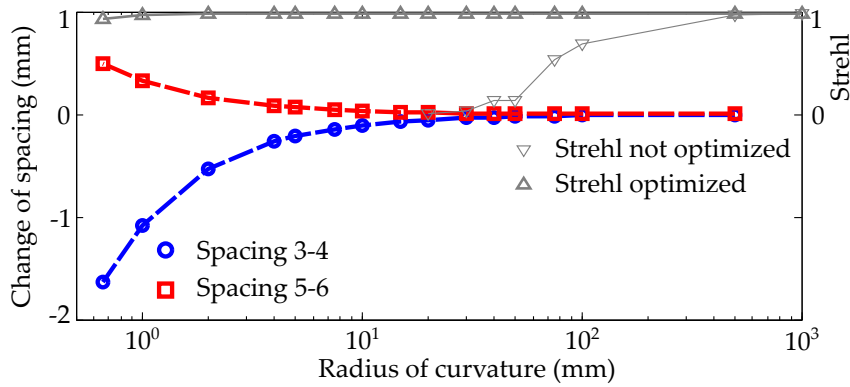


Figure 4.11: Objective adjustment to a bending of the vacuum window. The blue circles and red squares show how the spacings 3-4 and of 5-6 have to be changed for an optimal performance at different bending radii of the vacuum window. The reference spacings are 1.762 mm for 3-4 and 6.498 mm for 5-6. The down and up pointing triangles show the Strehl ratio for the non-/optimized objective. The on axis Strehl ratio of the optimized system goes to 0.94 for strong a bending with a radius of 0.67 m. All lines serve as a guide to the eye.

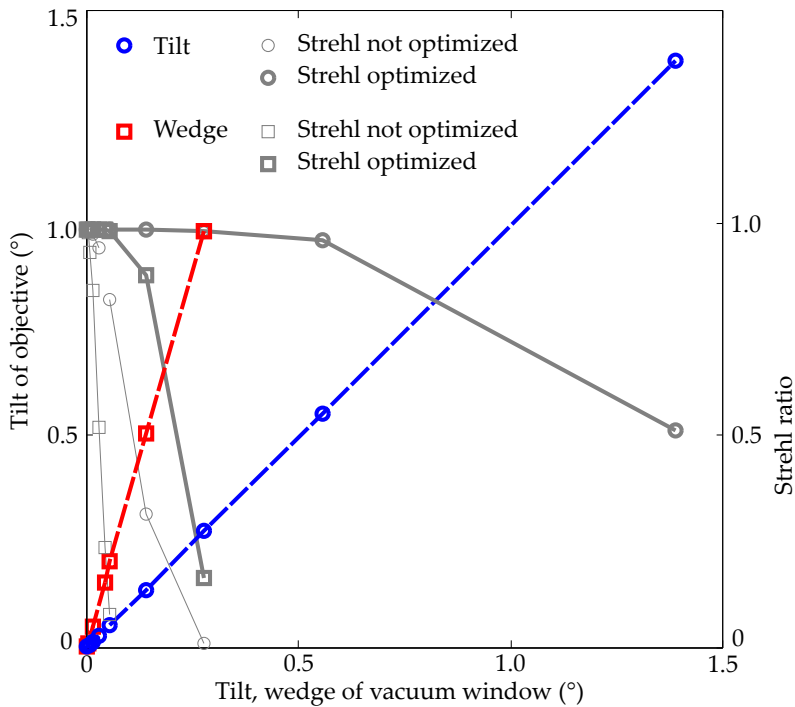


Figure 4.12: Tilt of the objective necessary to compensate a tilt or wedge of the vacuum window. The blue circles and red squares correspond to the correction of tilt and wedge. The thin gray symbols indicate the Strehl ratio when the tilt or wedge of the vacuum window are not compensated. The thick gray symbols show the Strehl ratio when the objective is tilted to compensate the tilt or wedge of the vacuum window. All lines serve as a guide to the eye.

The ITO coating which was introduced in Chapter 3 creates more severe aberrations. As it is gapped, like shown in Fig. 3.8, light actually passing through ITO has a longer optical path than light passing in a gap of the structure. The central gap along the y direction is 7 mm wide. As this gap is not radially symmetric with respect to the optical axis the performance of the imaging in the transverse plane has to be balanced. At an ITO thickness of 100 nm [150 nm] this leads to an RMS of 0.08 [0.11]. This is not diffraction limited anymore, but still nearly perfect [199].

The tolerances of the imaging lenses are neglected.

4.5 Mounting

According to the last section, the mounting of the two lenses in the objective is not as critical for the performance as the manufacturing tolerances of individual surfaces. Still, it is severely more critical than the mounting of other components. The approach, shown in Fig. 4.13, minimizes the free parameters to those necessary for achieving diffraction limited performance and otherwise relies on precise manufacturing of the mount. Only the spacings 3-4 and 5-6, as well as the overall tilt of the objective can be adjusted.

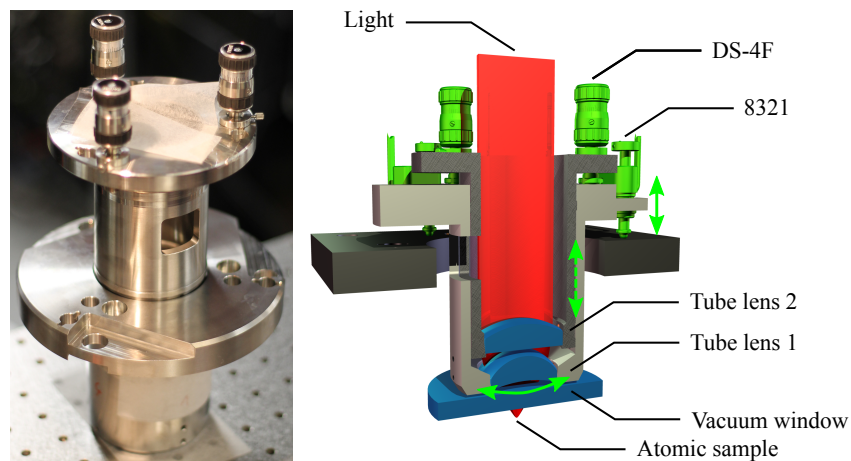


Figure 4.13: Objective Mount. The two lenses are mounted in stainless steel tubes, sliding in another. The spacing between the two lenses (dashed arrow) is adjusted with a Newport DS-4F. The spacing of the objective from the vacuum window, as well as its tilt are adjusted with a three point mounting (solid arrows) relying on three New Focus 8321.

Each of the two lenses is mounted in a stainless steel tube. Both tubes are custom lathed to slide in another. The spacing 3-4, of the lenses, is adjusted with a differential micrometer screw (DS-4F, Newport). The complete objective itself is supported on a three point mount that can be adjusted via three picomotor actuators (8321, New Focus). Those picomotor actuators adjust the distance 5-6, of the objective to the vacuum window, and the overall tilt of the objective in steps of less than 30 nm or $0.04''$.

The imaging lens pair is mounted in a commercial tube system (SM2L30C, Thorlabs) and placed on top of the objective mount. A silver mirror (PFE20-P01, Thorlabs; mounted: modified KCB2E/M, Thorlabs) placed over the imaging lenses reflects the light onto the CCD.

4.6 Characterization

In a test setup, it was investigated whether the computed performance can actually be achieved in the experiment. The test setup mimics the experiment as realistically as possible. All components of this setup are mounted on a breadboard which is to a certain degree vibration isolated (PWA075, Thorlabs). The resolution target is mounted horizontally. It can be illuminated with laser light at a wavelength of 589 nm either from below, or at an angle of 30° from the side/top. When the target is illuminated from below, a laser speckle reducer (LSR-3010, optotune) is used. The camera used is the pco.pixelfly usb.

As already discussed above, the medium between the test target and the vacuum window can be air instead of vacuum, the objective performs equally well. In the test, the vacuum window is substituted by a glass substrate (Laser Optik). Above the window the objective and the imaging lenses are supported by the three point mount. The silver mirror is mounted independently.

As the glass substrate replacing the vacuum window is 0.020 mm thicker than the original vacuum window, the magnification in the optimum alignment decreases from 40.6 to 40.1. Figure 4.10 showed that the thicker glass can be compensated using the spacings 3-4 and 5-6. The necessary adjustments are shown in Table 4.5, which also indicates that the image quality is not influenced.

| System | 3-4 (mm) | 5-6 (mm) | Strehl on-axis | Strehl off axis |
|-----------------------------|----------|----------|----------------|-----------------|
| Window thickness (9.525 mm) | 1.762 | 6.498 | 0.99 | 0.98 |
| Window thickness (9.545 mm) | 1.736 | 6.490 | 0.99 | 0.98 |

Table 4.5: Spacings 3-4 and 5-6 and Strehl ratio for different window thickness The optimal spacings 3-4 and 5-6 for the objective were computed using Zemax. The first line gives the results for a window thickness of 9.525 mm, as it is expected to be found in the experiment. The second line shows the results for a thickness of 9.545 mm as it is found in the test setup.

Now, the magnification is confirmed, with a 1951 United States Air Force resolution test chart (USAF chart), before the PSF of the system is determined by imaging 100 nm gold nanoparticles.

4.6.1 1951 USAF Resolution Test Chart

Evaluating several elements of a USAF chart confirmed the magnification of the test setup to be 40.2 (4). From the same images the contrasts of group 9 of the USAF chart were determined. Table 4.6 compares them to the values expected from Zemax computations. The low measured contrast can partially be attributed to the bad alignment during the magnification measurement, but could also be a first indication for the sag of the measured MTFs shown in Fig. 4.17.

The smallest feature available on this USAF chart⁸ is element 3 of group 9. The corre-

⁸ Other resolution targets provide more line pairs per mm. The Geller MRS 4.2 for example ($500 \frac{\text{lp}}{\text{mm}}$, $1000 \frac{\text{lp}}{\text{mm}}$, $2000 \frac{\text{lp}}{\text{mm}}$).

sponding $645 \frac{\text{lp}}{\text{mm}}$ are far from the $1760 \frac{\text{lp}}{\text{mm}}$ which are expected to be the cutoff frequency of the objective at a wavelength of 589 nm. As the CTF cannot be interpolated between those values the resolution of the objective, or more precisely the contrast at other spatial frequencies had to be determined with a different method.

| USAF chart group/element | CTF (Zemax) | CTF (Measured) |
|--------------------------|-------------|----------------|
| 9/1 | 0.78 | 0.68 |
| 9/2 | 0.75 | 0.69 |
| 9/3 | 0.69 | 0.61 |

Table 4.6: Contrast transfer function of the imaging system. The table compares the values of the CTF measured by imaging group 9 of a 1951 USAF chart resolution test chart to those which are computed using Zemax. For this comparison the measured values were converted to the infinite square wave target using [195, 196], assuming a linear scaling. The objective was not perfectly adjusted for this measurement.

4.6.2 Point Spread Function - Pinhole

A versatile method to determine the resolution of an imaging system is to examine its response to a point like light source, its PSF.

Trying to determine the PSF by imaging a pinhole failed [200]. The pinhole (56-272, Edmund Optics) has a nominal diameter of 1 μm but its shape was not well enough defined to allow an accurate determination of the PSF, even with attempted deconvolution. To confirm the doubts about the measurement, Fig. 4.14 shows an image of the pinhole, taken with a scanning electron microscope. The scale of the image is provided by the diameter of the green circle which corresponds to 1 μm .

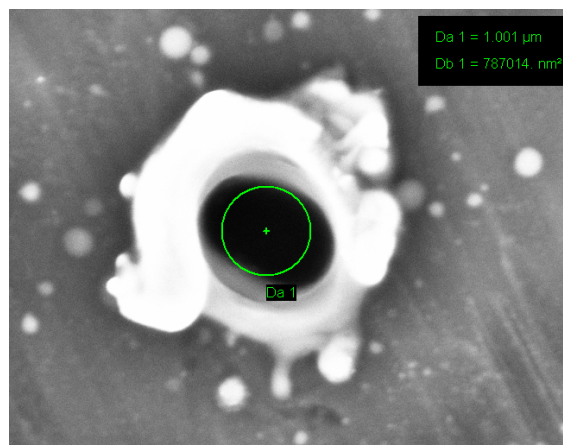


Figure 4.14: Pinhole imaged with scanning electron microscope. The diameter of the green circle corresponds to 1 μm . The image was taken at the Physikalisch Technische Bundesanstalt, Braunschweig by Peter Hinze.

4.6.3 Point Spread Function - Nanoparticles

A reliable method to determine the PSF of the system was to image gold nanoparticles, illuminated at a wavelength of 589 nm. Because of their small diameter the nanoparticles are very close to point like for this objective, and small relative deviations of their size or shape become unimportant.

Target

The gold nanoparticles⁹ used for the characterization have a nominal diameter of 100 nm and were deposited on a glass substrate (VPW42-A, Thorlabs). The diameter of the particles is a compromise of two different requirements: On the one hand, they are small compared to the Airy radius, which makes their influence on the PSF negligible. On the other hand, the photon scattering rate of the particles at a wavelength of 589 nm is still sufficiently high at this diameter.

Before the nanoparticles were deposited, the substrate was cleaned with acetone in an ultrasonic bath and then rinsed with doubly distilled water. A hundredfold diluted solution of nanoparticles was exposed to the ultrasonic bath for ten minutes, before the solution was pipetted on the substrate. After three minutes of waiting time the substrate was rinsed and afterwards dried on air, protected from dust. The successful deposition of gold nanoparticles was confirmed by bright field and confocal microscopy. A cut bright field image is shown in the top right corner of Fig. 4.15.

The method of imaging gold nanoparticles has certain advantages compared to e.g. the USAF chart. Besides being a cheap method, incredibly large test targets can be produced. Thus the resolution over the full field of view can be probed simultaneously.

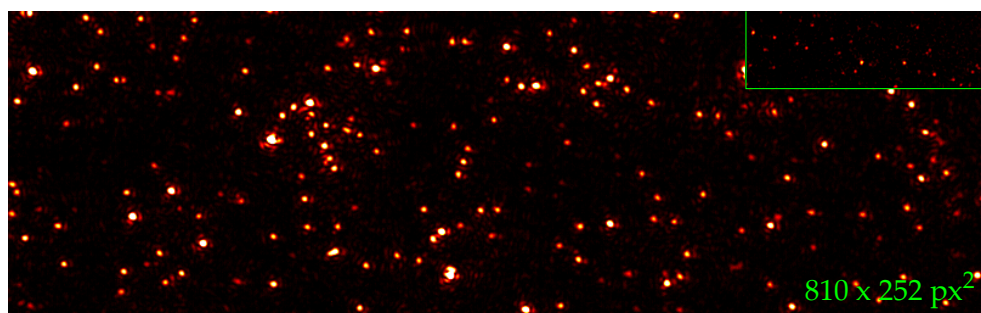


Figure 4.15: Image (false color) of gold nanoparticles taken with the test setup. An area of $810 \times 252 \text{ px}^2$ is shown. Assuming that the magnification is 40.2 this image is rescaled to the object plane and magnified by a factor 1000. Weak signals are enhanced in this presentation.

The inset in the top right corner is a bright field image (false color) of the deposited nanoparticles taken with a Leica DCM 3D. It is to scale, the contrast was however significantly enhanced in post-processing.

⁹ nanoComposix: NanoXact, BPEI, 100 nm Gold Spheres, 25 mL; mean diameter: 100(5) nm; relative standard deviation: < 15%

Procedure

During the tests the deposited gold particles are illuminated with 589.2 nm light from the sodium laser system (Chapter 2). The sample is illuminated from the side, under an angle of 30°. The imaging system collects photons scattered off the nanoparticles. While continuously imaging the particles, the objective was optimized regarding distance to the target and tilt. As the gold particles are distributed over the whole field of view, the resolution can be probed locally. When the objective was nearly perfectly adjusted, the power of the background light was on the order of the first Airy ring which limited the final alignments. In this context, a negative target with small holes in a non transparent coating would be advantageous. Close to the optimum adjustment several images of the sample were taken. The images were recorded using μ Manager¹⁰ [201].

Evaluation

The evaluation is constrained to the images with the smallest average FWHM of imaged gold particles. The average neglects large clusters and all single particle fits with a FWHM significantly larger or smaller than the average. This means only features which are presumably single nanoparticles are taken into account. The FWHMs were determined by fitting two-dimensional Gaussians to the gold nanoparticle images using Fiji¹¹ [202, 203]. In this pre-evaluation nine images were selected for further evaluation.

The following evaluation assumes that the image of a nanoparticle is only determined by the PSF of the imaging system. The spatial extent of the nanoparticles has a negligible effect on their images, because their diameter is significantly smaller than the expected PSF of the imaging system. This is confirmed by the numeric convolution of a disk with 100 nm diameter and an Airy disk of 0.69 μ m radius. The convolution indicates that the finite spatial extent of a 100 nm disk increases the FWHM of the image by only 0.4%, compared to the system's PSF. A disk with 120 nm diameter results in an increase of 0.6%. Therefore, the following analysis neglects the finite dimensions of the nanoparticles. Also, anisotropic scattering off nanoparticles is neglected.

For the further evaluation of the selected nine images, a derivate of PolarCam (Chapter 2) was used. In each of the nine images on the order of fifty nanoparticle images were selected. Their centers were determined by two-dimensional Gaussian fits. The areas surrounding the centers were copied and each pixel was divided into a 50×50 subpx² subpixel grid. All subpixel nanoparticle images of a single image were averaged, taking care that the centers of the Gaussian fits did coincide. Accordingly, for each of the nine images one average nanoparticle image is obtained. The boundaries of the of the nine averaged nanoparticle images were cropped, such that the area is 800×800 subpx² $\sim 16 \times 16$ px² in size and the centers of the Gaussian fits are in the middle. The side length of 16 px correspond to 3.6 Airy radii of the expected PSF. Assuming the Gaussian fits determined the centers well, the error due to discrete subpixels is 0.009 Airy radii.

¹⁰ Together with the dynamic link libraries from pco: pco.micro-manager Installation Guide V1.20

¹¹ Plugins - GDSC SMLM - Fitting - Gaussian Fit, Fiji Is Just ImageJ.

A manual for the GDSC SMLM plugins is available at:

http://www.sussex.ac.uk/gdsc/intranet/microscopy/imagej/smlm_plugins.

In a first step, a two-dimensional Gaussian is fitted to each of the nine averaged subpixel nanoparticle images. The major axes of the Gaussians are oriented along the direction of the pixels. The average FWHM of all nine images is $d_G = 0.57$. This can be related to an Airy radius of $r_{\text{Airy,G}} = 1.19 \cdot d_A = 1.19 \cdot 1.04 \cdot d_G = 0.71^{+0.02}_{-0.03} \mu\text{m}$, d_A being the FWHM of an Airy disk. The error of the Airy radius combines the error of the magnification, the finite extent of the nanoparticles, the discrete subpixel size, the error of the individual fits and the statistical error over those fits. An example of averaged subpixel data is shown in the inset of Fig. 4.16, together with the corresponding Gaussian fit. The data in this plot is based on an average of 30 nanoparticle images, extracted from a single image.

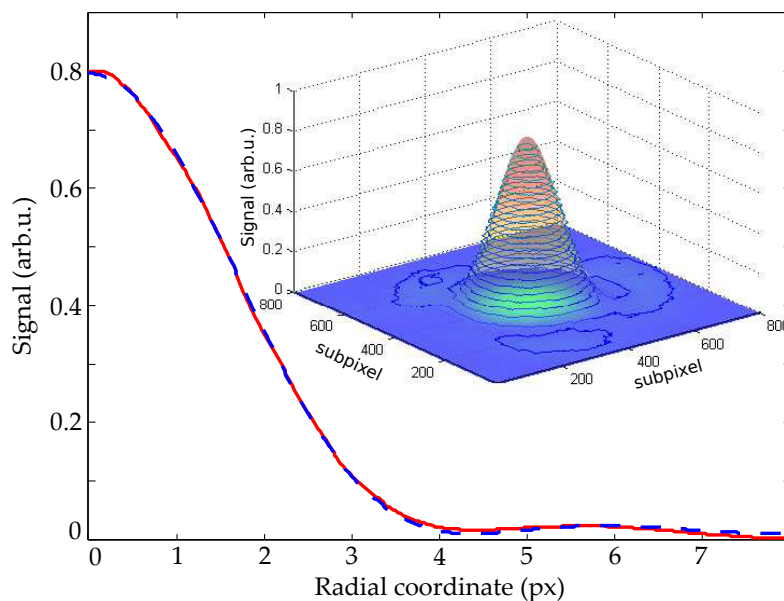


Figure 4.16: Radially averaged images of gold nanoparticles. For the inset the images of 30 gold nanoparticles of image 03-30_28 where subpixel averaged. This average is shown in form of a three dimensional contour plot, the two-dimensional Gaussian fit to this data as a color coded surface. The axes of the Gaussian fit are oriented along the transversal directions of the CCD. The FWHM convert to an Airy radius of $0.71 \mu\text{m}$ and $0.69 \mu\text{m}$ in the transversal directions.

The solid, red line in the main plot shows the same data rotationally averaged around the center of the Gaussian. The dashed, blue line is an Airy profile fitted to the data. The Airy radius of the fit is $0.70 \mu\text{m}$.

In a next step the averaged subpixel data are rotationally averaged around the center of the Gaussian fit. The profile of an Airy disk is fitted to the data. An example is shown in Fig. 4.16. Determining the radial scaling of all nine fits the Airy radius is $r_{\text{Airy,R}} = 0.72^{+0.02}_{-0.03} \mu\text{m}$, confirming $r_{\text{Airy,G}}$. The error of the Airy radius again combines the error of the magnification, the finite extent of the nanoparticles, the discrete subpixel size, the error of the individual fits and the statistical error over those fits. Both, $r_{\text{Airy,G}}$ and $r_{\text{Airy,R}}$ are close to the expected resolution, which is $r_{\text{Airy}} = 0.67(3) \mu\text{m}$. The error here is due to an uncertainty in the aperture stop. The discrepancy between the expected, ideal value and the measured value could either be due to the performance of the objective, or to a misjudged effect of the finite dimensions of the nanoparticles, e.g. an effect of the BPEI coat. If desired, this could be resolved by remeasuring the PSF with smaller particles.

There are also single images which, by themselves, give better Airy radii than the average value. The fits shown in Fig. 4.16 for example result in $r_{\text{Airy}} = 0.70^{+0.01}_{-0.02} \mu\text{m}$.

To determine the contrast as a function of spatial frequency, the MTF can be determined by Fourier transforming the averaged subpixel data, using a two-dimensional FFT. This was for example done for the data shown in Fig. 4.16. The inset of Fig. 4.17 shows the absolute value of the FFT in form of a contour plot. The axes correspond to spatial frequencies along the transversal directions of the CCD, i.e. the directions parallel to the rows and columns of pixels. Cross sections of the FFT along these transverse directions are plotted in the main figure as solid blue lines. The average of both lines is shown in red. For comparison the ideal MTF of Fig. 4.7 is also shown.

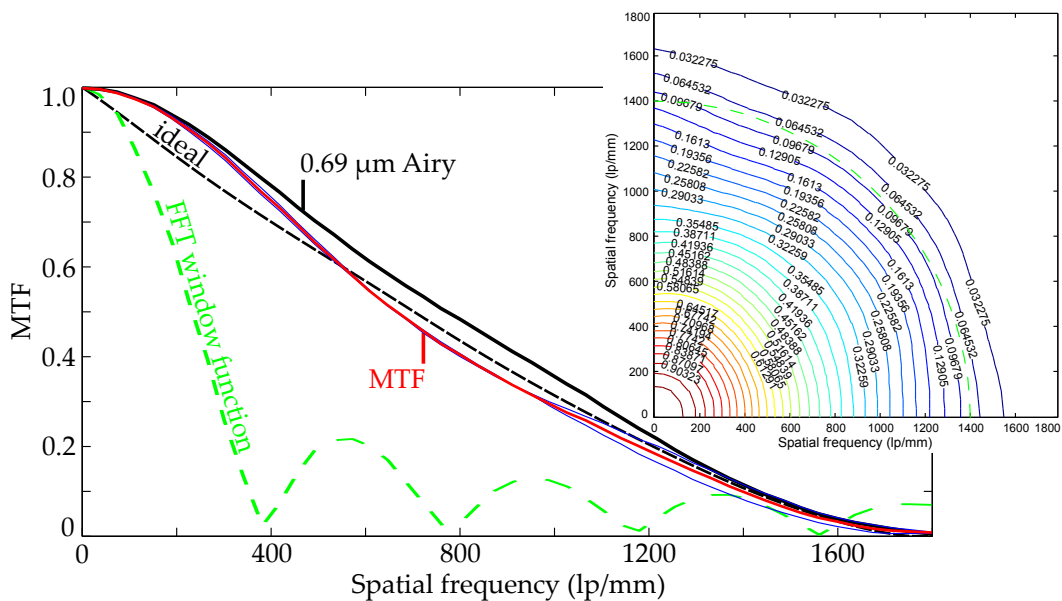


Figure 4.17: Measured MTF compared to the ideal MTF. The inset shows the absolute value of a two-dimensional FFT of the data shown in Fig. 4.16. This FFT is limited by a finite window function of $16 \times 16 \text{ px}^2$ corresponding to $2.6 \times 2.6 \mu\text{m}^2$ in the object plane. Thus the FFT is a convolution of the transfer function and the FFT of the window function.

In the main plot a cross section of the absolute value of the window function's FFT is shown as dashed green line. The thin blue lines are values of the function shown in the inset along the x- and y-axes. The red solid line is the average of the blue lines. The MTF of the ideal system taken from Fig. 4.7 (black dashed line) visualizes the finite size effects. The black solid line is the absolute value of the FFT of an Airy disk with radius $0.69 \mu\text{m}$, computed in the same window as the FFT of the experimental data.

Clearly, the FFT of the experimental data overestimates the contrast at low spatial frequencies. These finite size effects are due to the finite window function of the FFT. As the FFTs were taken over a finite window of $16 \times 16 \text{ px}^2$, corresponding to $2.6 \times 2.6 \mu\text{m}^2$ in the object plane, the FFT is a convolution of the transfer function and the FFT of the window function. The absolute value of the window function's FFT is shown as a dashed green line. It goes to zero at about $390 \frac{\text{lp}}{\text{mm}}$. Before computing the FFT, the background had to be subtracted from the data. A good estimate of the background is provided by the vertical offset determined during the radial fit of the Airy profile.

To circumvent the problem of deconvolution, the absolute value of the FFT of an Airy disk with $0.69 \mu\text{m}$ radius, computed in the same window, is shown as a solid black line. The Airy radius of $0.69 \mu\text{m}$ corresponds to the numerical aperture of 0.52 which was desired in the design. Compared to the solid black line, the measured ‘MTF’ sags at medium frequencies, indicating non-optimal performance. The sag is however less significant than for the aberrations shown in Fig. 4.7. This could be confirmed by the Strehl ratio. The ratio of the volume below the absolute value of the two-dimensional FFT of the data and the volume below the absolute value of the FFT of an Airy disk with $0.69 \mu\text{m}$ radius is 0.87.¹² Because of the window effects in the FFT, and the finite pixel size this ratio does not exactly resemble the Strehl ratio of the objective. This can, however, be considered to be a common artifact [204].

To check the evaluation process a relatively bad image was evaluated. The results are shown in Appendix A.6.

4.7 Conclusion

This chapter presented the design of an objective with potential single-site resolution, which enables probing the microscopic density distribution of atoms in quasi two-dimensional lattice systems. A measurement of the PSF confirmed a resolution comparable to an Airy radius of $0.71_{-0.03}^{+0.02} \mu\text{m}$, or better. This is close to the desired value of $r_{\text{Airy}} = 0.69 \mu\text{m}$. The ratio of the volumes below the absolute values of the FFT of the PSF and of the FFT of an Airy disk with $0.69 \mu\text{m}$ radius is 0.87.

Determining the PSF with gold nanoparticles proved to be comparatively cheap. It would however be advantageous to use a substrate with large features of a well known size (about $10 \cdot r_{\text{Airy}}$ to $100 \cdot r_{\text{Airy}}$) to determine the PSF and the magnification in a single image.

In total, the costs of the objective, including an anti-reflection coating of the lenses are around € 10 000. When building two objectives the costs could be reduced by about 30%.

Future designs could be even more versatile and provide a larger numerical aperture, aiming for a higher numerical aperture at an imaging wavelength of 589 nm. Considering the cutoff frequency of the MTF, real single-site resolution of atoms in an optical lattice with 532 nm spacing is already achievable at a numerical aperture of 0.56. A value which can be implemented in a refined two lens design.

¹² The finite window function of the FFT is certainly limiting the accuracy, here. However, considering the footnote to Eq. (4.10), which notes: $\text{Strehl} = \frac{\iint \text{OTF}_{\text{RealSystem}} df_x df_y}{\iint \text{OTF}_{\text{IdealSystem}} df_x df_y}$, the situation is different.

Starting from Eq. (4.9): $\text{Strehl} =$

$$\begin{aligned} \frac{\text{PSF}_{\text{RealSystem}}(0)}{\text{PSF}_{\text{IdealSystem}}(0)} &= \frac{\text{PSF}_{\text{RealSystem}}(0) \cdot W(0)}{\text{PSF}_{\text{IdealSystem}}(0) \cdot W(0)} = \frac{\text{PSF}_{\text{RealSystem}}(x,y) \cdot W(x,y)}{\text{PSF}_{\text{IdealSystem}}(x,y) \cdot W(x,y)} \Bigg|_{x,y=0} = \frac{\mathcal{F}^{-1}[\text{OTF}_{\text{RealSystem}}(x,y)] \cdot \mathcal{F}^{-1}[\hat{W}(x,y)]}{\mathcal{F}^{-1}[\text{OTF}_{\text{IdealSystem}}(x,y)] \cdot \mathcal{F}^{-1}[\hat{W}(x,y)]} \Bigg|_{x,y=0} = \\ &= \frac{\mathcal{F}^{-1}[\text{OTF}_{\text{RealSystem}}(x,y) \circ \hat{W}(x,y)]}{\mathcal{F}^{-1}[\text{OTF}_{\text{IdealSystem}}(x,y) \circ \hat{W}(x,y)]} \Bigg|_{x,y=0} = \frac{\mathcal{F}^{-1}[\mathcal{F}[\text{PSF}_{\text{RealSystem}}(x,y)] \circ \mathcal{F}[W(x,y)]]}{\mathcal{F}^{-1}[\mathcal{F}[\text{PSF}_{\text{IdealSystem}}(x,y)] \circ \mathcal{F}[W(x,y)]]} \Bigg|_{x,y=0} = \frac{\mathcal{F}^{-1} \mathcal{F}[\text{PSF}_{\text{RealSystem}}(x,y) \cdot W(x,y)]}{\mathcal{F}^{-1} \mathcal{F}[\text{PSF}_{\text{IdealSystem}}(x,y) \cdot W(x,y)]} \Bigg|_{x,y=0} \\ &= \left\{ \frac{\mathcal{F}^{-1}[\text{OTF}_{\text{RealSystem,FFT}}(f_x, f_y)]}{\mathcal{F}^{-1}[\text{OTF}_{\text{IdealSystem,FFT}}(f_x, f_y)]} \Bigg|_{x,y=0} = \frac{\iint \text{OTF}_{\text{RealSystem,FFT}} df_x df_y}{\iint \text{OTF}_{\text{IdealSystem,FFT}} df_x df_y} \right\} = \frac{[\text{PSF}_{\text{RealSystem}}(x,y) \cdot W(x,y)]}{[\text{PSF}_{\text{IdealSystem}}(x,y) \cdot W(x,y)]} \Bigg|_{x,y=0} = \frac{\text{PSF}_{\text{RealSystem,FFT}}(0)}{\text{PSF}_{\text{IdealSystem,FFT}}(0)}, \end{aligned}$$

with $W(x,y)$ being the window function of the FFT and ‘ \circ ’ denoting convolution.

The last ratio in curly brackets also evaluates to 0.87, however.

CHAPTER 5

Outlook

In this thesis I presented the necessary tools to create ultracold gases of polar NaK ground state molecules, as we have implemented them in our experiment. Furthermore I introduced an electrode geometry, suitable to polarize these molecules, tune their dipolar interaction and address their rotational states in single layers of a one-dimensional optical lattice. In the last section I presented the design and characterization of a diffraction limited, high resolution objective, applicable to image sodium at the D2 line with single-site resolution in an optical lattice with 532 nm spacing.

At the current point, the vacuum in the main chamber is unfortunately limiting the experiment. The vacuum limits the lifetime of magnetically trapped samples to values at which evaporative cooling to the quantum regime appears to be extremely challenging. Nevertheless, dipolar interactions in quantum-many-body systems are an important topic in the context of ultracold gases and most theoretical proposals have not been tested in experiments, yet. Therefore, it is important to overcome the current limitations, in order to create a sample of ultracold polar NaK molecules. In this context a new main vacuum chamber was implemented which overcomes the limitations of the old one.

In the following I will shortly summarize the main points of each chapter and indicate how further work can extend it.

5.1 Setup

Most required components of the experiment are already set up. Until now the progress was solely limited by a decrease of the lifetime in the magnetic trap over the period of several months. Lifetimes as short as 4 s inhibited evaporative cooling in the magnetic trap and consequently the creation of ultracold samples.

The decrease of the measured lifetime was attributed to a deteriorating vacuum at the location of the atoms. An investigation required several bakings of the main vacuum chamber and many of the components in and on the chamber had to be exchanged.

Since the beginning of November 2015 a new vacuum chamber has replaced the old one. In the new chamber the lifetime was measured to be 37(2) s in the unplugged magnetic trap. This value has been constant over the last two weeks. The controllers of the ion pump on the main chamber and the small ion pump at the end of the Zeeman slower pipe show 6.5 nA and 0.3 nA, respectively. Both currents correspond to pressures below $1 \cdot 10^{-11}$ mbar. Currently, all components of the experiment are optimized, for an efficient evaporative cooling, enabling experiments in the quantum degenerate regime.

5.2 Electric Fields

For tuning the dipolar interactions of polar molecules, this experiment relies on electric DC fields. Hence, the dipolar interactions are tuned by changing the direction and magnitude of the electric field at the location of the molecules. It was found that spatial deviations of the field magnitude must be minimized, to reduce the field's influence on the molecules' confinement.

An electrode geometry was devised which can be used to create the required electric fields: In the volume of the optical dipole trap the electric field can reach about

10 kV/cm with relative spatial deviations below 10^{-6} . Its direction is fully rotatable in a plane spanned by the vertical and a horizontal axis of the optical lattice. This means NaK ground state molecules could be polarized up to 1.9 D, while their interactions in low dimensional geometries can be tuned from repulsive to attractive. For addressing the molecules' rotational states in single layers of a one-dimensional optical lattice electric field gradients as high as 3 kV/cm² can be applied. Such versatile fields are suitable for mapping out phase diagrams of dipolar interactions.

The idea of mutually canceling gradients or curvatures of the electric field, created by several electrodes, is also applicable to smaller sized electrode geometries, with $w_0/l \approx 1$, like they can be implemented on atom-chips. As chips can be manufactured in various layouts and with high accuracy, an excellent predictability of the created electric fields can be expected. Due to the small length scales, the required electric potentials [205] will be smaller by more than one order of magnitude compared to macroscopic systems. This simplifies the implementation of electronics for switching and ramping electric fields. An electrode structure with three pairs of rods in a horizontal plane was optimized regarding relative magnitude deviations of vertical electric fields. Another structure was optimized for horizontal fields. Both results are shown in Fig. 5.1.

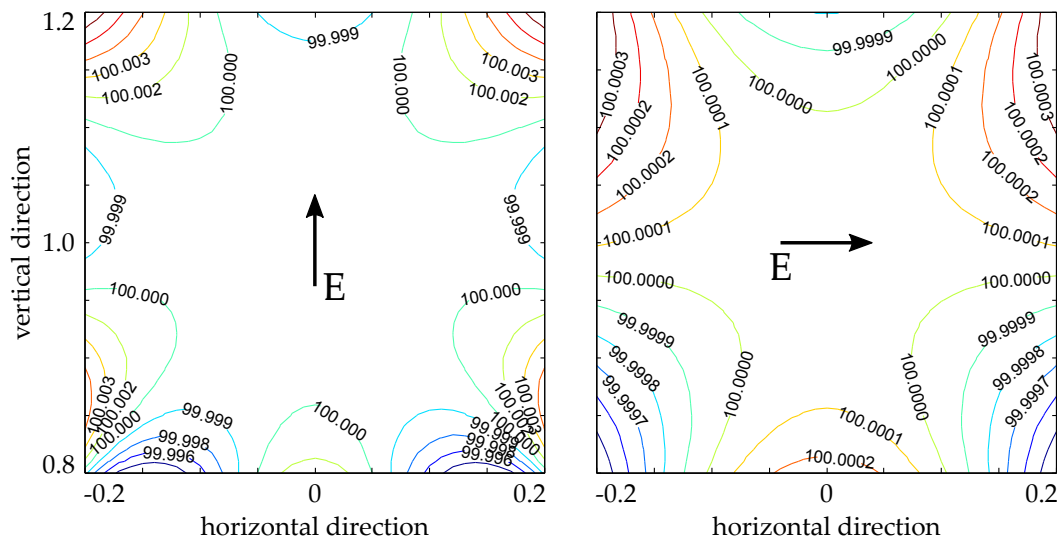


Figure 5.1: Electric field magnitude of rods in chip like configuration. Contour plot of electric field magnitudes created by six infinitely long, parallel, mirror symmetric rods in the horizontal x - y -plane. The rods extend in the y direction. The plot shows the electric field magnitude in the x - z -plane. The electric field magnitude was normalized to a value of 100 at the center of the contour plot. All length scales are relative. The center of the coordinate system is 1 above the symmetry axis of the rods. The black arrows indicate the direction of the electric field. The geometric optimization for the vertical and horizontal field directions was independent.

Considering a volume with 100 μm radial extend, centered 500 μm above the plane the relative deviations are in both cases on the order of 10^{-5} . More uniform fields are obtained when increasing the spatial dimensions of the geometry whilst maintaining the radial extend of the trapping volume. These first results suggest that atom chips could be another excellent environment to implement experiments with polar molecules.

5.3 Objective

In the last chapter it was shown that high resolution imaging is also possible with relatively simple optical systems. It was experimentally verified that based on an objective consisting of only two lenses diffraction limited imaging with a resolution corresponding to an Airy radius of $0.71^{+0.02}_{-0.03}$ μm can be achieved. The imaging wavelength was 589 nm, the working distance about 22 mm. The field of view was geometrically limited to $220 \times 170 \mu\text{m}^2$ by the chip size of the camera.

Simulations predict that the objective can be diffraction limited at any imaging wavelength between 400 nm and 1100 nm. By adapting future designs also to thinner vacuum windows, the objective could become even more adaptable to different experiments. For convenience, the three point mount of the objective can be modified to have two perpendicular rotation axes, while substituting the currently used open loop picomotors by closed loop versions (e.g. LPMS, NANOS-Instruments GmbH) which promise a higher reproducibility at similar costs.

The obtained results encourage to attempt the design of similar systems with higher numerical apertures. For a lattice constant of 532 nm, a numerical aperture of 0.56 combined with an imaging wavelength of 589 nm would provide actual single site resolution¹. Higher numerical apertures will also mitigate the negative effects of the gapped indium tin oxide coating on the modulation transfer function.

Combining all necessary tools for the production of ultracold NaK molecules, the electric fields to polarize them and high resolution imaging, this experiment will be an excellent test ground to study strong dipolar interactions in the quantum regime and test the formation of phases like supersolids in defect free lattices.

¹ At an numerical aperture above 0.60 the cutoff frequency exceeds $2000 \frac{\text{lp}}{\text{mm}}$.

APPENDIX A

Appendix

A.1 Constants

| Constant | Value | Unit | |
|--------------|--------------------------------|------------------|-----------------------------|
| a_0 | $0.52917721067 \cdot 10^{-10}$ | m | Bohr radius |
| c | $2.99792458 \cdot 10^8$ | m/s | Speed of light in vacuum |
| μ_0 | $4\pi \cdot 10^{-7}$ | N/A ² | Magnetic constant |
| ϵ_0 | $8.854187817 \cdot 10^{-12}$ | F/m | Electric constant |
| \hbar | $1.054571800 \cdot 10^{-34}$ | Js | Planck constant over 2π |
| k_B | $1.38064852 \cdot 10^{-23}$ | J/K | Boltzmann constant |
| μ_B | $9.274009994 \cdot 10^{-24}$ | J/T | Bohr magneton |

Table A.1: Table of constants. Values: <http://physics.nist.gov/cuu/Constants/index.html>; 30th of November, 2015

A.2 Laboratory Conditions

After initial problems with the air conditioning and the flow-boxes, the system was fixed by many efforts from Christian Ospelkaus. Now, as Fig. A.1 shows, it appears to work mostly unproblematic.

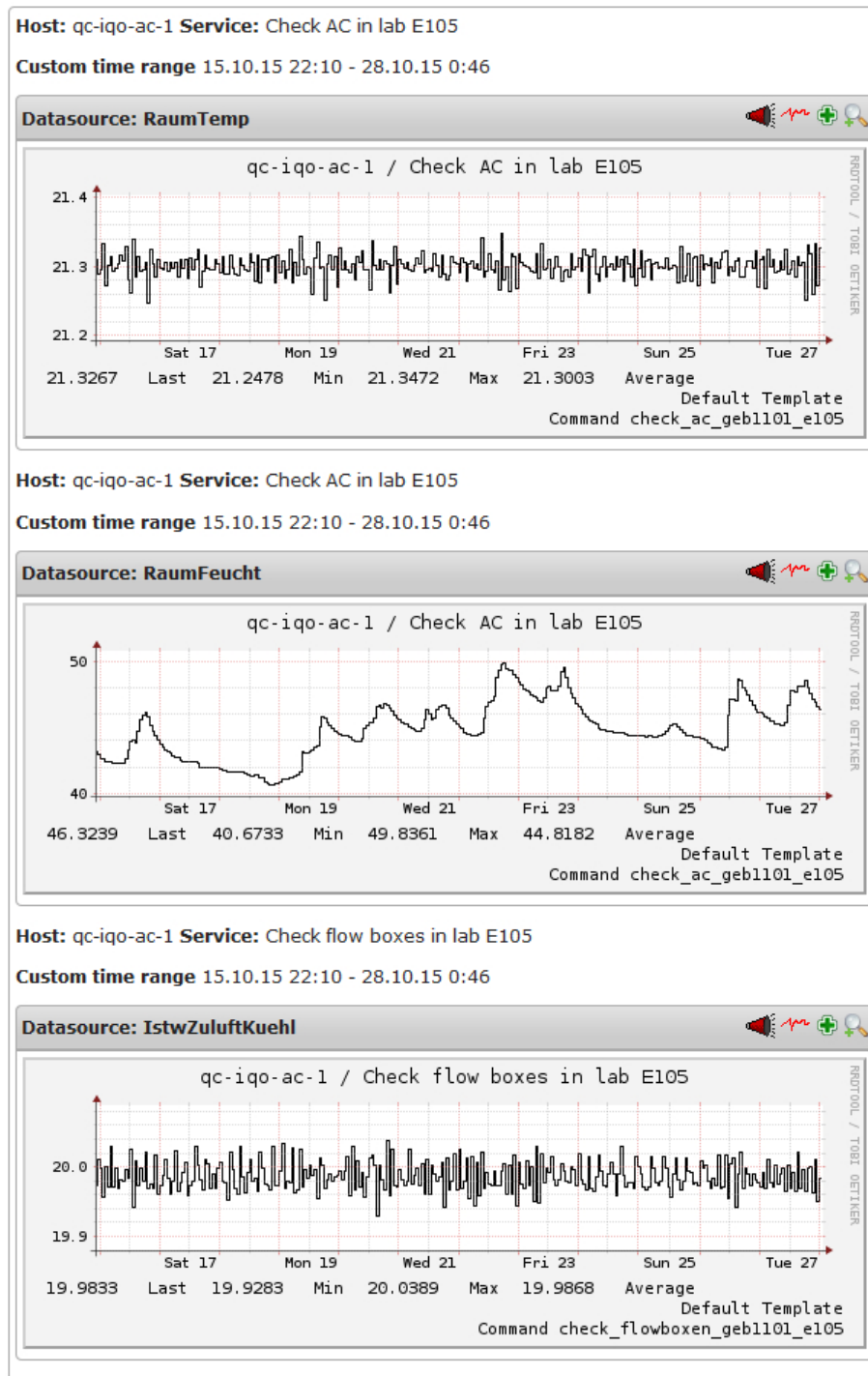


Figure A.1: Laboratory conditions. Values of room temperature, humidity and temperature of the flow-boxes over time period of twelve days. The peak to peak deviation in room temperature was 0.1°C . The peak to peak deviation in humidity was 10%. The peak to peak deviation in flow box temperature was 0.1°C .

A.3 Offset Lock

The offset lock frequency stabilizes two lasers with respect to another by beating them on a fast photo diode. The beat signal is electronically processed as show in Fig. A.2: First, it is amplified, then split to show the frequency of the beat, i.e. the frequency difference of both lasers, on a frequency counter. To further process the signal it is frequency down converted by mixing it with a stable local oscillator. The down converted signal is amplified, power limited, filtered and sent to the error signal circuit.

The error signal circuit [206], shown in Appendix A.3, converts the frequency difference between the down converted signal and the 3 dB point of a high pass filter (RHP-65, Mini Circuits) to a DC signal, which can be processed by a PID controller and fed back to one of the lasers to stabilize its frequency.

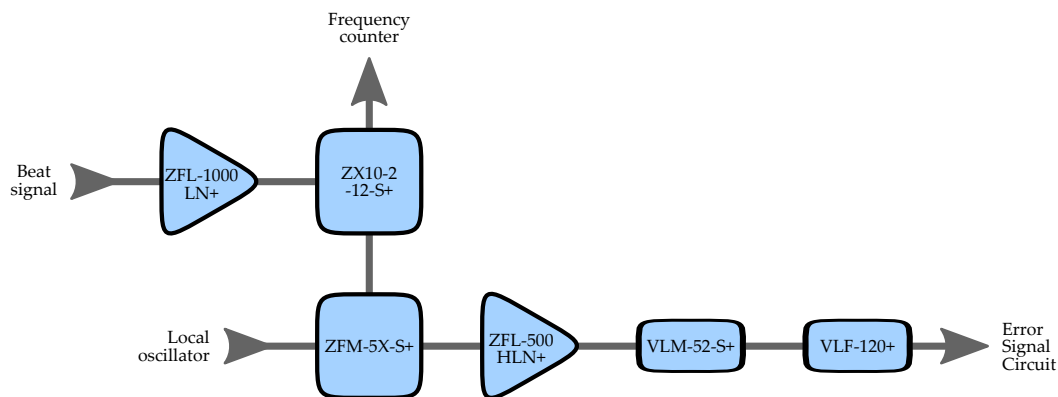


Figure A.2: The beat signal of the photo diode is fed to this circuit. It is amplified and split. One part is send to a frequency counter, the other is frequency down converted. The down converted signal is amplified, power limited and low pass filtered, before it is converted to an error signal

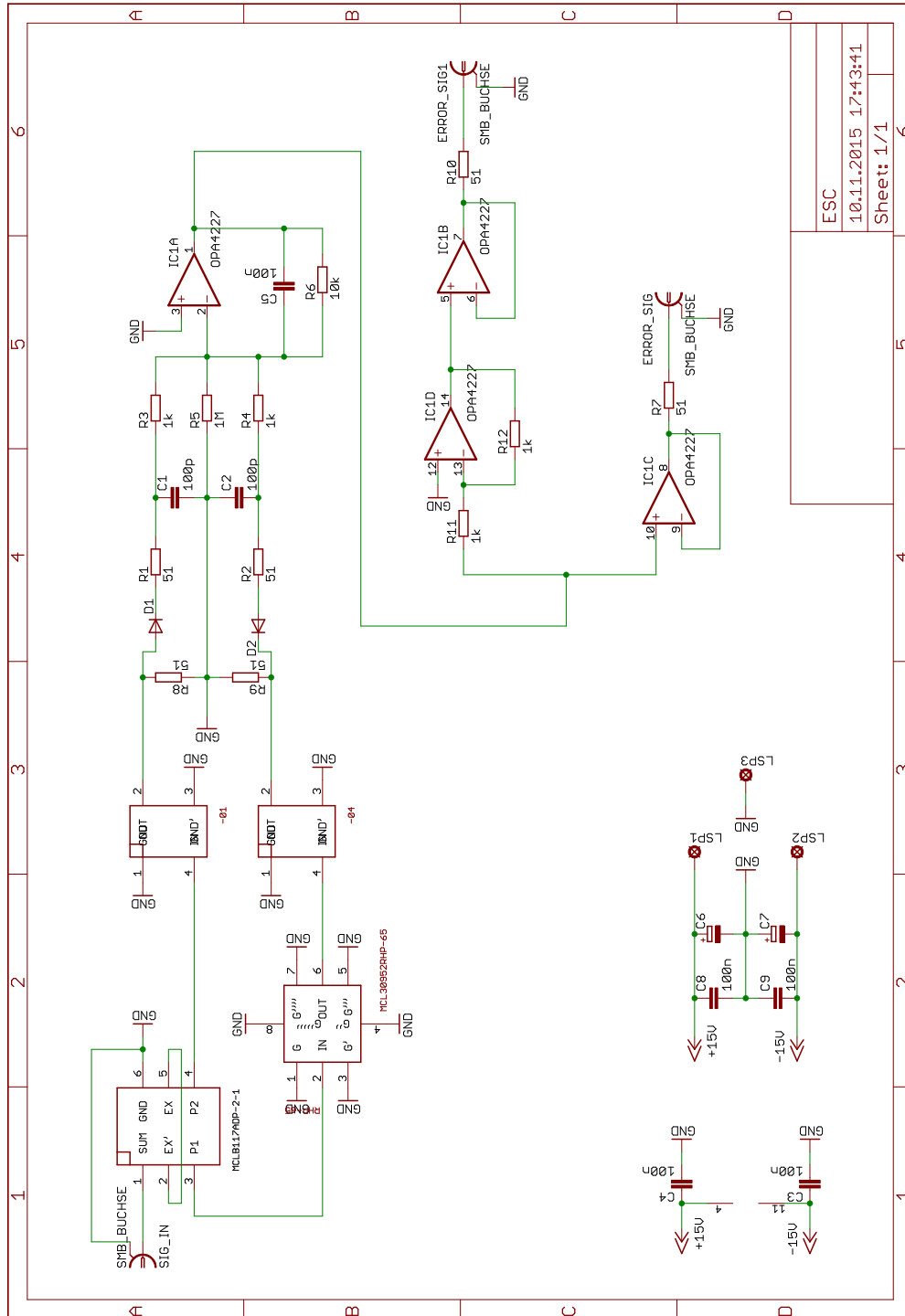


Figure A.3: The error signal circuit is based on [206].

A.4 Coil Control

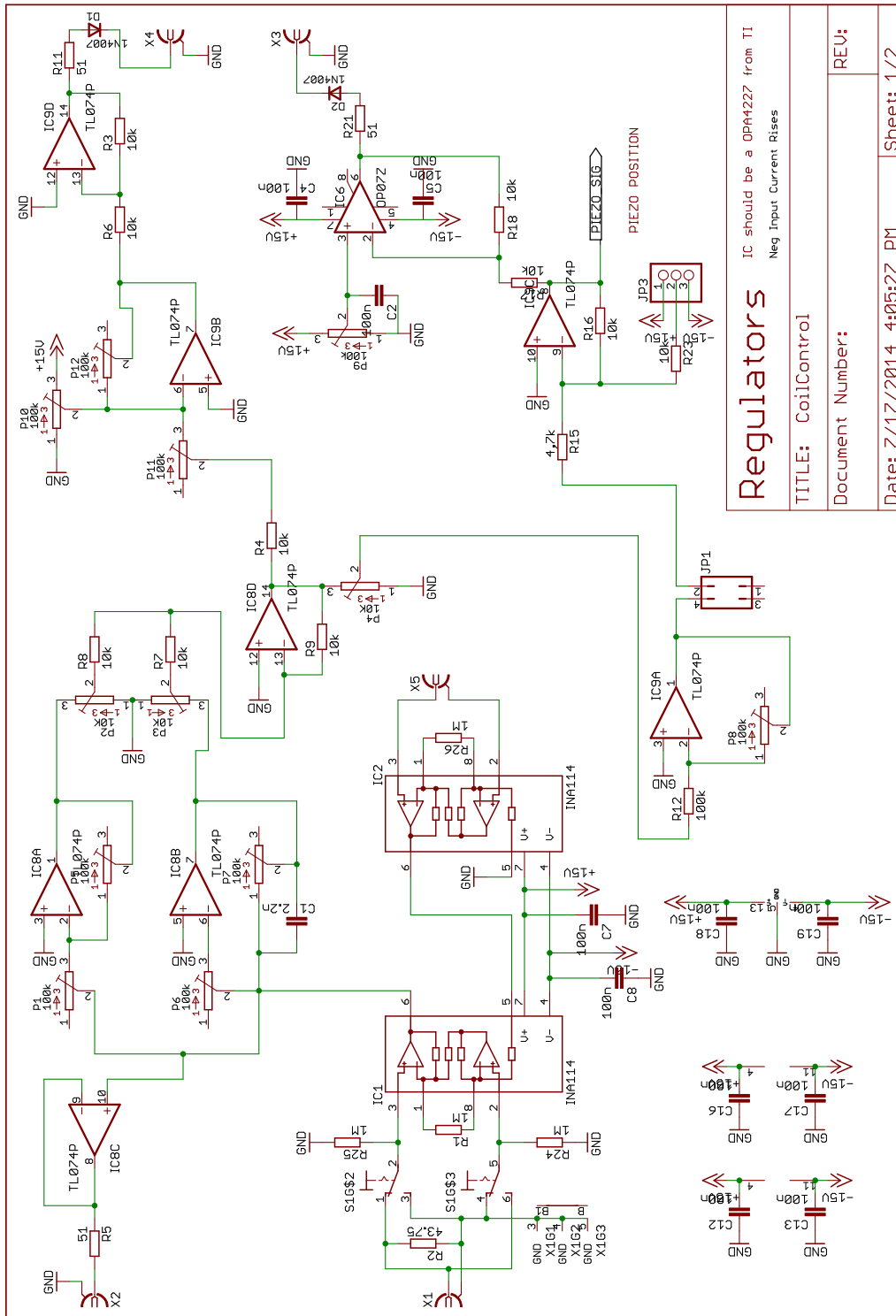


Figure A.4: The proportional-integral control for the coil control is a variation of the proportional-integral control for laser locking.

A.5 Electrodes

Table A.2 lists the layers of the anti-reflection and ITO coating of the CF200 vacuum windows.

| | | | | | | |
|-------------------|--------------------------------|------------------|--------------------------------|------------------|--------------------------------|------------------|
| Material: | Gold | Titan | ITO | SiO ₂ | Ta ₂ O ₅ | SiO ₂ |
| Thickness: | 200nm | 50nm | 167nm | 141,71nm | 36,67nm | 55,12nm |
| | Ta ₂ O ₅ | SiO ₂ | Ta ₂ O ₅ | SiO ₂ | Ta ₂ O ₅ | SiO ₂ |
| | 39,78nm | 306,83nm | 20,00nm | 32,07nm | 89,49nm | 54,23nm |
| | Ta ₂ O ₅ | SiO ₂ | Ta ₂ O ₅ | SiO ₂ | Ta ₂ O ₅ | SiO ₂ |
| | 20,00nm | 258,41nm | 41,24nm | 39,60nm | 70,11nm | 31,11nm |
| | Ta ₂ O ₅ | SiO ₂ | Ta ₂ O ₅ | Quarzglas | Ta ₂ O ₅ | SiO ₂ |
| | 35,84nm | 100,00nm | 150,00nm | - | 150,00nm | 100,00nm |
| | Ta ₂ O ₅ | SiO ₂ | Ta ₂ O ₅ | SiO ₂ | Ta ₂ O ₅ | SiO ₂ |
| | 29,07nm | 50,64nm | 55,61nm | 56,94nm | 38,57nm | 293,41nm |
| | Ta ₂ O ₅ | SiO ₂ | Ta ₂ O ₅ | SiO ₂ | Ta ₂ O ₅ | SiO ₂ |
| | 23,84nm | 58,27nm | 114,43nm | 43,34nm | 20,95nm | 310,42nm |
| | Ta ₂ O ₅ | SiO ₂ | Ta ₂ O ₅ | SiO ₂ | | |
| | 41,49nm | 64,07nm | 36,38nm | 151,89nm | | |

Table A.2: Layers of coating on main windows. The material and thickness of each layer of the coating is listed, starting from the vacuum side. Masks were used, to create the gold, titan and ITO structures. Data are provided by the Fraunhofer IST, Braunschweig.

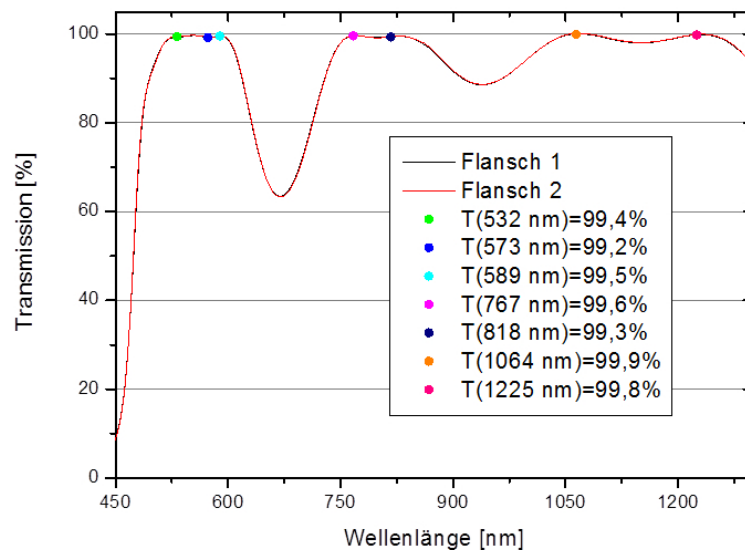


Figure A.5: Measured transmission of anti-reflection coating. The curve shown is the transmission of one window, without ITO. The transmission was optimized for the wavelength 532 nm, 573 nm (STIRAP), 589 nm (sodium), 767 nm (potassium), 818 nm (STIRAP), 1064 nm (optical lattice) and 1225 nm. Data are provided by the Fraunhofer IST, Braunschweig.

As shown in Fig. A.5, the anti-reflection coating was optimized for 532 nm, 573 nm, 589 nm, 767 nm, 818 nm, 1064 nm and 1225 nm, i.e. some wavelength typical for ultracold atom experiments, the sodium and potassium D2 line, the STIRAP lasers, as well as the optical dipole trap and lattice. The ITO and gold structures were sputtered on the window by means of a negative metallic mask.

Figure A.6 indicates a high transmission of ITO for wavelength in the visible regime. The results of simulations shown in Figs. A.7 and A.8 indicate that in combination with the anti-reflection coating a 166.7 nm thick ITO layer provides high transmission at the sodium and the potassium D2 lines (589 nm and 767 nm).

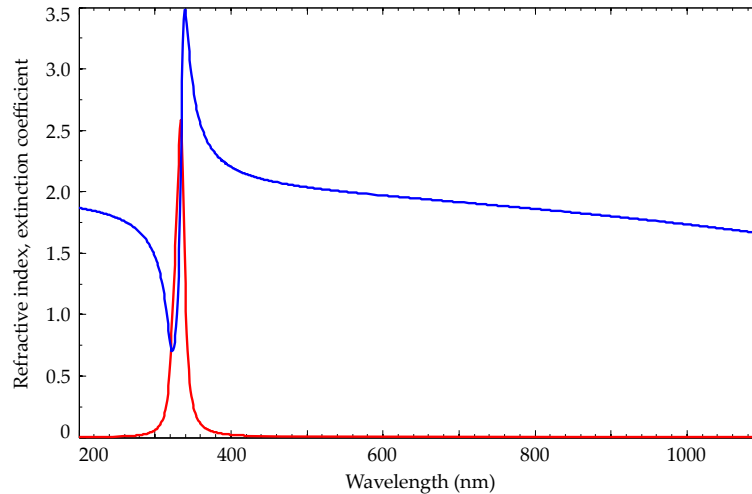


Figure A.6: Dispersion data of ITO. Blue: refractive index n . Red: extinction coefficient k . Data are provided by the Fraunhofer IST, Braunschweig.

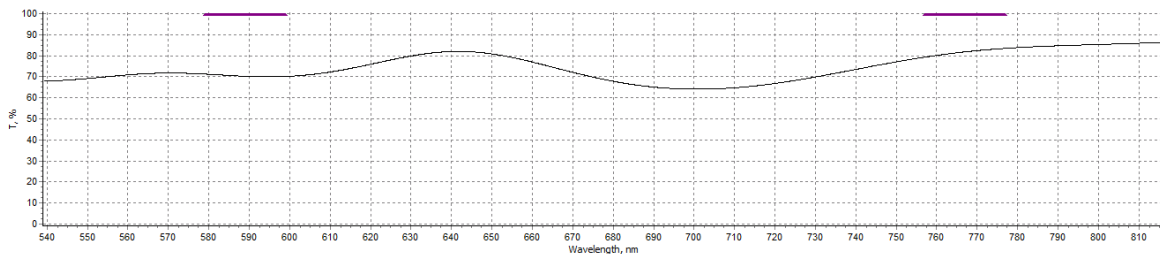


Figure A.7: Calculated Transmission AR + 50 nm ITO. Data are provided by the Fraunhofer IST, Braunschweig.

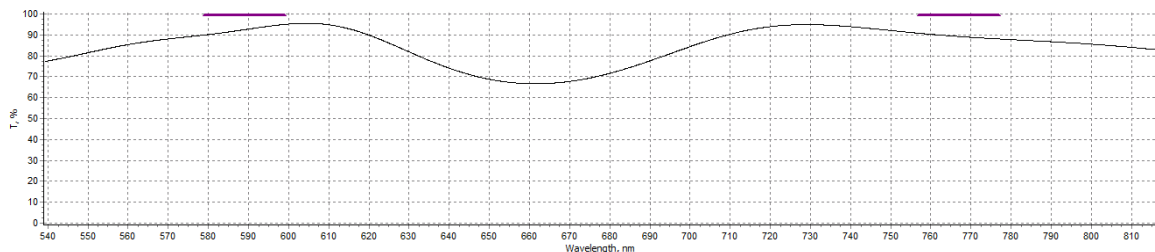


Figure A.8: Calculated Transmission AR + 166.7 nm ITO. Data are provided by the Fraunhofer IST, Braunschweig.

A.6 Objective

A.6.1 Non Ideal Imaging

The following figures give a short impression of results for non ideal nanoparticle images. Figure A.9 shows the rotational average over 19 gold nanoparticle images. Figure A.10 shows cross sections of the FFT of an average of the same gold nanoparticle images.

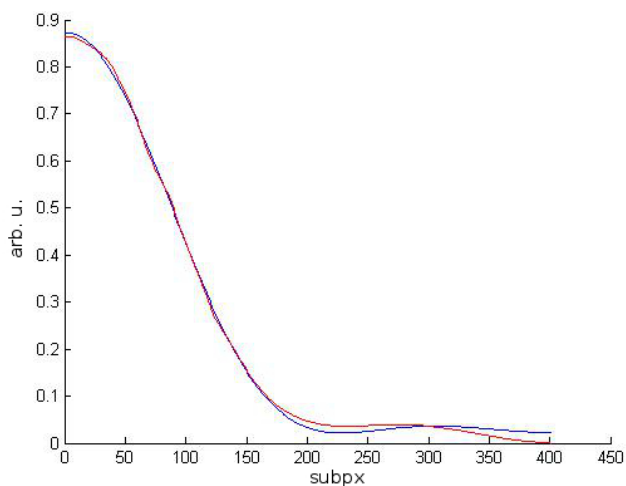


Figure A.9: Rotational average over an average of 19 gold nanoparticle images. Red solid curve: Data. Blue solid curve: Fit of Airy profile. X-Axis: subpixel. Y-axis: arbitrary units.

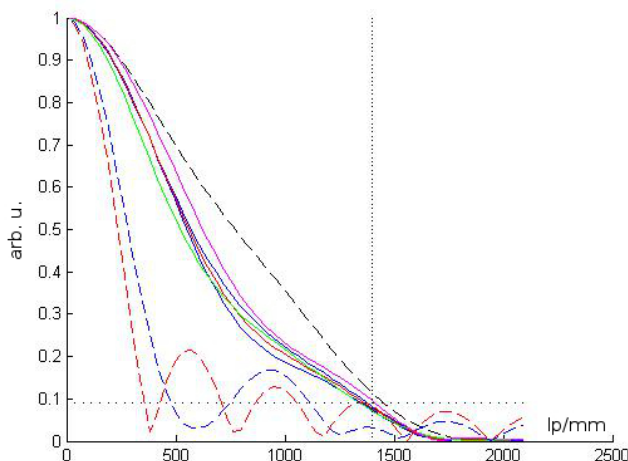


Figure A.10: Cross sections of the FFT of an average of 19 gold nanoparticle images. The interesting lines are: Black dashed: FFT of Airy disk with $0.69 \mu\text{m}$ radius. Blue solid: Cross sections of FFT of images of nanoparticles, in x and y direction. Red solid: Average of blue lines Green solid: Less background subtraction. Magenta solid: Higher background subtraction. X-Axis: spatial frequency in lp/mm. Y-axis: contrast.

A.6.2 Zemax

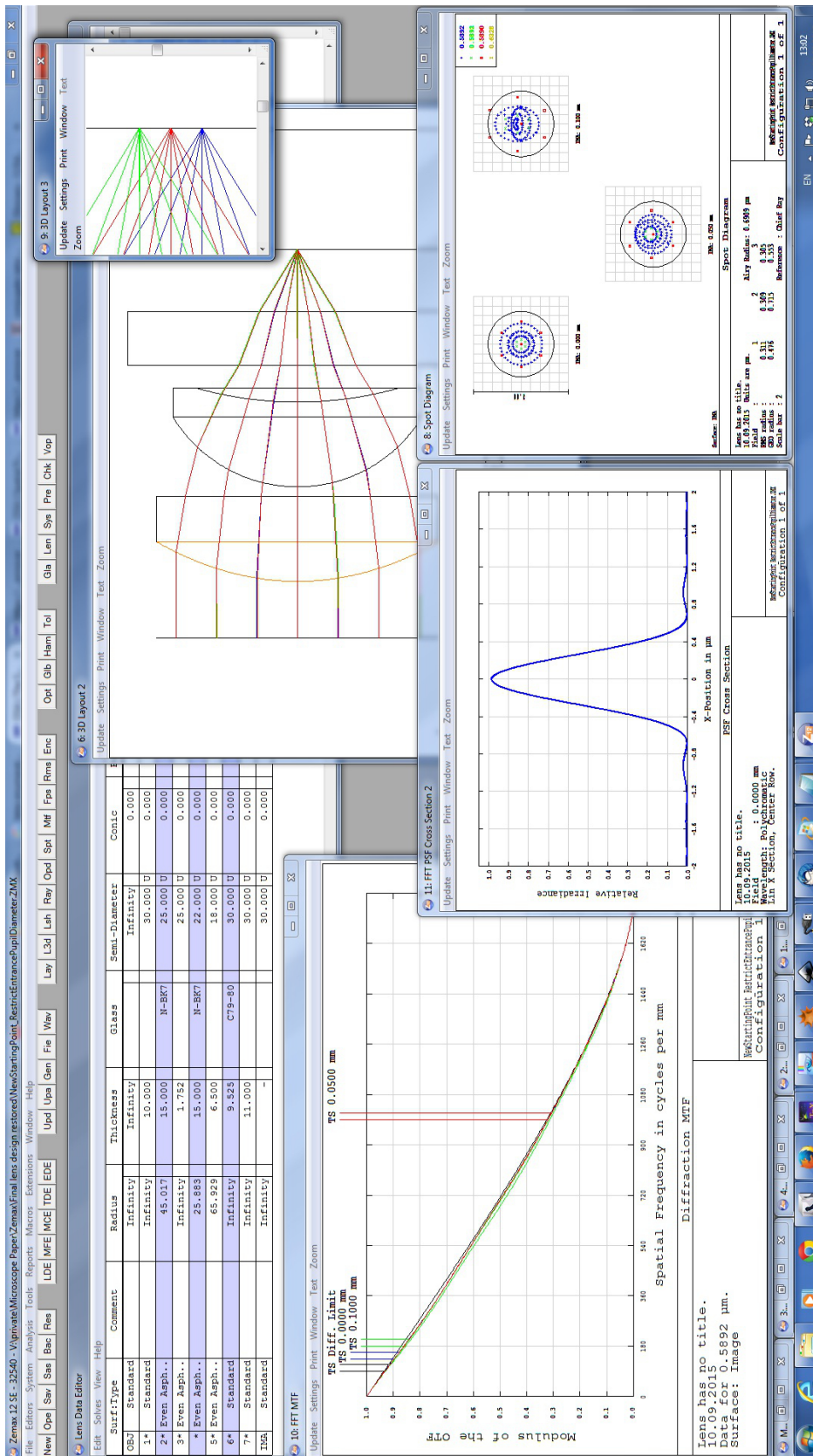


Figure A.11: Zemax screen shot. This screen shot shows the layout of Zemax, with the lens data editor in the upper left corner, MTF cross sections in the lower left corner. In the upper right corner one finds a cross section of the objective layout with a zoom in on the image plane one the three different fields which were optimized. In the lower right corner is a spot diagram showing some rays which are geometrically traced through the system and the Airy radius of the system as a black circle. In the middle is a cross section of the PSF.

Bibliography

- [1] M. H. Anderson, J. R. Ensher, M. R. Matthews, C. E. Wieman, and E. A. Cornell. Observation of Bose-Einstein condensation in a dilute atomic vapor. *Science*, 269:198, 1995.
- [2] K. B. Davis, M. O. Mewes, M. R. Andrews, N. J. van Druten, D. S. Durfee, D. M. Kurn, and W. Ketterle. Bose-Einstein condensation in a gas of sodium atoms. *Phys. Rev. Lett.*, 75:3969, 1995.
- [3] B. DeMarco and D. S. Jin. Onset of Fermi degeneracy in a trapped atomic gas. *Science*, 285:1703, 1999.
- [4] C. A. Regal, C. Ticknor, J. L. Bohn, and D. S. Jin. Creation of ultracold molecules from a Fermi gas of atoms. *Nature*, 424:47, 2003.
- [5] M. Greiner, O. Mandel, T. Esslinger, T. W. Hänsch, and I. Bloch. Quantum phase transition from a superfluid to a Mott insulator in a gas of ultracold atoms. *Nature*, 415:39, 2002.
- [6] M. P. A. Fisher, P. B. Weichman, G. Grinstein, and D. S. Fisher. Boson localization and the superfluid-insulator transition. *Phys. Rev. B*, 40:546, 1989.
- [7] I. Bloch. Ultracold quantum gases in optical lattices. *Nat. Phys.*, 1:23, 2005.
- [8] R. P. Feynman. Simulating physics with computers. *Int. J. Theor. Phys.*, 21:467, 1982.
- [9] I. Bloch, J. Dalibard, and W. Zwerger. Many-body physics with ultracold gases. *Rev. Mod. Phys.*, 80:885, 2008.
- [10] M. Lewenstein, A. Sanpera, and V. Ahufinger. *Ultracold atoms in optical lattices: simulating quantum many-body systems*. OUP Oxford, 2012.
- [11] D. Mukamel, S. Ruffo, and N. Schreiber. Breaking of ergodicity and long relaxation times in systems with long-range interactions. *Phys. Rev. Lett.*, 95:240604, 2005.
- [12] J. Barré, D. Mukamel, and S. Ruffo. Inequivalence of ensembles in a system with long-range interactions. *Phys. Rev. Lett.*, 87:030601, 2001.
- [13] S. Trotzky, P. Cheinet, S. Fölling, M. Feld, U. Schnorrberger, A. M. Rey, A. Polkovnikov, E. A. Demler, M. D. Lukin, and I. Bloch. Time-resolved observation and control of superexchange interactions with ultracold atoms in optical lattices. *Science*, 319:295, 2008.
- [14] J. L. Bohn, M. Cavagnero, and C. Ticknor. Quasi-universal dipolar scattering in cold and ultracold gases. *New J. Phys.*, 11:055039, 2009.

- [15] M. Vengalattore, S. R. Leslie, J. Guzman, and D. M. Stamper-Kurn. Spontaneously modulated spin textures in a dipolar spinor Bose-Einstein condensate. *Phys. Rev. Lett.*, 100:170403, 2008.
- [16] J. Stuhler, A. Griesmaier, T. Koch, M. Fattori, T. Pfau, S. Giovanazzi, P. Pedri, and L. Santos. Observation of dipole-dipole interaction in a degenerate quantum gas. *Phys. Rev. Lett.*, 95:150406, 2005.
- [17] K. Aikawa, A. Frisch, M. Mark, S. Baier, A. Rietzler, R. Grimm, and F. Ferlaino. Bose-Einstein condensation of erbium. *Phys. Rev. Lett.*, 108:210401, 2012.
- [18] M. Lu, N. Q. Burdick, S. H. Youn, and B. L. Lev. Strongly dipolar Bose-Einstein condensate of dysprosium. *Phys. Rev. Lett.*, 107:190401, 2011.
- [19] M. Aymar and O. Dulieu. Calculation of accurate permanent dipole moments of the lowest $1,3\Sigma^+$ states of heteronuclear alkali dimers using extended basis sets. *J. Chem. Phys.*, 122:204302, 2005.
- [20] T. Lahaye, T. Koch, B. Fröhlich, M. Fattori, J. Metz, A. Griesmaier, S. Giovanazzi, and T. Pfau. Strong dipolar effects in a quantum ferrofluid. *Nature*, 448:672, 2007.
- [21] T. Lahaye, J. Metz, B. Fröhlich, T. Koch, M. Meister, A. Griesmaier, T. Pfau, H. Saito, Y. Kawaguchi, and M. Ueda. d -wave collapse and explosion of a dipolar Bose-Einstein condensate. *Phys. Rev. Lett.*, 101:080401, 2008.
- [22] S. Müller, J. Billy, E. A. L. Henn, H. Kadau, A. Griesmaier, M. Jona-Lasinio, L. Santos, and T. Pfau. Stability of a dipolar Bose-Einstein condensate in a one-dimensional lattice. *Phys. Rev. A*, 84:053601, 2011.
- [23] K. Aikawa, S. Baier, A. Frisch, M. Mark, C. Ravensbergen, and F. Ferlaino. Observation of Fermi surface deformation in a dipolar quantum gas. *Science*, 345:1484, 2014.
- [24] K. Aikawa, A. Frisch, M. Mark, S. Baier, R. Grimm, J. L. Bohn, D. S. Jin, G. M. Bruun, and F. Ferlaino. Anisotropic relaxation dynamics in a dipolar Fermi gas driven out of equilibrium. *Phys. Rev. Lett.*, 113:263201, 2014.
- [25] K.-K. Ni, S. Ospelkaus, M. H. G. de Miranda, A. Pe'er, B. Neyenhuis, J. J. Zirbel, S. Kotochigova, P. S. Julienne, D. S. Jin, and J. Ye. A high phase-space-density gas of polar molecules. *Science*, 322:231, 2008.
- [26] S. Ospelkaus, K.-K. Ni, D. Wang, M. H. G. de Miranda, B. Neyenhuis, G. Quéméner, P. S. Julienne, J. L. Bohn, D. S. Jin, and J. Ye. Quantum-state controlled chemical reactions of ultracold potassium-rubidium molecules. *Science*, 327:853, 2010.
- [27] B. Yan and S. A. Moses and B. Gadway and J. P. Covey and K. R. A. Hazzard and A. M. Rey and D. S. Jin and J. Ye. Observation of dipolar spin-exchange interactions with lattice-confined polar molecules. *Nature*, 501:521, 2013.

- [28] M. A. Baranov. Theoretical progress in many-body physics with ultracold dipolar gas. *Phys. Rep.*, 464:71, 2008.
- [29] T. Lahaye, C. Menotti, L. Santos, M. Lewenstein, and T. Pfau. The physics of dipolar bosonic quantum gases. *Rep. Prog. Phys.*, 72:126401, 2009.
- [30] L. D. Carr, D. DeMille, R. V. Krems, and J. Ye. Cold and ultracold molecules: science, technology, and applications. *New J. Phys.*, 11:055049, 2009.
- [31] M. A. Baranov, M. Dalmonte, G. Pupillo, and P. Zoller. Condensed Matter Theory of Dipolar Quantum Gases. *Chem. Rev.*, 112:5012, 2012.
- [32] K. Góral, L. Santos, and M. Lewenstein. Quantum phases of dipolar bosons in optical lattices. *Phys. Rev. Lett.*, 88:170406, 2002.
- [33] L. Santos, G. V. Shlyapnikov, and M. Lewenstein. Roton-maxon spectrum and stability of trapped dipolar Bose-Einstein condensates. *Phys. Rev. Lett.*, 90:250403, 2003.
- [34] M. A. Baranov, M. S. Mar'enko, Val. S. Rychkov, and G. V. Shlyapnikov. Superfluid pairing in a polarized dipolar Fermi gas. *Phys. Rev. A*, 66:013606, 2002.
- [35] D.-W. Wang, M. D. Lukin, and E. Demler. Quantum fluids of self-assembled chains of polar molecules. *Phys. Rev. Lett.*, 97:180413, 2006.
- [36] A. Pikovski, M. Klawunn, G. V. Shlyapnikov, and L. Santos. Interlayer superfluidity in bilayer systems of fermionic polar molecules. *Phys. Rev. Lett.*, 105:215302, 2010.
- [37] A. Pikovski, M. Klawunn, A. Recati, and L. Santos. Nonlocal state swapping of polar molecules in bilayers. *Phys. Rev. A*, 84:061605, 2011.
- [38] B. Capogrosso-Sansone, C. Trefzger, M. Lewenstein, P. Zoller, and G. Pupillo. Quantum phases of cold polar molecules in 2D optical lattices. *Phys. Rev. Lett.*, 104:125301, 2010.
- [39] L. Pollet, J. D. Picon, H. P. Büchler, and M. Troyer. Supersolid phase with cold polar molecules on a triangular lattice. *Phys. Rev. Lett.*, 104:125302, 2010.
- [40] L. He and W. Hofstetter. Supersolid phase of cold fermionic polar molecules in two-dimensional optical lattices. *Phys. Rev. A*, 83:053629, 2011.
- [41] R. Barnett, D. Petrov, M. Lukin, and E. Demler. Quantum magnetism with multi-component dipolar molecules in an optical lattice. *Phys. Rev. Lett.*, 96:190401, 2006.
- [42] A. V. Gorshkov, S. R. Manmana, G. Chen, J. Ye, E. Demler, M. D. Lukin, and A. M. Rey. Tunable superfluidity and quantum magnetism with ultracold polar molecules. *Phys. Rev. Lett.*, 107:115301, 2011.
- [43] S. V. Syzranov, M. L. Wall, V. Gurarie, and A. M. Rey. Spin-orbital dynamics in a system of polar molecules. *Nat. Commun.*, 5:5391, 2014.

- [44] S. R. Manmana, E. M. Stoudenmire, K. R. A. Hazzard, A. M. Rey, and A. V. Gorshkov. Topological phases in ultracold polar-molecule quantum magnets. *Phys. Rev. B*, 87:081106, 2013.
- [45] M. Heyl, A. Polkovnikov, and S. Kehrein. Dynamical quantum phase transitions in the transverse-field Ising model. *Phys. Rev. Lett.*, 110:135704, 2013.
- [46] P. Hauke and L. Tagliacozzo. Spread of correlations in long-range interacting quantum systems. *Phys. Rev. Lett.*, 111:207202, 2013.
- [47] D. J. Thouless. The flow of a dense superfluid. *Ann. Phys.*, 52:403, 1969.
- [48] A. F. Andreev and I. M. Lifshitz. Quantum theory of defects in crystals. *Sov. Phys. JETP*, 29:1107, 1969.
- [49] A. J. Leggett. Can a solid be superfluid? *Phys. Rev. Lett.*, 25:1543, 1970.
- [50] E. Kim and M. H. W. Chan. Probable observation of a supersolid helium phase. *Nature*, 427:225, 2004.
- [51] S. Balibar. The enigma of supersolidity. *Nature*, 464:176, 2010.
- [52] M. H. W. Chan. Supersolidity. *Science*, 319:1207, 2008.
- [53] D. Y. Kim and M. H. W. Chan. Absence of supersolidity in solid helium in porous vycor glass. *Phys. Rev. Lett.*, 109:155301, 2012.
- [54] J. J. Hudson, B. E. Sauer, M. R. Tarbutt, and E. A. Hinds. Measurement of the electron electric dipole moment using YbF molecules. *Phys. Rev. Lett.*, 89:023003, 2002.
- [55] D. DeMille. Quantum computation with trapped polar molecules. *Phys. Rev. Lett.*, 88:067901, 2002.
- [56] S. E. Maxwell, N. Brahms, R. deCarvalho, D. R. Glenn, J. S. Helton, S. V. Nguyen, D. Patterson, J. Petricka, D. DeMille, and J. M. Doyle. High-flux beam source for cold, slow atoms or molecules. *Phys. Rev. Lett.*, 95:173201, 2005.
- [57] N. R. Hutzler, H.-I. Lu, and J. M. Doyle. The Buffer Gas Beam: An Intense, Cold, and Slow Source for Atoms and Molecules. *Chem. Rev.*, 112:4803, 2012.
- [58] H. L. Bethlem, G. Berden, F. M. H. Crompvoets, R. T. Jongma, A. J. A. van Roij, and G. Meijer. Electrostatic trapping of ammonia molecules. *Nature*, 406:491, 2000.
- [59] S. Chervenkov, X. Wu, J. Bayerl, A. Rohlfes, T. Gantner, M. Zeppenfeld, and G. Rempe. Continuous centrifuge decelerator for polar molecules. *Phys. Rev. Lett.*, 112:013001, 2014.
- [60] M. Zeppenfeld, B. G. U. Englert, R. Glöckner, A. Prehn, M. Mielenz, C. Sommer, L. D. van Buuren, M. Motsch, and G. Rempe. Sisyphus cooling of electrically trapped polyatomic molecules. *Nature*, 491:570, 2012.

- [61] E. S. Shuman, J. F. Barry, and D. DeMille. Laser cooling of a diatomic molecule. *Nature*, 467:820, 2010.
- [62] B. K. Stuhl, M. T. Hummon, M. Yeo, G. Quéméner, and J. Ye. Evaporative cooling of the dipolar hydroxyl radical. *Nature*, 492:396, 2012.
- [63] U. Schlöder, C. Silber, and C. Zimmermann. Photoassociation of heteronuclear lithium. *Appl. Phys. B*, 73:801, 2001.
- [64] J. M. Sage, S. Sainis, T. Bergeman, and D. DeMille. Optical production of ultracold polar molecules. *Phys. Rev. Lett.*, 94:203001, 2005.
- [65] J. Ulmanis, J. Deiglmayr, M. Repp, R. Wester, and M. Weidemüller. Ultracold molecules formed by photoassociation: heteronuclear dimers, inelastic collisions, and interactions with ultrashort laser pulses. *Chem. Rev.*, 112:4890, 2012.
- [66] P. S. Żuchowski and J. M. Hutson. Reactions of ultracold alkali-metal dimers. *Phys. Rev. A*, 81:060703, 2010.
- [67] A. Chotia, B. Neyenhuis, S. A. Moses, B. Yan, J. P. Covey, M. Foss-Feig, A. M. Rey, D. S. Jin, and J. Ye. Long-lived dipolar molecules and Feshbach molecules in a 3D optical lattice. *Phys. Rev. Lett.*, 108:080405, 2012.
- [68] W. L. Meerts and A. Dymanus. Electric dipole moments of OH and OD by molecular beam electric resonance. *Chem. Phys. Lett.*, 23:45, 1973.
- [69] B. K. Stuhl, M. Yeo, B. C. Sawyer, M. T. Hummon, and J. Ye. Microwave state transfer and adiabatic dynamics of magnetically trapped polar molecules. *Phys. Rev. A*, 85:033427, 2012.
- [70] B. Sawyer. *Cold polar molecules for novel collision experiments at low energies*. PhD thesis, University of Colorado, Department of Physics, 2010.
- [71] K. M. R. van der Stam, E. D. van Ooijen, R. Meppelink, J. M. Vogels, and P. van der Straten. Large atom number Bose-Einstein condensate of sodium. *Rev. Sci. Instrum.*, 78:013102, 2007.
- [72] M.-S. Heo, J.-Y. Choi, and Y.-I. Shin. Fast production of large ^{23}Na Bose-Einstein condensates in an optically plugged magnetic quadrupole trap. *Phys. Rev. A*, 83:013622, 2011.
- [73] J. Söding, D. Guéry-Odelin, P. Desbiolles, G. Ferrari, and J. Dalibard. Giant Spin Relaxation of an Ultracold Cesium Gas. *Phys. Rev. Lett.*, 80:1869, 1998.
- [74] T. Weber, J. Herbig, M. Mark, H.-C. Nägerl, and R. Grimm. Bose-Einstein Condensation of Cesium. *Science*, 299(5604):232, 2003.
- [75] W. D. Phillips and H. Metcalf. Laser deceleration of an atomic beam. *Phys. Rev. Lett.*, 48:596, 1982.

- [76] E. Riis, D. S. Weiss, K. A. Moler, and S. Chu. Atom funnel for the production of a slow, high-density atomic beam. *Phys. Rev. Lett.*, 64:1658, 1990.
- [77] E. L. Raab, M. Prentiss, A. Cable, S. Chu, and D. E. Pritchard. Trapping of neutral sodium atoms with radiation pressure. *Phys. Rev. Lett.*, 59:2631, 1987.
- [78] H. J. Metcalf and P. van der Straten. *Laser Cooling and Trapping*. Springer, 1999.
- [79] T. G. Tiecke. Properties of Potassium. available online at: www.tobiastiecke.nl/archive/PotassiumProperties.pdf (revision v1.02, May, 2011), 2011.
- [80] W. Ketterle, K. B. Davis, M. A. Joffe, A. Martin, and D. E. Pritchard. High densities of cold atoms in a *dark* spontaneous-force optical trap. *Phys. Rev. Lett.*, 70:2253, 1993.
- [81] A. L. Migdall, J. V. Prodan, W. D. Phillips, T. H. Bergeman, and H. J. Metcalf. First observation of magnetically trapped neutral atoms. *Phys. Rev. Lett.*, 54:2596, 1985.
- [82] H. F. Hess. Evaporative cooling of magnetically trapped and compressed spin-polarized hydrogen. *Phys. Rev. B*, 34:3476, 1986.
- [83] N. Masuhara, J. M. Doyle, J. C. Sandberg, D. Kleppner, T. J. Greytak, H. F. Hess, and G. P. Kochanski. Evaporative cooling of spin-polarized atomic hydrogen. *Phys. Rev. Lett.*, 61:935, 1988.
- [84] K. B. Davis, M.-O. Mewes, M. A. Joffe, M. R. Andrews, and W. Ketterle. Evaporative cooling of sodium atoms. *Phys. Rev. Lett.*, 74:5202, 1995.
- [85] J. W. Park, C.-H. Wu, I. Santiago, T. G. Tiecke, S. Will, P. Ahmadi, and M. W. Zwierlein. Quantum degenerate Bose-Fermi mixture of chemically different atomic species with widely tunable interactions. *Phys. Rev. A*, 85:051602, 2012.
- [86] U. Fano. Sullo spettro di assorbimento dei gas nobili presso il limite dello spettro d'arco. *Nuovo Cimento*, 12:154, 1935. Translated by G. Pupillo, A. Zannoni, and C. W. Clark: arXiv:cond-mat/0502210v1.
- [87] H. Feshbach. Unified theory of nuclear reactions. *Ann. Phys.*, 5:357, 1958.
- [88] S. Inouye, M. R. Andrews, J. Stenger, H.-J. Miesner, D. M. Stamper-Kurn, and W. Ketterle. Observation of Feshbach resonances in a Bose-Einstein condensate. *Nature*, 392:151, 1998.
- [89] C.-H. Wu, J. W. Park, P. Ahmadi, S. Will, and M. W. Zwierlein. Ultracold fermionic Feshbach molecules of $^{23}\text{Na}^{40}\text{K}$. *Phys. Rev. Lett.*, 109:085301, 2012.
- [90] K. Bergmann, H. Theuer, and B. W. Shore. Coherent population transfer among quantum states of atoms and molecules. *Rev. Mod. Phys.*, 70:1003, 1998.
- [91] J. W. Park, S. A. Will, and M. W. Zwierlein. Two-photon pathway to ultracold ground state molecules of $^{23}\text{Na}^{40}\text{K}$. *New J. Phys.*, 17:075016, 2015.

- [92] B. Damski, L. Santos, E. Tiemann, M. Lewenstein, S. Kotochigova, P. Julienne, and P. Zoller. Creation of a dipolar superfluid in optical lattices. *Phys. Rev. Lett.*, 90:110401, 2003.
- [93] J. K. Freericks, M. M. Maška, A. Hu, T. M. Hanna, C. J. Williams, P. S. Julienne, and R. Lemański. Improving the efficiency of ultracold dipolar molecule formation by first loading onto an optical lattice. *Phys. Rev. A*, 81:011605, 2010. Erratum: *Phys. Rev. A*, 82:039901.
- [94] G. Herzberg. *Molecular spectra and molecular structure*. Van Nostrand Reinhold Company, 1950.
- [95] T. A. Schulze, I. I. Temelkov, M. W. Gempel, T. Hartmann, H. Knöckel, S. Ospelkaus, and E. Tiemann. Multichannel modeling and two-photon coherent transfer paths in NaK. *Phys. Rev. A*, 88:023401, 2013.
- [96] W. Müller and W. Meyer. Ground-state properties of alkali dimers and their cations (including the elements Li, Na, and K) from abinitio calculations with effective core polarization potentials. *J. Chem. Phys.*, 80:3311, 1984.
- [97] M. W. Gempel. A Laser system for Cooling and Trapping of ^{40}K . Master's thesis, Physik Department TUM, Max Planck Institut für Quantenoptik, 2010.
- [98] G. C. Bjorklund. Frequency-modulation spectroscopy a new method for measuring weak absorptions and dispersions. *Opt. Lett.*, 5:15, 1980.
- [99] D. A. Steck. Sodium D Line Data. available online at: <http://steck.us/alkalidata> (revision 2.1.4, 23. December 2010), 2010.
- [100] T. A. Schulze. Leibniz Universität Hannover, Fakultät für Mathematik und Physik, Institut für Quantenoptik, 2016. Unpublished doctoral dissertation.
- [101] T. Bergeman, G. Erez, and H. J. Metcalf. Magnetostatic trapping fields for neutral atoms. *Phys. Rev. A*, 35:1535, 1987.
- [102] T. Hartmann. Leibniz Universität Hannover, Fakultät für Mathematik und Physik, Institut für Quantenoptik, 2016. Unpublished doctoral dissertation.
- [103] T. W. Hänsch and A. L. Schawlow. Cooling of gases by laser radiation. *Opt. Commun.*, 13:68, 1975.
- [104] D. J. Wineland and H. Dehmelt. Proposed $10^{-14}Dv < v$ laser fluorescence spectroscopy on Tl⁺ mono-ion oscillator III (side band cooling). *Bull. Am. Phys. Soc.*, 20:637, 1975.
- [105] A. Aspect, E. Arimondo, R. Kaiser, N. Vansteenkiste, and C. Cohen-Tannoudji. Laser cooling below the one-photon recoil energy by velocity-selective coherent population trapping. *Phys. Rev. Lett.*, 61:826, 1988.
- [106] M. Kasevich and S. Chu. Laser cooling below a photon recoil with three-level atoms. *Phys. Rev. Lett.*, 69:1741, 1992.

- [107] U. Volz, M. Majerus, H. Liebel, A. Schmitt, and H. Schmoranzer. Precision lifetime measurements on NaI $3p^2P_{1/2}$ and $3p^2P_{3/2}$ by beam-gas-laser spectroscopy. *Phys. Rev. Lett.*, 76:2862, 1996.
- [108] S. Y. T. van de Meerakker, H. L. Bethlem, N. Vanhaecke, and G. Meijer. Manipulation and control of molecular beams. *Chem. Rev.*, 112:4828, 2012.
- [109] R. E. Honig. <http://www.targisol.csic.es/elements/vaporpressure1.html>.
- [110] M. Petzold. Zeeman Slower und magnetischer Transport zur Präparation einer quantenentarteten Mischung aus ^{23}Na und ^{40}K . Master's thesis, Leibniz Universität Hannover Fakultät für Mathematik und Physik Institut für Quantenoptik, 2012.
- [111] R. S. Williamson III. *Magneto-optical trapping of potassium isotopes*. PhD thesis, University of Wisconsin Madison, Physics, 1997. available online at: www-atoms.physics.wisc.edu/People/RobsThesis.pdf.
- [112] S. Earnshaw. On the nature of the molecular forces which regulate the constitution of the luminiferous ether. *Trans. Camb. Phil. Soc.*, 7:97, 1842.
- [113] C. J. Pethick and H. Smith. *Bose-Einstein Condensation in Dilute Gases*. Cambridge, 2008.
- [114] W. Ketterle and N.J. van Druten. Evaporative cooling of atoms. *Adv. At. Mol. Opt. Phy.*, 37:181, 1996.
- [115] W. Petrich, M. H. Anderson, J. R. Ensher, and E. A. Cornell. Stable, tightly confining magnetic trap for evaporative cooling of neutral atoms. *Phys. Rev. Lett.*, 74:3352, 1995.
- [116] D. E. Pritchard. Cooling neutral atoms in a magnetic trap for precision spectroscopy. *Phys. Rev. Lett.*, 51:1336, 1983.
- [117] Y. V. Gott, M. S. Ioffe, and V. G. Tel'kowskii. *Nucl. Fusion Suppl.*, 3:1045, 1962.
- [118] M.-O. Mewes, M. R. Andrews, N. J. van Druten, D. M. Kurn, D. S. Durfee, and W. Ketterle. Bose-Einstein condensation in a tightly confining dc magnetic trap. *Phys. Rev. Lett.*, 77:416, 1996.
- [119] K. B. Davis, M.-O. Mewes, and W. Ketterle. An analytical model for evaporative cooling of atoms. *Appl. Phys. B*, 60:155, 1995.
- [120] E. Schwanke. Hyperfeinstruktur des NaK-Grundzustandes und Intensitätsstabilisierung einer Dipolfalle. Master's thesis, Leibniz Universität Hannover Fakultät für Mathematik und Physik Institut für Quantenoptik, 2014.
- [121] C.-H. Hong, J.-H. Shin, N.-M. Park, K.-H. Kim, B.-S. Kim, J.-S. Kwak, B.-K. Ju, and W.-S. Cheong. Effects of Nb_2O_5 and SiO_2 buffer layers on the suppression of potassium out-diffusion into indium tin oxide electrode formed on chemically strengthened glass. *Jpn. J. Appl. Phys.*, 53:08NG01, 2014.

- [122] E. Tiesinga, C. J. Williams, P. S. Julienne, K. M. Jones, P. D. Lett, and W. D. Phillips. A spectroscopic determination of scattering lengths for sodium atom collisions. *Chem. Rev.*, 101:505, 1996.
- [123] C. R. Monroe, E. A. Cornell, C. A. Sackett, C. J. Myatt, and C. E. Wieman. Measurement of Cs-Cs elastic scattering at $T = 30 \mu\text{K}$. *Phys. Rev. Lett.*, 70:414, 1993.
- [124] C. Ospelkaus. *Fermi-Bose mixtures – From mean-field interactions to ultracold chemistry*. PhD thesis, Department Physik, Universität Hamburg, 2006.
- [125] T. P. Crowley, E. A. Donley, and T. P. Heavner. Quantum-based microwave power measurements: Proof-of-concept experiment. *Rev. Sci. Instrum.*, 75:2575, 2004.
- [126] W. Ketterle and M. W. Zwierlein. Making, probing and understanding ultracold Fermi gases. In *Proc. Internat. School Phys. Enrico Fermi, Course CLXIV*, page 95. IOS Press, Amsterdam, 2008.
- [127] S. Chu, J. E. Bjorkholm, A. Ashkin, and A. Cable. Experimental observation of optically trapped atoms. *Phys. Rev. Lett.*, 57:314, 1986.
- [128] R. Grimm, M. Weidemüller, and Y. B. Ovchinnikov. Optical dipole traps for neutral atoms. *Adv. At. Mol. Opt. Phys.*, 42:95, 2000.
- [129] J. G. Danzl, M. J. Mark, E. Haller, M. Gustavsson, R. Hart, J. Aldegunde, J. M. Hutson, and H.-C. Nägerl. An ultracold high-density sample of rovibronic ground-state molecules in an optical lattice. *Nat. Phys.*, 6:265, 2010.
- [130] W. Ketterle, D. S. Durfee, and D. M. Stamper-Kurn. Making, probing and understanding Bose-Einstein condensates. In *Proc. Internat. School Phys. Enrico Fermi, Course CXL*, page 67. IOS Press, Amsterdam, 1999.
- [131] M. R. Andrews, M.-O. Mewes, N. J. van Druten, D. S. Durfee, D. M. Kurn, and W. Ketterle. Direct, nondestructive observation of a Bose condensate. *Science*, 273:84, 1996.
- [132] M. R. Andrews, D. M. Kurn, H.-J. Miesner, D. S. Durfee, C. G. Townsend, S. Inouye, and W. Ketterle. Propagation of sound in a Bose-Einstein condensate. *Phys. Rev. Lett.*, 79:553, 1997.
- [133] C. C. Bradley, C. A. Sackett, and R. G. Hulet. Bose-Einstein condensation of lithium: observation of limited condensate number. *Phys. Rev. Lett.*, 78:985, 1997.
- [134] L. D. Turner, K. F. E. M. Domen, and R. E. Scholten. Diffraction-contrast imaging of cold atoms. *Phys. Rev. A*, 72:031403, 2005.
- [135] Y. Miroshnychenko, D. Schrader, S. Kuhr, W. Alt, I Dotsenko, M. Khudaverdyan, A. Rauschenbeutel, and D. Meschede. Continued imaging of the transport of a single neutral atom. *Opt. Express*, 11:3498, 2003.
- [136] K. D. Nelson, X. Li, and D. S. Weiss. Imaging single atoms in a three-dimensional array. *Nat. Phys.*, 3:556, 2007.

- [137] W. S. Bakr, J. I. Gillen, A. Peng, S. Fölling, and M. Greiner. A quantum gas microscope for detecting single atoms in a Hubbard-regime optical lattice. *Nature*, 462:74, 2009.
- [138] J. F. Sherson, C. Weitenberg, M. Endres, M. Cheneau, I. Bloch, and S. Kuhr. Single-atom-resolved fluorescence imaging of an atomic Mott insulator. *Nature*, 467:68, 2010.
- [139] Z. Hu and H. J. Kimble. Observation of a single atom in a magneto-optical trap. *Opt. Lett.*, 19:1888, 1994.
- [140] E. W. Streed, A. Jechow, B. G. Norton, and D. Kielpinski. Absorption imaging of a single atom. *Nat. Commun.*, 3:933, 2012.
- [141] E. Haller, J. Hudson, A. Kelly, D. A. Cotta, B. Peaudecerf, G. D. Bruce, and S. Kuhr. Single-atom imaging of fermions in a quantum-gas microscope. *Nature Physics*, 11:738, 2015.
- [142] D. Wang, B. Neyenhuis, M. H. G. de Miranda, K.-K. Ni, S. Ospelkaus, D. S. Jin, and J. Ye. Direct absorption imaging of ultracold polar molecules. *Phys. Rev. A*, 81:061404, 2010.
- [143] C. Ospelkaus, S. Ospelkaus, L. Humbert, P. Ernst, K. Sengstock, and K. Bongs. Ultracold heteronuclear molecules in a 3D optical lattice. *Phys. Rev. Lett.*, 97:120402, 2006.
- [144] T. Köhler, K. Góral, and P. S. Julienne. Production of cold molecules via magnetically tunable Feshbach resonances. *Rev. Mod. Phys.*, 78:1311, 2006.
- [145] J. W. Park, S. A. Will, and M. W. Zwierlein. Ultracold dipolar gas of fermionic $^{23}\text{Na}^{40}\text{K}$ molecules in their absolute ground state. *Phys. Rev. Lett.*, 114:205302, 2015.
- [146] T. Takekoshi, L. Reichsöllner, A. Schindewolf, J. M. Hutson, C. R. Le Sueur, O. Dulieu, F. Ferlaino, R. Grimm, and H.-C. Nägerl. Ultracold dense samples of dipolar RbCs molecules in the rovibrational and hyperfine ground state. *Phys. Rev. Lett.*, 113:205301, 2014.
- [147] J. J. Zirbel, K.-K. Ni, S. Ospelkaus, T. L. Nicholson, M. L. Olsen, P. S. Julienne, C. E. Wieman, J. Ye, and D. S. Jin. Heteronuclear molecules in an optical dipole trap. *Phys. Rev. A*, 78:013416, 2008.
- [148] G. Thalhammer, K. Winkler, F. Lang, S. Schmid, R. Grimm, and J. Hecker Denschlag. Long-lived Feshbach molecules in a three-dimensional optical lattice. *Phys. Rev. Lett.*, 96:050402, 2006.
- [149] S. A. Moses, J. P. Covey, M. T. Miecnikowski, B. Yan, B. Gadway, J. Ye, and D. S. Jin. Creation of a low-entropy quantum gas of polar molecules in an optical lattice. *Science*, 350:659, 2015.

- [150] C. Chin, R. Grimm, P. Julienne, and E. Tiesinga. Feshbach resonances in ultracold gases. *Rev. Mod. Phys.*, 82:1225, 2010.
- [151] H. Friedrich. *Theoretical Atomic Physics*. Springer, 2006.
- [152] A. J. Moerdijk, B. J. Verhaar, and A. Axelsson. Resonances in ultracold collisions of ${}^6\text{Li}$, ${}^7\text{Li}$, and ${}^{23}\text{Na}$. *Phys. Rev. A*, 51:4852, 1995.
- [153] F. Schwarz, T.-O. Müller, and H. Friedrich. Near-threshold Feshbach resonances in interatomic collisions and spectra. *Phys. Rev. A*, 85:052703, 2012.
- [154] E. Timmermans, P. Tommasini, M. Hussein, and A. Kerman. Feshbach resonances in atomic Bose–Einstein condensates. *Phys. Rep.*, 315:199, 1999.
- [155] F. A. van Abeelen and B. J. Verhaar. Time-dependent Feshbach resonance scattering and anomalous decay of a Na Bose-Einstein condensate. *Phys. Rev. Lett.*, 83:1550, 1999.
- [156] F. H. Mies, E. Tiesinga, and P. S. Julienne. Manipulation of Feshbach resonances in ultracold atomic collisions using time-dependent magnetic fields. *Phys. Rev. A*, 61:022721, 2000.
- [157] J. Herbig, T. Kraemer, M. Mark, T. Weber, C. Chin, H.-C. Nägerl, and R. Grimm. Preparation of a pure molecular quantum gas. *Science*, 301:1510, 2003.
- [158] A. Simoni, F. Ferlaino, G. Roati, G. Modugno, and M. Inguscio. Magnetic control of the interaction in ultracold K-Rb mixtures. *Phys. Rev. Lett.*, 90:163202, 2003.
- [159] S. Inouye, J. Goldwin, M. L. Olsen, C. Ticknor, J. L. Bohn, and D. S. Jin. Observation of heteronuclear Feshbach resonances in a mixture of bosons and fermions. *Phys. Rev. Lett.*, 93:183201, 2004.
- [160] J. K. Kuklinski, U. Gaubatz, F. T. Hioe, and K. Bergmann. Adiabatic population transfer in a three level system driven by delayed laser pulses. *Phys. Rev. A*, 40:6741, 1989.
- [161] L. P. Yatsenko, V. I. Romanenko, B. W. Shore, and K. Bergmann. Stimulated Raman adiabatic passage with partially coherent laser fields. *Phys. Rev. A*, 65:043409, 2002.
- [162] M. Mackie, R. Kowalski, and J. Javanainen. Bose-stimulated Raman adiabatic passage in photoassociation. *Phys. Rev. Lett.*, 84:3803, 2000.
- [163] S. Stellmer, B. Pasquiou, R. Grimm, and F. Schreck. Creation of ultracold Sr_2 molecules in the electronic ground state. *Phys. Rev. Lett.*, 109:115302, 2012.
- [164] I. Temelkov, H. Knöckel, A. Pashov, and E. Tiemann. Molecular beam study of the $a^3\Sigma^+$ state of NaK up to the dissociation limit. *Phys. Rev. A*, 91:032512, 2015.
- [165] K. K. Voges. Leibniz Universität Hannover, Fakultät für Mathematik und Physik, Institut für Quantenoptik, 2016. Unpublished doctoral dissertation.

- [166] J. Wöhler. Ein Ramanlasersystem zur Erzeugung ultrakalter Moleküle. Master's thesis, Leibniz Universität Hannover Fakultät für Mathematik und Physik Institut für Quantenoptik, 2014.
- [167] L. Pauling. The nature of the chemical bond. IV. The energy of single bonds and the relative electronegativity of atoms. *J. Am. Chem. Soc.*, 54:3570, 1932.
- [168] J. Deiglmayr, M. Aymar, R. Wester, M. Weidemüller, and O. Dulieu. Calculations of static dipole polarizabilities of alkali dimers: Prospects for alignment of ultracold molecules. *J. Chem. Phys.*, 129:064309, 2008.
- [169] A. Gerdes, O. Dulieu, H. Knöckel, and E. Tiemann. Stark effect measurements on the NaK molecule. *EPJ D*, 65:105, 2011.
- [170] M. L. Wall, E. Bekaroglu, and L. D. Carr. Molecular Hubbard Hamiltonian: Field regimes and molecular species. *Phys. Rev. A*, 88:023605, 2013.
- [171] J. L. Bohn. Electric dipoles at ultralow temperatures. *arXiv*, 0901:0276v1, 2009.
- [172] M. W. Gempel, T. Hartmann, T. A. Schulze, K. K. Voges, A. Zenesini, and S. Ospelkaus. Versatile electric fields for the manipulation of ultracold NaK molecules. Submitted to *New J. Phys.*, 2016.
- [173] J. von Neumann and E. P. Wigner. Über das Verhalten von Eigenwerten bei adiabatischen Prozessen. *Phys. Z.*, 30:467, 1929.
- [174] C. Zener. Non-adiabatic crossing of energy levels. *Proc. Roy. Soc. A*, 137:696, 1932.
- [175] C. Sias, A. Zenesini, H. Lignier, S. Wimberger, D. Ciampini, O. Morsch, and E. Arimondo. Resonantly enhanced tunneling of Bose-Einstein condensates in periodic potentials. *Phys. Rev. Lett.*, 98:120403, 2007.
- [176] J. L. Horn, D. M. Homan, C. S. Hwang, W. L. Fuqua III, and K. B. MacAdam. Electrostatic cage "Stark barrel" for rapidly switching a uniform electric field through arbitrary angles. *Rev. Sci. Instrum.*, 69:4086, 1998.
- [177] T. Neubert. *Entwicklung und Charakterisierung von lasertransformierbaren Schichten auf Basis von Indiumzinnoxid*. PhD thesis, Fakultät für Elektrotechnik, Informationstechnik, Physik der Technischen Universität Carolo-Wilhelmina, Braunschweig, 2007.
- [178] W. S. Bakr, A. Peng, M. E. Tai, R. Ma, J. Simon, J. I. Gillen, S. Fölling, L. Pollet, and M. Greiner. Probing the superfluid-to-Mott insulator transition at the single-atom level. *Science*, 329:547, 2010.
- [179] M. Cheneau, P. Barmettler, D. Poletti, M. Endres, P. Schauß, T. Fukuhara, C. Gross, I. Bloch, C. Kollath, and S. Kuhr. Light-cone-like spreading of correlations in a quantum many-body system. *Nature*, 481:484, 2012.

- [180] P. M. Preiss, R. Ma, M. E. Tai, A. Lukin, M. Rispoli, P. Zupancic, Y. Lahini, R. Islam, and M. Greiner. Strongly correlated quantum walks in optical lattices. *Science*, 347:1229, 2015.
- [181] M. Endres, M. Cheneau, T. Fukuhara, C. Weitenberg, P. Schauß, C. Gross, L. Mazza, M. C. Ba nuls, L. Pollet, I. Bloch, and S. Kuhr. Observation of correlated particle-hole pairs and string order in low-dimensional Mott insulators. *Science*, 334:200, 2011.
- [182] P. M. Preiss, R. Ma, M. E. Tai, J. Simon, and M. Greiner. Quantum gas microscopy with spin, atom-number, and multilayer readout. *Phys. Rev. A*, 91:041602(R), 2015.
- [183] M. Miranda, R. Inoue, Y. Okuyama, A. Nakamoto, and M. Kozuma. Site-resolved imaging of ytterbium atoms in a two-dimensional optical lattice. *Phys. Rev. A*, 91:063414, 2015.
- [184] L. W. Cheuk, M. A. Nichols, M. Okan, T. Gersdorf, V. Ramasesh, W. S. Bakr, T. Lompe, and M. W. Zwierlein. Quantum-gas microscope for fermionic atoms. *Phys. Rev. Lett.*, 114:193001, 2015.
- [185] M. F. Parsons, F. Huber, A. Mazurenko, C. S. Chiu, W. Setiawan, K. Wooley-Brown, S. Blatt, and M. Greiner. Site-resolved imaging of fermionic ${}^6\text{Li}$ in an optical lattice. *Phys. Rev. Lett.*, 114:213002, 2015.
- [186] B. Zimmermann, T. Müller, J. Meineke, T. Esslinger, and H. Moritz. High-resolution imaging of ultracold fermions in microscopically tailored optical potentials. *New J. Phys.*, 13:043007, 2011.
- [187] C. Weitenberg, M. Endres, J. F. Sherson, M. Cheneau, P. Schauß, T. Fukuhara, I. Bloch, and S. Kuhr. Single-spin addressing in an atomic Mott insulator. *Nature*, 471:319, 2011.
- [188] M. W. Gempel, T. A. Schulze, T. Hartmann, K. K. Voges, A. Zenesini, and S. Ospelkaus. An adaptable two-lens high resolution objective for imaging ultracold atoms. In preparation, 2016.
- [189] J. Hecker Denschlag, J. E. Simsarian, H. Häffner, C. McKenzie, A. Browaeys, D. Cho, K. Helmerson, S. L. Rolston, and W. D. Phillips. A Bose-Einstein condensate in an optical lattice. *J. Phys. B*, 35:3095, 2002.
- [190] W. S. Bakr, P. M. Preiss, M. Eric Tai, R. Ma, J. Simon, and M. Greiner. Orbital excitation blockade and algorithmic cooling in quantum gases. *Nature*, 480:500, 2011.
- [191] P. D. Lett, R. N. Watts, C. I. Westbrook, W. D. Phillips, P. L. Gould, and H. J. Metcalf. Observation of atoms laser cooled below the Doppler limit. *Phys. Rev. Lett.*, 61:169, 1988.

- [192] C. Monroe, D. M. Meekhof, B. E. King, S. R. Jefferts, W. M. Itano, D. J. Wineland, and P. Gould. Resolved-sideband Raman cooling of a bound atom to the 3D zero-point energy. *Phys. Rev. Lett.*, 75:4011, 1995.
- [193] G. Morigi, J. Eschner, and C. H. Keitel. Ground state laser cooling using electromagnetically induced transparency. *Phys. Rev. Lett.*, 85:4458, 2000.
- [194] J. W. Coltman. The specification of imaging properties by response to a sine wave input. *J. Opt. Soc. Am.*, 44:468, 1954.
- [195] D. H. Kelly. Spatial frequency, bandwidth, and resolution. *Appl. Opt.*, 4:435, 1965.
- [196] M. Bass, editor. *Handbook of optics II; Transfer functions techniques*. Optical Society of America, 1995. Ch. 32, G. D. Boreman.
- [197] M. Bass, editor. *Handbook of optics*. Optical Society of America, 1995.
- [198] C. E. Shannon. Communication in the presence of noise. *Proceedings of the IEEE*, 86:447, 1998. This paper is reprinted from the *Proc. IRE*, 37:10, 1949.
- [199] M. Bass, editor. *Handbook of optics I; Optical specifications*. Optical Society of America, 1995. Ch. 35, R. R. Shannon.
- [200] P. Gersema. Charakterisierung eines hochauflösenden Detektionssystems für Na Atome. Master's thesis, Leibniz Universität Hannover Fakultät für Mathematik und Physik Institut für Quantenoptik, 2014.
- [201] A. Edelstein, N. Amodaj, K. Hoover, R. Vale, and N. Stuurman. *Computer Control of Microscopes Using μ Manager*, chapter 14.20. John Wiley & Sons, Inc., 2001.
- [202] C. A. Schneider, W. S. Rasband, and K. W. Eliceiri. NIH Image to ImageJ: 25 years of image analysis. *Nat. Methods*, 9:671, 2012.
- [203] J. Schindelin, I. Arganda-Carreras, E. Frise, V. Kaynig, M. Longair, T. Pietzsch, S. Preibisch, C. Rueden, S. Saalfeld, B. Schmid, J.-Y. Tinevez, D. J. White, V. Hartenstein, K. Eliceiri, P. Tomancak, and A. Cardona. Fiji: an open-source platform for biological-image analysis. *Nat. Methods*, 9:676, 2012.
- [204] L. C. Jr. Roberts, M. D. Perrin, F. Marchis, A. Sivaramakrishnan, R. B. Makidon, J. C. Christou, B. A. Macintosh, L. A. Poyneer, M. A. van Dam, and M. Troy. Is that really your Strehl ratio? In *Proc. SPIE 5490, Advancements in Adaptive Optics*, page 504, 2004.
- [205] R. C. Sterling, H. Rattanasonti, S. Weidt, K. Lake, P. Srinivasan, S. C. Webster, M. Kraft, and W. K. Hensinger. Fabrication and operation of a two-dimensional ion-trap lattice on a high-voltage microchip. *Nat. Commun.*, 5:3637, 2014.
- [206] G. Ritt, G. Cennini, C. Geckeler, and M. Weitz. Laser frequency offset locking using a side of filter technique. *Appl. Phys. B*, 79:363, 2004.

List of Figures

| | | |
|------|---------------------------------------------------------------|----|
| 1.1 | Comparison of dipolar interactions | 3 |
| 1.2 | Comparison molecules | 6 |
| 2.1 | Cut of experiment | 10 |
| 2.2 | Molecule ground state | 12 |
| 2.3 | Cut of main chamber | 15 |
| 2.4 | Picture of opened main chamber | 16 |
| 2.5 | Level scheme of ^{39}K and ^{40}K | 18 |
| 2.6 | D2 line laser system for potassium | 19 |
| 2.7 | Level scheme of ^{23}Na | 21 |
| 2.8 | Cut of top coil | 23 |
| 2.9 | Magnetic fields measured | 24 |
| 2.10 | Cut of Zeeman slower | 28 |
| 2.11 | Cut of 2D-MOT | 30 |
| 2.12 | Simultaneous MOT loading | 31 |
| 2.13 | Decay of the lifetime | 34 |
| 2.14 | Removal of atoms by rf ramp | 38 |
| 2.15 | Microwave circuit | 39 |
| 2.16 | PolarCam main GUI | 45 |
| 2.17 | Feshbach resonance | 48 |
| 2.18 | STIRAP lambda scheme | 50 |
| 3.1 | Polarization | 56 |
| 3.2 | Contours of Stark shift due to perturbation | 57 |
| 3.3 | Scheme of polarized molecules | 58 |
| 3.4 | Deformation of trap potential | 59 |
| 3.5 | Gradient for splitting of layers | 62 |
| 3.6 | Cross section of vacuum chamber | 63 |
| 3.7 | Curvature of four infinite rods | 65 |
| 3.8 | Layout of ITO electrodes | 66 |
| 3.9 | Curvature ratio of inner and outer electrodes | 68 |
| 3.10 | Electrodes on windows | 70 |
| 4.1 | Imaging system | 76 |
| 4.2 | Comparison Airy disk and MTF | 78 |
| 4.3 | Illustration of RMS wavefront error | 79 |
| 4.4 | Illustration objective optimization | 81 |
| 4.5 | Optimized objective (reversed) | 82 |
| 4.6 | Lens system | 84 |
| 4.7 | Simulated MTF | 86 |
| 4.8 | Strehl ratio for varying spacings 3-4 and 5-6 | 87 |

| | | |
|------|----------------------------------------------------------------|-----|
| 4.9 | Objective adjustment to other wavelengths | 88 |
| 4.10 | Objective adjustment to vacuum window thickness | 89 |
| 4.11 | Objective adjustment to vacuum window bend | 90 |
| 4.12 | Objective adjustment to vacuum window wedge and tilt | 90 |
| 4.13 | Objective mount | 91 |
| 4.14 | SEM image of pinhole | 93 |
| 4.15 | Gold nanoparticles | 94 |
| 4.16 | Radially averaged images of gold nanoparticles | 96 |
| 4.17 | MTF obtained by FFT | 97 |
| 5.1 | Electric field magnitude of chip configuration | 101 |
| A.1 | Ambient conditions | 105 |
| A.2 | Offset lock: Down conversion circuit | 106 |
| A.3 | Offset lock: Error signal circuit | 107 |
| A.4 | PI coil control | 108 |
| A.5 | Measured transmission of anti-reflection coating | 109 |
| A.6 | Dispersion Data of ITO | 110 |
| A.7 | Simulated transmission AR + 50 nm ITO | 110 |
| A.8 | Simulated transmission AR + 167 nm ITO | 110 |
| A.9 | Non ideal rotational average | 111 |
| A.10 | Non ideal MTF | 111 |
| A.11 | Zemax screen shot | 112 |

List of Tables

| | | |
|-----|----------------------------------------------------------------|-----|
| 2.1 | Parameters of potassium laser system | 20 |
| 2.2 | Parameters of sodium laser system | 21 |
| 2.3 | Trap depths and frequencies of optical dipole trap | 41 |
| 3.1 | Limits on electric field gradient and curvature | 60 |
| 4.1 | Objective design | 83 |
| 4.2 | Manufacturing tolerances of lenses and resulting RMS | 85 |
| 4.3 | Objective adjustment reoptimized | 87 |
| 4.4 | Objective adjustment air versus vacuum | 88 |
| 4.5 | Window thickness experiment versus test setup | 92 |
| 4.6 | CTF 1951 USAF chart resolution test chart | 93 |
| A.1 | Constants | 104 |
| A.2 | ITO coating | 109 |

Acknowledgments

Actually, I do not want to only acknowledge – I want to gratefully thank everybody who is involved in our experiment and anybody who contributes, has contributed, or will contribute to it. I am sure it will reward us by revealing wonderful physics.

I think I do not have to list people. You know that this experiment requires the enormous efforts of many, not only those working on it.

Still, I wanted to thank Silke for the enormous possibilities she is providing me, for being always available, for listening patiently and giving good advice, for believing in us and the experiment, and for being so involved.

At last, a loud shout out goes to my colleagues Torben, Torsten, Alessandro and Kai for: building vacuum, lasers, electronics, measuring, rebuilding vacuum, remeasuring, dealing with time, sending me a link, making me laugh.

Publications

- i *Multichannel modeling and two-photon coherent transfer paths in NaK*
T. A. Schulze, I. I. Temelkov, M. W. Gempel, T. Hartmann, H. Knöckel, S. Ospelkaus, and E. Tiemann
Phys. Rev. A **88**,023401 (2013)
- ii *Versatile electric fields for the manipulation of ultracold NaK molecules*
M. W. Gempel, T. Hartmann, T. A. Schulze, K. K. Voges, A. Zenesini and S. Ospelkaus
New J. Phys. (Submitted)
- iii *An adaptable two-lens high resolution objective for imaging ultracold atoms*
M. W. Gempel, T. A. Schulze, T. Hartmann, K. K. Voges, A. Zenesini and S. Ospelkaus
In preparation

MATTHIAS W. GEMPEL

Hennigesstr 18

30451 Hannover

Born June 08, 1985 Treuchtlingen (Germany)

Research

Jan. 2011 - Feb. 2016**Doctoral Studies**

Institut für Quantenoptik of Leibniz Universität Hannover

PhD student in the group of Prof. Dr. Silke Ospelkaus

- Towards Ultracold Polar NaK Molecules and the Investigation of Dipolar Quantum Gases
- PhD student Research Training Group 1729

University

Oct. 2005 - Sep. 2010**Diplom Physik**

Technische Universität München

Max Planck Institut für Quantenoptik

Diploma in the group of Prof. Dr. Immanuel Bloch

- A Laser system for Cooling and Trapping of ^{40}K

May 2009**Master's of Science in Physics**

University of Illinois at Urbana Champaign

Community service

Jul. 2004 - Mar. 2005

Gemeindeschwesternstation Treuchtlingen

School

Sep. 2001 - May 2004**Abitur**

Werner-von-Siemens-Gymnasium Weißenburg

Sep. 1995 - Jul. 2001

Senefelder-Schule Treuchtlingen

November 30, 2015